The Dissertation Committee for Hao Wu Certifies that this is the approved version of the following dissertation:

Flame Retardant Nylon 6 Nanocomposite Fibers: Processing and Characterization

Committee:

Mourad Krifa, Supervisor

Joseph H. Koo, Co-Supervisor

Wei Li

Christopher J. Ellison

Jonathan Y. Chen

FLAME RETARDANT NYLON 6 NANOCOMPOSITE FIBERS: PROCESSING AND CHARACTERIZATION

by

Hao Wu, B.E.; M.S.T.A.T.

Dissertation

Presented to the Faculty of the Graduate School of

The University of Texas at Austin

in Partial Fulfillment

of the Requirements

for the Degree of

Doctor of Philosophy

The University of Texas at Austin

August 2016

Dedication

To my parents, for their unconditional love and support throughout my life.

Acknowledgements

Over the years of my PhD study in Austin, I have received tremendous support and encouragement from a great number of kindhearted individuals. First and foremost I would like to express my sincere gratitude to my advisers Dr. Mourad Krifa and Dr. Joseph H. Koo. Both of them have always been extremely encouraging and have great patience in helping me progress throughout my research. They have taught me not just how to be a good researcher, but also the wisdom of life. None of these works could have been accomplished without their guidance.

I would like to express my sincere gratitude to my dissertation committee of Dr. Wei Li, Dr. Christopher J. Ellison and Dr. Jonathan Y. Chen. They all have provided generous support and valuable suggestions to my study.

I'm honored to have worked with many outstanding students and scholars. Special thanks to Ha, Joon, and Dr. Paul from Department of Chemical Engineering; Wei from Department of Mechanical Engineering; Siyuan, Dr. Zhang, Dr. Fathe, and Dr. Smyth from School of Pharmacy; Dr. Zhang, Dr. Smith, and Dr. Celio from Texas Materials Institute; Dwight from Institute for Cellular and Molecular Biology; Dr. Tate and his group from Texas State University; Eric from South Dakota School of Mines and Dr. Natali from University of Perugia.

I'm truly thankful to Kurt, Will, Robert, Brian, Rogelio, Bryan, Chunhong, Wei, Tahar, Renan, Dr. Dickson Lao, Dr. Ayou Hao, Dr. Lan Yao, and Dr. Yanmao Dong from Dr. Krifa and Dr. Koo's group. For the many research projects we have worked together, I have received numerous assistances in many ways and will never forget the great memories over the past years.

I would like to thank all my family and friends, for making my life as a graduate student a happy one.

Flame Retardant Nylon 6 Nanocomposite Fibers: Processing and Characterization

Hao Wu, Ph.D.

The University of Texas at Austin, 2016

Supervisor: Mourad Krifa

Co-supervisor: Joseph H. Koo

One type of engineering thermoplastic polymers that has significant commercial application is nylon. However, flammability and melt dripping is a major problem for polymers like nylon 6 because it can cause fire to spread to other flammable objects and escalate the fire in a short amount of time. Although high performance inherently flame-retardant (FR) fibers have been discovered and various durable FR finishes for nylon have been developed, cost-effective flame retardant nylon and nylon blend fabrics remain a challenge. The goal of this research is to develop non-drip inherently FR nylon 6 fibers as a cost-effective alternative for use in high volume FR fabrics.

In this dissertation, a cost effective alternative of producing non-drip inherently flame retardant nylon 6 fibers with balanced performances was developed based on polymer nanocomposite systems incorporating intumescent FR and nanoclay additives. Nanoclay was added to the system to reduce FR particle loading and capitalize on the synergistic effect between nanoclay and intumescent additives. Adequate dispersion of the additives with exfoliation of the nanoclay platelets was observed using TEM and XRD. Injection molding was used as a tool for screening the performance of the nanocomposite formulations in bulk form before the fiber spinning process. Results of injection molded FR PA6 nanocomposites suggest that although a good FR performance could be achieved,

mechanical properties, especially ductility, were significantly compromised. To solve this problem, rubber toughening was achieved using a thermoplastic elastomer with significant success in recovering material ductility without compromising FR performance. Ultra-sonication of the FR additives prior the fiber spinning could effectively reduce the FR particle size distribution. Single fiber tensile tests show that PA6/FR/elastomer/nanoclay formulation is able to improve both the tenacity and elongation at break from the original PA6/FR system. Moreover, flammability tests suggest that the nanocomposite FR fibers have significantly lower heat release properties and are able to retain a fibrous shape after combustion indicating the non-dripping property. Therefore, our experiments have yielded improved non-drip FR properties in PA6 through the infusion of nanoclay and non-halogenated intumescent particles (FR) via co-rotating twin-screw extrusion. One major implication of these results is that with the new non-drip FR nylon 6 fiber, it would be possible to achieve blends with higher nylon content than customary and not compromise the FR performance of the fabric, thus providing a cost effective solution for high-volume applications.

Table of Contents

List of Tables

List of Figures

Chapter 1: Introduction

1.1 BACKGROUND

From apparel to carpets, polymeric fibers are abundant in people's daily life. In 2014 the world production of textile fibers reached 96 million tons, 67.5% of which are manmade fibers [1]. One type of engineering thermoplastic polymers that has significant commercial application are aliphatic or semi-aromatic polyamides (PA) often known as nylon. Dr. Wallace Carothers at DuPont Experimental Station Laboratory invented nylon (nylon 66) in 1935 [2]. Nylon is a generic name for a family of polymers which contain the amide groups (-CONH-) in their polymer backbone. High tensile strength, ductility and ease of production promptly made nylon the first commercial synthetic fiber in history. During World War II, nylon was an essential material for making airborne parachutes as well as tire cords, tents, and ropes for the military. Eighty years later, nylons are still widely used as an important engineering thermoplastic in the fields of textiles, automotive, and electrical industry. In recent years, it has found novel applications, such as fiber reinforced composites and 3D printing.

Depending on the arrangement of the amide linkages of the polymer chain, nylons can be classified into AB types or AABB types. AB types are usually made by polycondensation from cyclic amides or lactams (Equation 1.1). In AABB type nylons, the amide bond alternates between the polymer backbone and are formed by reaction of diamcids and diamines (Equation 1.2) [2, 3].

$$n\ H_2N\text{-}(CH_2)_x\text{-}NH_2 + n\ HOOC\text{-}(CH_2)_{y\text{-}2}\text{-}COOH \leftrightarrow$$
$$H\text{-}[HN\text{-}(CH_2)_x\text{-}NHCO\text{-}(CH_2)_{y\text{-}2}\text{-}CO]_n\text{-}OH + (2n\text{-}1)\ H_2O \quad (1.1)$$

$$n\ H_2N\text{-}(CH_2)_{x\text{-}1}\text{-}COOH \leftrightarrow H\text{-}[HN\text{-}(CH_2)_{x\text{-}1}\text{-}CO]_n\text{+}(n\text{-}1)H_2O \quad (1.2)$$

Discovered by Schlack in 1938, polyamide 6 (PA6) or nylon 6 inherits many outstanding properties of the nylon family including chemical resistance, ease to process, high impact resistance, elasticity and elastic recovery [2]. PA6 is commercially made by hydrolytic ring-opening polymerization of ε–caprolactam (Figure 1.1). Anionic polymerization can also be used to produce PA6 but this process is not commercialized because of its relatively high cost [2]. Similar to other nylons, the hydrogen bonding among polymer chains enhances its mechanical strength. The low cost and good balance between tensile modulus, strength and chemical resistance has led to widespread use of PA6 in applications, such as fibers, films, gears, bearing, and automotive parts.

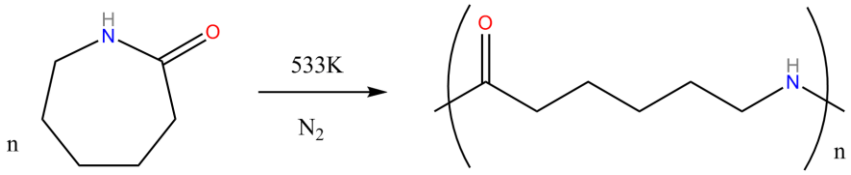

Figure 1.1. Ring opening polymerization of nylon 6.

Like many other polyamides, PA6 is a semi-crystalline polymer consisting of amorphous and crystalline regions. Such combination of crystalline and amorphous structures leads to balanced material properties. The crystalline regions are ordered periodic structures usually formed by folding polymer chains, whereas the amorphous regions consist of random isotropic polymer chains. PA6 has two main stable crystal structures denoted as α and γ crystals (Figure 1.2). To optimize the number of H-bonds, the PA6 polymer chains have to adopt a fully extended, i.e. monoclinic α crystal structure or twisted configuration, i.e. γ form crystal structure. Because of the bond structure, the α form is more thermodynamically stable than the γ form. Figure 1.2 shows polymer chains

of an α crystal that run parallel in opposite directions. With d-spacing of 0.37 nm, α phase crystal has two characteristic X-ray diffraction peaks at 20 and 23.7° indicating (200) and (002)/(202) reflections. To accommodate the formation of H-bonds, γ crystals contain twisted polymer chains with larger bond length pointing in the same direction [4]. The characteristic X-ray peaks for γ phase are 10.7 and 21.4° which are indexed as (020) and (001), respectively. The formation of α form or γ form depends on processing conditions, such as thermal conditions, applied stress, presences of moisture and additives that are present. In general, fast cooling or quenching PA6 from polymer melt results in γ form crystal [2].

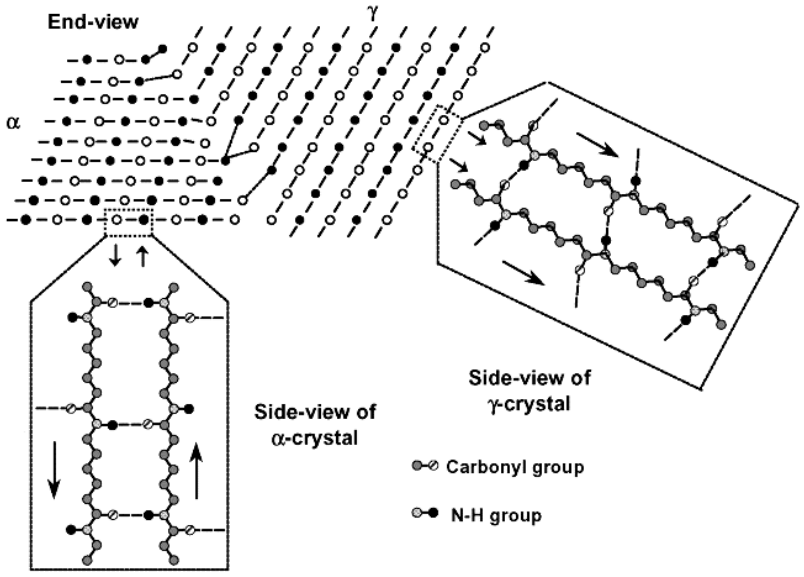

Figure 1.2. Schematic of hydrogen bonding within the α and γ crystalline forms of PA6 as seen from end and side-view of each crystal [4].

In addition to the crystal structures, morphology of the crystalline and amorphous regions can also affect the material properties of nylon. Depending on molecular weight, the arrangement of the crystalline regions and the crystallization conditions, e.g. cooling rate, isothermal crystallization temperature etc. can result in different morphologies. For

example, Figure 1.3 shows a typical spherical semi-crystalline structure called spherulite. When PA6 cools down from its melting temperature and above, the polar amide groups form hydrogen bonds between CO and NH groups. Crystalline regions are formed through folded polymer chains, and these thin crystal lamellas accommodate the maximum number of hydrogen bonds. At the same time, amorphous regions fill up the remaining space. The dimensions of the crystal lamellas and the amorphous regions are usually less than a few tens of nanometers. This self-assembly process of semi-crystalline structure makes themselves a "nanocomposite" which usually involves two components, i.e. nanoparticle and polymer matrix [5]. Such semi-crystalline structure yields good performance balance. The crystalline regions contribute to high yield strength, chemical and abrasion resistance as well as thermal stability whereas the amorphous regions help improve its impact resistance and ductility.

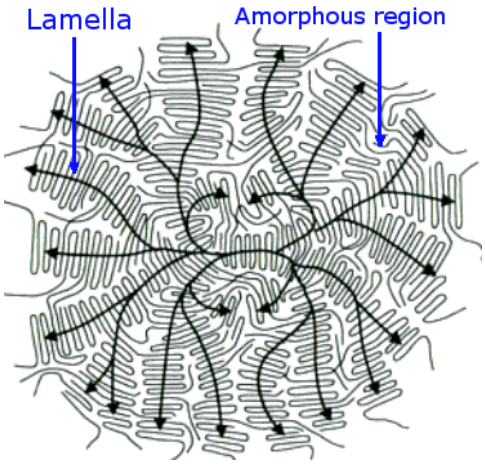

Figure 1.3. Schematic model of a spherulite structure [6].

Unlike many hydrocarbon polymers, PA6 and other polyamides have a certain degree of flame retardancy which can be attributed to the presence of nitrogen in the amide group [7, 8]. The limiting oxygen index (LOI) of PA6 ranges from 21 to 25 compared to

17.4% for polyethylene [2, 7]. The degradation products of PA6 include cyclic monomer carprolactam as well as carbon monoxide, ammonia, nitriles, and hydrocarbons which could impede the combustion by diluting the oxygen environment. However, despite the above, flammability remains a problem for PA6 in a broad range of applications. Indeed, nylon 6 tends to melt and drip when exposed to fire. Melt dripping is a major problem for polymers like nylon 6 because it can cause fire to spread to other flammable objects and escalate the fire in a short amount of time. In the following sections, mechanisms of polymer degradation and combustion will be discussed and different methods to make polymers flame retardant will also be introduced.

1.2 POLYMER DEGRADATION AND COMBUSTION

Because of their organic nature, many polymeric materials, especially thermoplastic polymers, such as polyethylene, polypropylene and polyamide are flammable. Because they may cause dramatic loss of life and property, fire hazards associated with the use of polymeric materials have been a critical issue. According to the National Fire Protection Association (NFPA), the year 2014 saw 1,298,000 fires in the United States causing 3,275 civilian deaths, 15,775 injuries, and 9.8 billion dollars in property damage [9]. Flame retardant fibers in material goods could have prevented many of these accidents.

Due to their high concentrations of carbon and hydrogen, polymers with no flame retardant treatment constitute a significant fuel supply in case of fire. In addition to flame, smoke emission and dripping are major problems for most commodity and engineering thermoplastic polymer fibers.

Typically, burning or flaming combustion of a polymer material starts with the degradation of polymer chains yielding combustible small molecules. Degradation of

polymers in an oxygen environment is a rather complex process which involves thermal oxidative degradation. Several simplified models have been developed considering only the degradation of pure polymer without the influence of oxygen. It is suggested that pure polymers degrade through one or a combination of the following routes: 1. End-chain scission where individual monomers successively cleaved from the chain end; 2. Random-chain scission which happens randomly through the polymer chain; 3. Chain stripping where atoms or functional groups not from the polymer backbone are cleaved off, and 4. Cross-linking where new bonds are created between polymer chains [10].

It is generally accepted that the thermal decomposition of PA6 starts with hemolytic scission of the N-alkyl-amide bond (Figure 1.4).

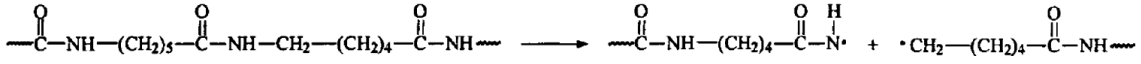

Figure 1.4. Hemolytic scission of the N-alkyl-amide bond [11].

Random scission leads to the formation of volatile products consisting of various low molecular weight polymer chain fragments. Although the predominant volatile pyrolysis products are cyclic monomers ε-caprolactam and butyrolactam [2, 12, 13], the amount and structure are dictated by the heating environment, i.e. temperature and presence of nucleophile such as water [14]. According to Davis et al. [14], without nucleophile the degradation of nylon 6 at temperatures between 200°C to 300°C forms mainly small amounts of ε-caprolactam monomers (Figure 1.5A) through intramolecular and intermolecular cyclization. From 500°C to 800°C, the decomposition of dry nylon 6 yields monomer, cyclic oligomers, polymer chain end groups, as well as other small molecules. In the presence of water as a nucleophile, hydrolysis of the peptide bond occurs below 300°C (Figure 1.5B) [11, 14]. At higher temperatures, conjugated compounds of C=C and

nitrile groups are detected. A detailed review on the thermal degradation mechanisms of PA6 can be found in [11].

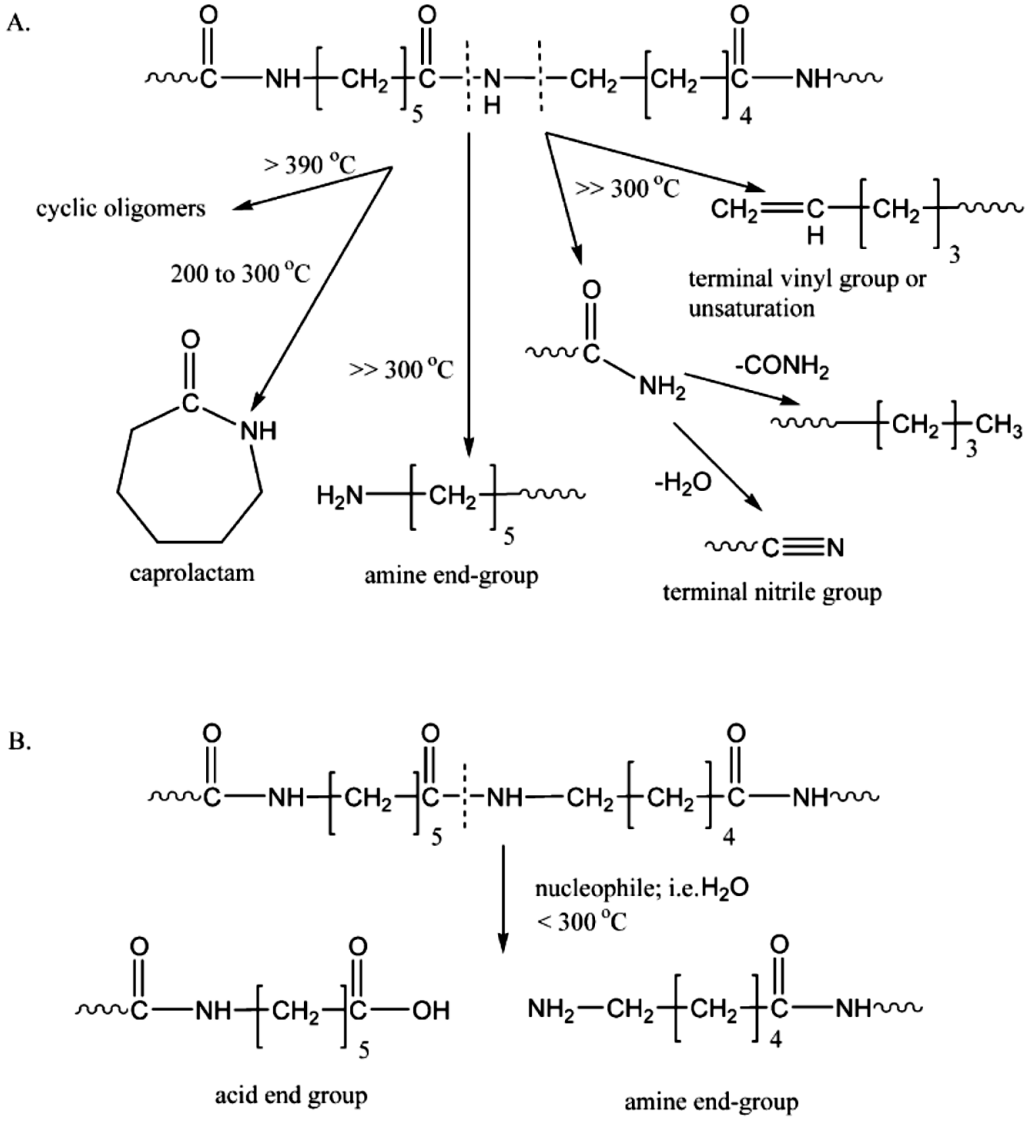

Figure 1.5. Degradation pathways of nylon 6 with (A) and without (B) nucleophile [14].

It is suggested that the thermal stability of nylon can be affected by the synthesis and processing techniques used. At elevated temperatures, the reduction in degree of

polymerization of anionically synthesized PA6 is much faster than that of hydrolytically made PA6 [15].

Polymer degradation provides a fuel source for the combustion which is a gas-phase reaction [16]. Generally, combustibles and combustives are the two components involved in a combustion process. The combustibles act as reducing agents which in this case are the degradation products from polymer chains. The combustive serves as oxidizing agents. The most common combustive is oxygen in air.

During the first stage of combustion, polymer bond scission occurs due to the heat source. Small molecules, such as methane (CH_4) result from the scission and are released into the surrounding air, creating a combustible gaseous mixture. This reaction can be approximated by the Arrhenius equation (Equation 1.3) which will be discussed in more details in Chapter 3. Two different methods of ignition can take place in this premixed flame scenario: as the temperature increases, the premixed fuels ignite when a critical temperature is reached. This phenomenon is called auto-ignition, and the critical temperature is called auto-ignition temperature (AIT). Another ignition circumstance is called piloted ignition, where combustion is initiated with help from a "localized energy source," such as an electric spark or existing flame. The temperature of a piloted ignition can be well below AIT [17].

$$\dot{m}'''_{\mathrm{F,r}} = A\,\mathrm{e}^{-E/(RT)} \tag{1.3}$$

After ignition, and in the absence of an external heat source, a continuous combustion cycle as shown in Figure 1.6 can be established if the amount of heat liberated from the ignition of decomposed products is enough to induce further decomposition from the solid phase.

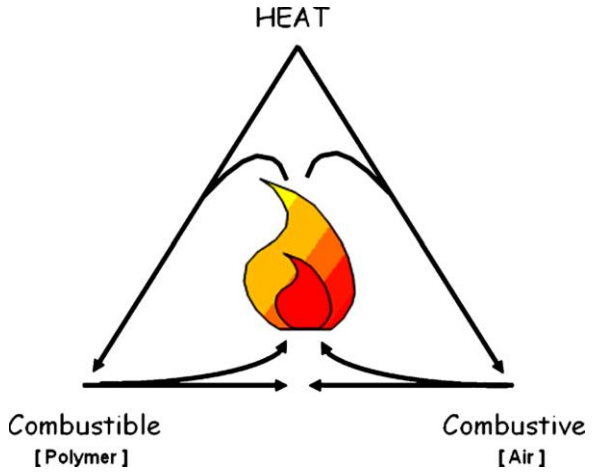

Figure 1.6. The combustion triangle [18].

Developed by Calcraft and Maries [19], Figure 1.7 is an illustration of a detailed gradient structure of materials during combustion. On the burning surface, heat generated by combustion will be conducted into and through the char layer while some energy will be transferred backward through convection of decomposition gases passing through the char layer. Under the char layer is where the polymer decomposition takes place and some relatively high molecular decomposition products will accumulate to form the char. Materials beneath the decomposition zone are unchanged but will also be heated through conduction and thermal energy will be stored in this region. Beneath the unchanged materials, some energy will be released if the room temperature is lower than the lowest material temperature. As the combustion cycle proceeds, what usually happens is that the pyrolysis of the polymer exceeds stoichiometric oxygen in the surrounding air. Therefore, incomplete combustion will result in soot or smoke. At the end of the reaction, either the fuel or oxidizer or both will be used up, the rate of combustion will slow down and will consequently cease according to Arrhenius.

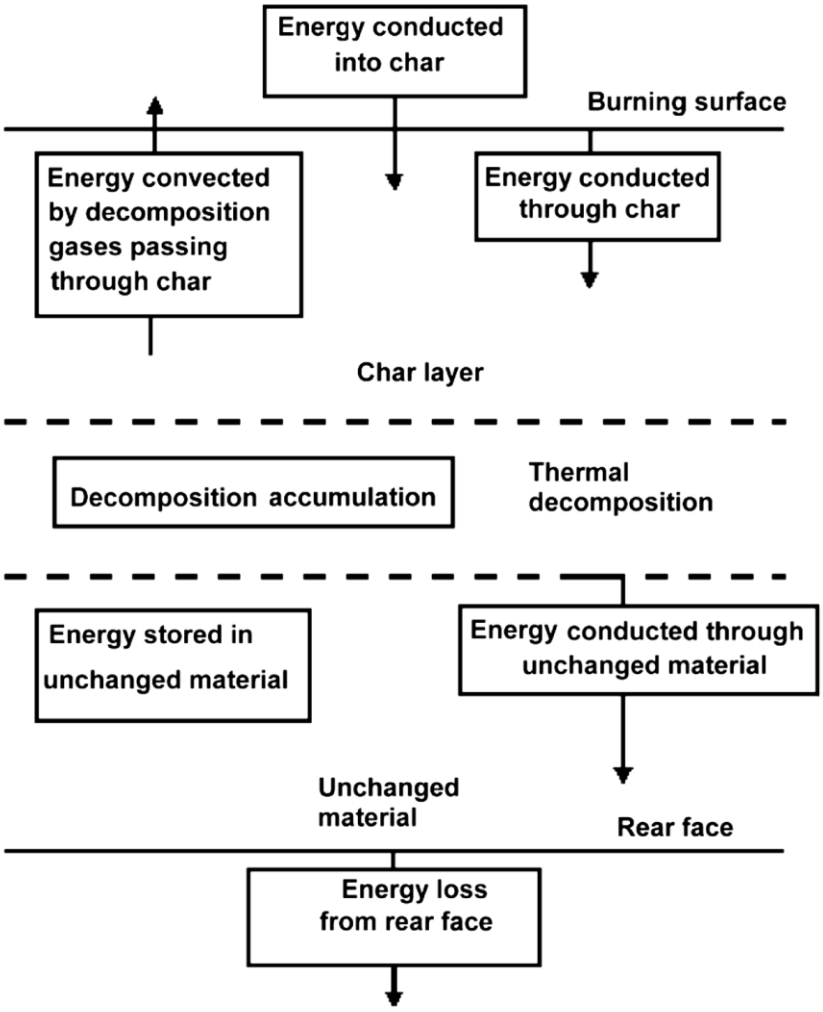

Figure 1.7. Heat transfer during combustion [18].

1.3 FLAMMABILITY CHARACTERIZATION METHODS

A large variety of flammability tests have been developed to characterize materials' ignitability, heat release, flame spread, smoke toxicity, etc. Depending on the scale of the test, flammability tests can be categorized into small, intermediate, and full scale flammability tests [16, 18]. In this section, only four of the most commonly used test methods will be discussed, i.e. cone calorimetry, microscale combustion calorimetry (MCC),

UL-94 and limiting oxygen index (LOI). A more comprehensive review of the flammability tests can be found in [20].

1.3.1 Cone Calorimeter

As one of the most widely used flammability test method, the cone calorimeter was developed by Dr. Vytenis Babrauskas in the early 1980s [16]. The method was later standardized as ASTM E1354 and ISO 5660. The main principle of the test is based on the measurement of oxygen consumption during the combustion process. Figure 1.8 shows the typical set up of a cone calorimeter. A 100×100 mm square sample is fixed on the load cell to monitor the weight loss during test. The cone heater with the shape of a truncated cone is used to radiate heat onto the test specimen at a given heat flux in the range of 10-100 kW/m^2. The pyrolysis products are ignited by an electric spark. All the combustion products are directed through the cone heater and collected by the exhaust hood where gas flow and concentrations of CO, CO_2 and O_2 are measured. Based on the assumption that the amount of heat release for organic materials in general is proportional to the oxygen consumption (E=13.1 kJ/g), heat release rate can then be calculated from the mass flow rate and oxygen concentration. The typical reported values from a cone calorimeter tests include heat release rate (HRR), peak heat release rate (pHRR), total heat release (THR), and time to ignition (TTI) [16, 18].

Although cone calorimetry is one of the most effective tools for flammability test, it requires samples in the 100 gram range, and the results can be affected by factors including ignition source, sample thickness, sample orientation, ventilation, edge conditions [21].

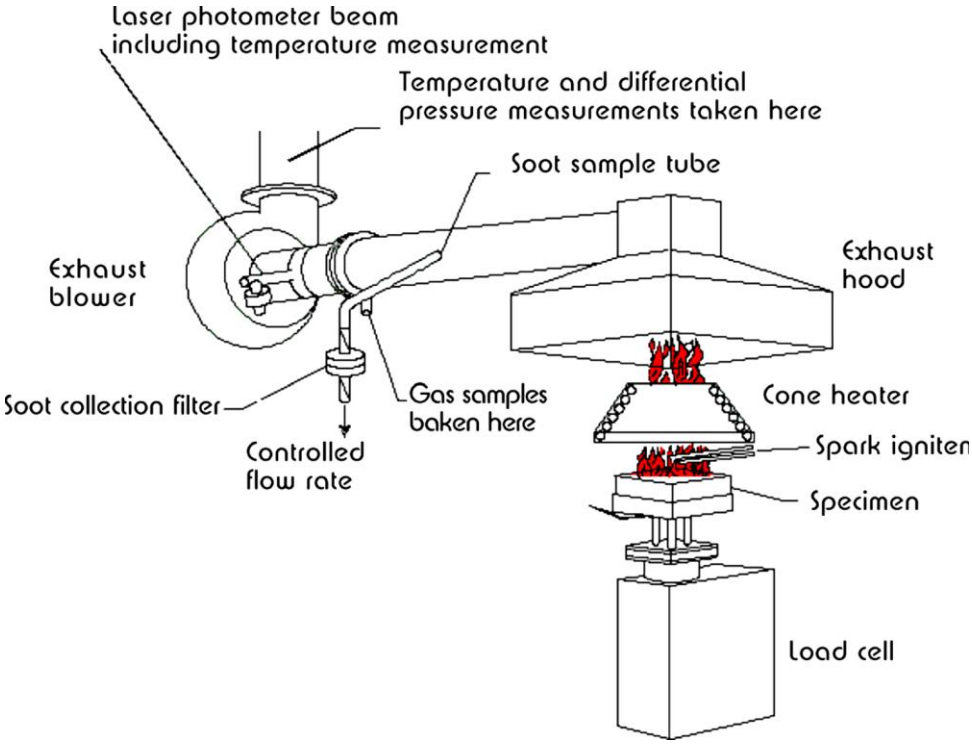

Figure 1.8. Schematic of a Cone Calorimeter [18].

1.3.2 Microscale Combustion Calorimetry (MCC)

To assess the fire safety of aircraft materials, the U.S. Federal Aviation Administration (FAA) developed microscale Pyrolysis-Combustion Flow Calorimetry (PFCC) which was later referred to as Microscale Combustion Calorimetry (MCC). MCC measures heat release parameters using only milligram sized samples (typically 2-5 mg) [21, 22]. ASTM 7309 is the primary standard for the MCC tests. Similarly to cone calorimetry, the heat release rate during combustion and the total heat release are also calculated using oxygen consumption rate and integration of the heat release rate versus time. The MCC reproduces the gas phase and condensed phase of a combustion process by using two connected heating zones shown in Figure 1.9. Method A and method B are two different test methods for MCC, only method A will be discussed in the following context

because it is the most commonly used in publications. More information about the method B can be found in [16].

Samples are placed in the prolyzer where a constant rate of heating is applied in a nitrogen environment. After the decomposition temperature of the polymer is reached, combustibles from the decomposition product flow into the combustor where the combustion will take place in a mixture of oxygen and nitrogen.

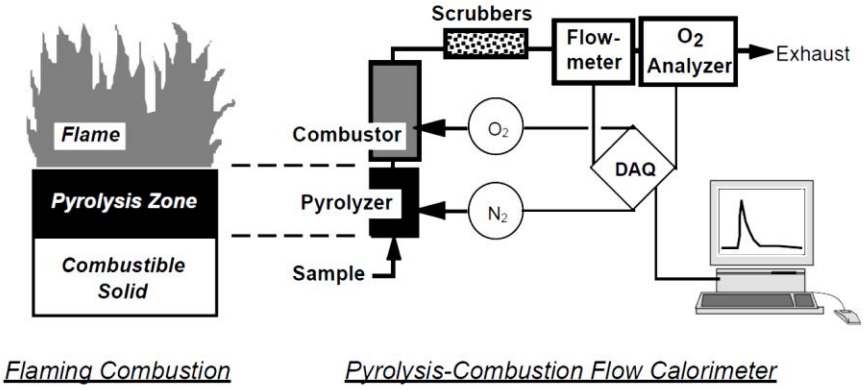

Figure 1.9. Illustration of Micro-Combustion Calorimeter working principle [21].

The typical output parameters from MCC are heat release capacity (HRC), heat release rate (HRR), peak heat release rate (PHRR), PHRR temperature and total heat release (THR). Heat release capacity is indicative of the maximum heat release potential of a material in a combustion process. It is an intrinsic material property independent of sample size and heating rate. It is defined as:

$$\eta_c = \frac{Q_{max}}{\beta} = \frac{h_c^0}{\Delta T_p} \tag{1.4}$$

Where Q_{max} is the maximum specific heat release rate, β is the heating rate, h_c^0 is the heat of complete combustion of the pyrolysis gases, and ΔT_p is pyrolysis temperature interval.

1.3.3 Vertical UL-94 Test

Developed by the "Underwriters Laboratories", UL-94 is a commonly used industry standard to test the flammability of plastic materials and their tendency to either self-extinguish or spread the flame once the specimen has been ignited. UL-94 refers to a series of test that includes small and large flame vertical tests, horizontal tests for bulk, and foamed materials and radiant panel flame-spread tests [18]. The most common UL-94 test is the small flame vertical test in which a 1.27 cm × 12.7 cm (1/2" × 5") specimen is held at one end in the vertical position as a burner flame is applied at its free end for two 10-second intervals, separated by the time it takes for flaming combustion to cease after the first application (Figure 1.10). The three ratings, V-2, V-1 and V-0 (best) indicate that the material was tested in a vertical position and self-extinguished within a specified time after the ignition source was removed (Table 1.1). These ratings also indicate whether the test specimen dripped flaming particles that ignited a cotton indicator located below the sample [23]. UL-94 requires five specimens to be tested for each sample for a final V rating to be reported.

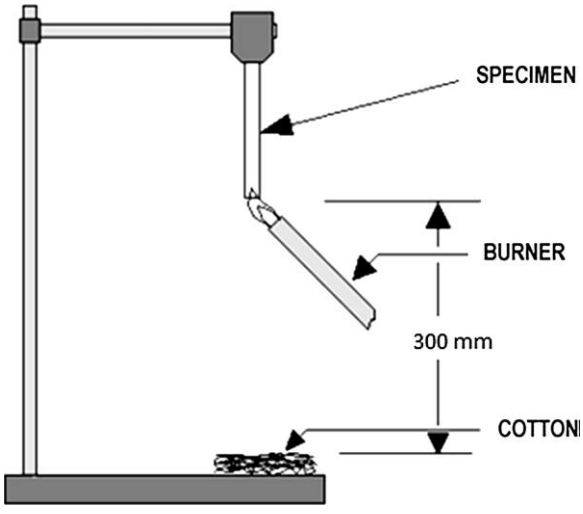

Figure 1.10. Illustration of a vertical UL-94 test set up.

Table 1.1. Classification criteria for the UL 94 flammability test.

Criteria	**V-0**	**V-1**	**V-2**
Afterflame for each individual specimen (t_1 and t_2)	≤ 10s	≤ 30s	≤ 30s
Total afterflame for any condition set ($t_1 + t_2$ for the 5 specimens)	≤ 50s	≤ 250s	≤ 250s
Afterflame plus afterglow time for each individual specimen after the second flame application	≤ 30s	≤ 60s	≤ 60s
Afterflame or afterglow of any specimen up to the holding clamp	No	No	No
Cotton indicator ignition	No	No	Yes

1.3.4 Limiting Oxygen Index (LOI) Test

As one of the few test apparatuses where steady burning conditions can be replicated on a small scale, LOI remains as an important tool to characterize materials flammability in the plastics industry [18]. The concept of limiting oxygen index (LOI) was introduced in 1966 by Fenimore and Martin from General Electric Research and Development Center. Standardized as ASTM D2863, LOI is a method to numerically describe the flammability of materials that burn in a "candle-like" way. It is also known as "Critical Oxygen Index" or simply "Oxygen Index". The LOI is defined as the minimum concentration of oxygen, expressed as a percentage that will support combustion of the sample:

$$LOI = 100 \times \frac{[O_2]}{[O_2] + [N_2]} \tag{1.5}$$

The LOI is measured by passing a mixture of oxygen and nitrogen over a burning specimen, and reducing the oxygen level until a critical level is reached (Figure 1.11). A

higher LOI indicates the materials need higher oxygen to support combustion, thus demonstrating a better flame retardant property. Since the oxygen concentration in air is 21%, any materials with LOI less than 21 will likely to be combustible while materials with LOI higher than 21 are considered self-extinguishing [18].

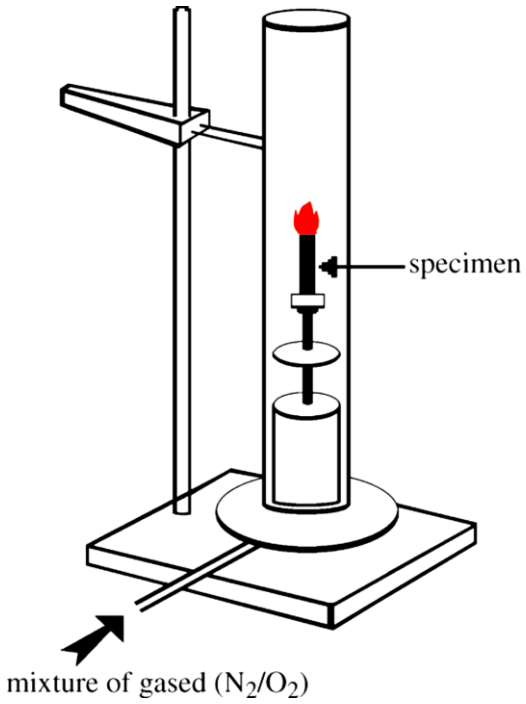

Figure 1.11. Illustration of a LOI set-up.

1.3.5 Relationships among Different Flammability Tests

Efforts have been made to establish correlations between flammability tests. UL-94 and LOI are commonly used small-scale methods for flammability evaluation of polymeric materials. However, these values are not intrinsic material properties because the results can be affected by sample geometry including thickness. Thicker samples tend to yield better UL-94 rating and higher LOI values. Although both tests examine materials' self-extinguishing properties, the main difference between UL-94 and LOI is that samples

in a UL-94 test are subject to upward flame, whereas in a LOI test a downward flame is enforced. Figure 1.12 shows typical LOI values of some commodity and engineering polymers including nylon. Since the oxygen concentration in air is 21, materials with LOI less than 21 will be combustible in an open fire condition [18]. On the other hand, not all polymers with LOI above 21 can self-extinguish in air. According to Bernhard [16], materials with higher LOI are more likely to self-extinguish and 27 (dashed line in Figure 1.12) is used as a reference line for determination of flammability. In another research, Lin et al. found that materials with LOI greater than 30 are likely to have UL-94 V-0 rating [24]. However, no well-defined relationship between LOI and UL-94 has been established: materials with LOI as low as 22 have been reported to self-extinguish while other materials with LOI as high as 47 have been reported as flammable [16].

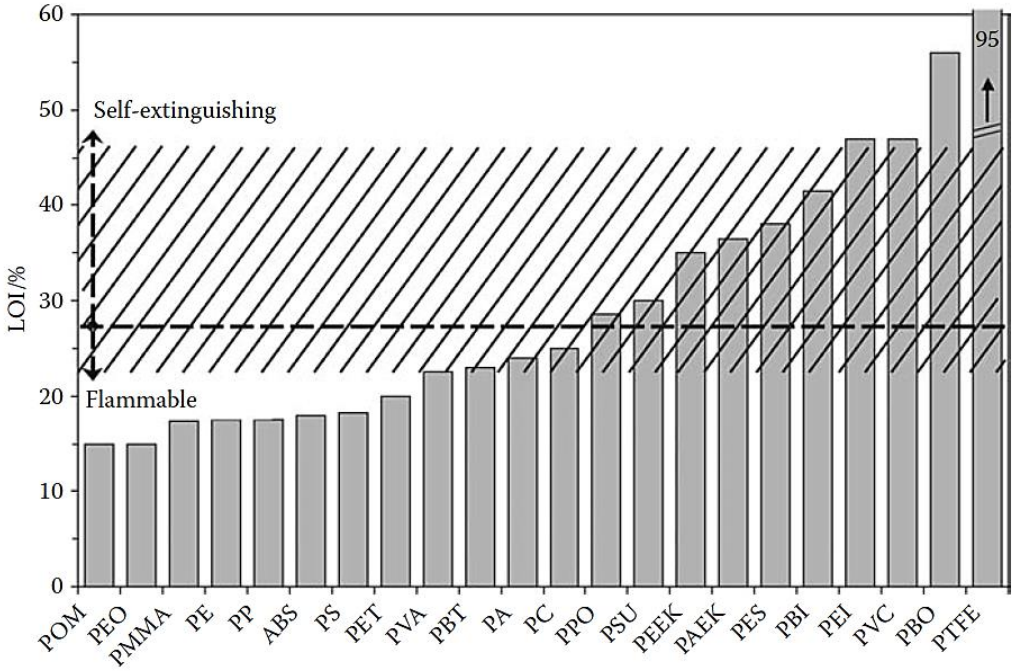

Figure 1.12. Typical LOI values of some polymers [16] (page 391).

Unlike LOI or UL-94 in which the sample does not undergo complete combustion, MCC is a complete combustion test method. Lyon et al. [22] studied the relationship between MCC, UL-94 and LOI results on different polymers. They found that HRC (η_c) from the MCC test cannot be used as a unique criterion for either UL-94 or LOI. Figure 1.13 compares MCC heat release capacity versus UL-94 ratings of different polymers. For polymers with the same UL-94 V-0 rating, the HRC varies in a large extent from 30 J/g-K to more than 500 J/g-K. For other UL-94 ratings (i.e. V1, V2 and NR/HB), there seems to be a lower threshold of HRC at about 200 J/g-K. This indicates a relatively poor correlation between UL-94 and MCC results, although there appears to be an overall increase in HRC with the poor UL-94 ratings.

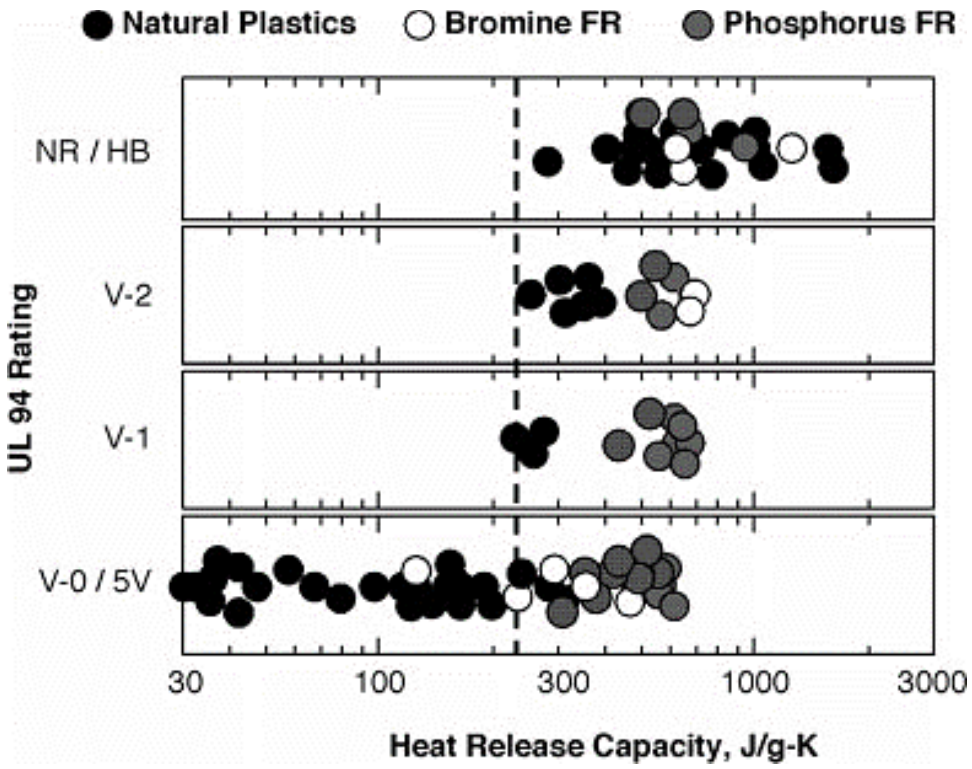

Figure 1.13. UL-94 rating versus heat release capacity of different polymers (the dashed line indicate lower threshold for self-sustained ignition, $\eta_c \approx 200\ \mathrm{Jg^{-1}K^{-1}}$) [22].

Lyon et al. [25] also reported that the LOI and HRC (η_c) can be affected by the burning efficiency and temperature at maximum pyrolysis rate (T_{max}). Figure 1.14 shows the LOI versus HRC of 50 different polymers. LOI is inversely related to HRC and a simple power law $LOI = 125/{\eta_c}^{1/4}$ was used to fit this relationship with moderate accuracy (R=0.84). In many cases, materials with LOI larger than 30 are likely to have $\eta_c < 200\ \mathrm{Jg^{-1}K^{-1}}$.

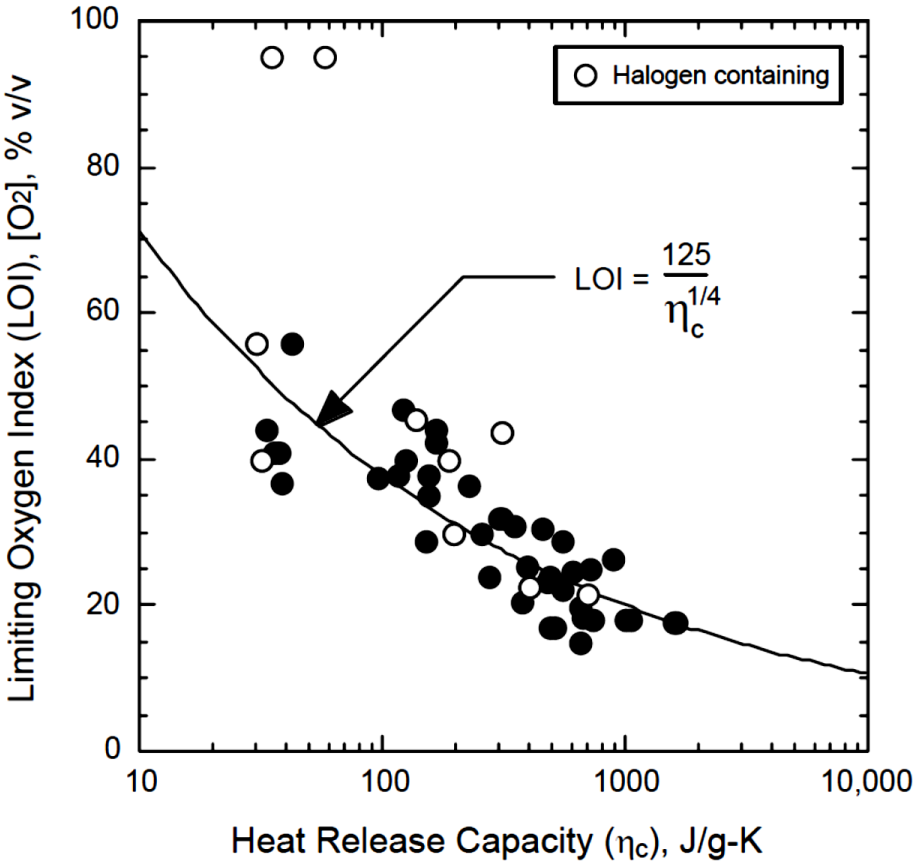

Figure 1.14. LOI versus HRC for 50 polymers [25]. (Solid dots indicate pure polymer, circles indicate polymers with halogen FR additives).

In another research, Yang et al. [26] used Lyon's model (Equation 1.6) [27] to correlates the LOI values with MCC parameters of woven FR cotton and nylon fabrics. A correlation coefficient of R=0.99 was found between measured and calculated LOI values.

$$\mathrm{LOI} = \mathrm{OI} + \frac{\sigma T_{\mathrm{PHRR}}^4}{a} + \frac{\mathrm{HRR}^* \eta_g / a\chi^2}{(1-\mu)^2 \mathrm{HRC}} \tag{1.6}$$

In summary, different flammability tests may yield different results due to their different test conditions. Throughout this research, several flammability tests will be

conducted and their results will be compared to obtain a thorough understanding of the flame retardancy properties of the material.

1.4 FLAME RETARDANT SYSTEMS FOR POLYMERS

There are three approaches to achieve flame retardant polymers: 1. incorporation of flame retardant additives during compounding; 2. grafting flame retardant groups onto the polymer chain or surface; and 3. in-situ polymerization with flame retardant monomers. The first two methods have been utilized in the commercial production of nylons. In contrast, the third method has not seen widespread use due to high cost and property degradation [8]. Flame retardant additives for nylons are limited because of nylon's high sensitivity to acids. Other problems for flame retardant nylon include migration of the additive during processing and hydrolysis of the flame retardants due to high moisture absorption of nylons. Moreover, some flame retardants affect the crystallinity of nylon, therefore changing its physical properties as well [8].

1.4.1 Flame Retardant Additives

Flame retardant (FR) additives are used to impede or stop the combustion of polymers. Depending on the mechanism, flame retardants can be divided into two categories. The first category works by physical action which includes cooling, formation of a thermal shielding layer, and fuel dilution. The second category achieves FR function by chemical reaction in either condensed or gaseous phase. Taking advantage of the synergism between different flame retardants, a high performance FR system usually contains a combination of both physical and chemical mechanisms.

1.4.1.1 Halogen-Containing Flame Retardants

Halogen containing compounds are one type of widely used flame retardant additives. Although not fully understood yet, the mechanism to achieve flame retardancy

is related to the scission of the carbon-halogen bond. The order of thermal stability for the halogen compounds is F>Cl>Br>I. The bond energy for fluorine compound is too high that it will not help with FR performance during combustion, whereas the iodine compound is not thermally stable at polymer processing temperature. Therefore, the typical halogen contains brominated or chlorinated compounds [16]. Pearce et al. [28] summarized three mechanisms for the halogen-containing FR systems as:

1. Formation of chain-terminating free radicals.
2. Enhancement of char formation through dehydrogenation reactions.
3. Generation of hydrogen halides (HF, HBr, etc.) blocking the combination of fuel gas with condensed phase.

Although halogen containing flame retardants are among the most effective FR additives for many synthetic polymers, they are not as effective for nylon. Because hydrogen halides can cause severe degradation of the nylon polymer chains into small combustible molecules. Metal compounds together with high loadings of additives are often added to nylon to achieve satisfactory flame retardant properties. For electrical insulating application, halogenated nylons have a lower tracking index, which is a parameter to measure electrical breakdown [8].

The release of toxic hydrogen halide during combustion also makes halogenated FRs inappropriate for many applications. A paper published in 1977 in Science raised concerns on using such halogenated FR additives as they can be a carcinogen if absorbed through human skin [29].

1.4.1.2 Phosphorus-Containing Flame Retardants

Driven by increasing health and ecological safety concerns, non-halogenated flame retardants have been developed over the years. One type of non-halogenated flame

retardant additive is phosphorous based. This type of flame retardants is particularly effective when incorporated into oxygen containing polymers, such as polyamides and polyesters [30]. There are lots of varieties among phosphorous based flame retardants (Figure 1.15). They can be categorized into red phosphorus, inorganic phosphates, organic phosphorus based compounds, and various phosphorus-nitrogen intumescent products. An extensive list of different phosphorus based compounds used in nylon can be found in a review by Levchik and Weil [8]. One well known flame retardant for nylon is red amorphous phosphorus. With maximum activity at 7-8 wt%, it is considered extremely potent. However, because of the dark color of the red phosphorus, there has been difficulty in developing light colored materials [2]. For most phosphorous FRs, thermal decomposition will generate phosphoric acid and water. The phosphoric acid facilitates the dehydration reaction of the hydroxyl groups, which will lead to the formation of a carbonaceous char layer and to the dilution of the oxidizing gas by the resulting water vapor [18].

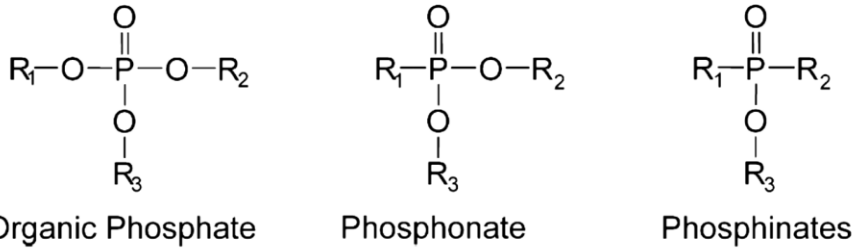

Figure 1.15. Chemical structure of some organic phosphorous based FRs [18].

Braun et al. [31] conducted a comprehensive study on the flame retardant mechanism of glass fiber reinforced PA6,6 compounded with aluminum phosphinate (AlPi), melamine polyphosphate (MPP) (Figure 1.16) as well as zinc borate (ZnB).

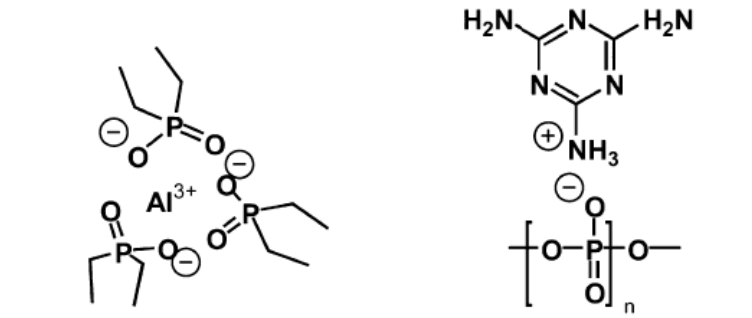

Figure 1.16. Chemical structure of AlPi and MPP [31].

The decomposition temperature of all formulations containing flame retardant shifted to lower range indicating strong interactions of PA66 with both MPP and AlPi. The evolved gas analysis indicated that the main degradation products of the composite were ammonia, carbon dioxide, cyclopentanone, hydrocarbons and methane. FTIR spectra of char residues at different decomposition stages suggested that ZnB suppressed the formation of aluminum phosphates during decomposition. Considering only the major decomposition pathways, two models were proposed based on thermal and hydrolytic decomposition pathways. Figure 1.17 shows the suggested decomposition pathway of PA66/GF-AlPi-MPP-ZnB. Because boron is the strongest Lewis acid, the addition of ZnB altered the reaction of MPP with AlPi resulting in boronphosphate, aluminumphosphate as well as vaporized AlPi and zinc oxide.

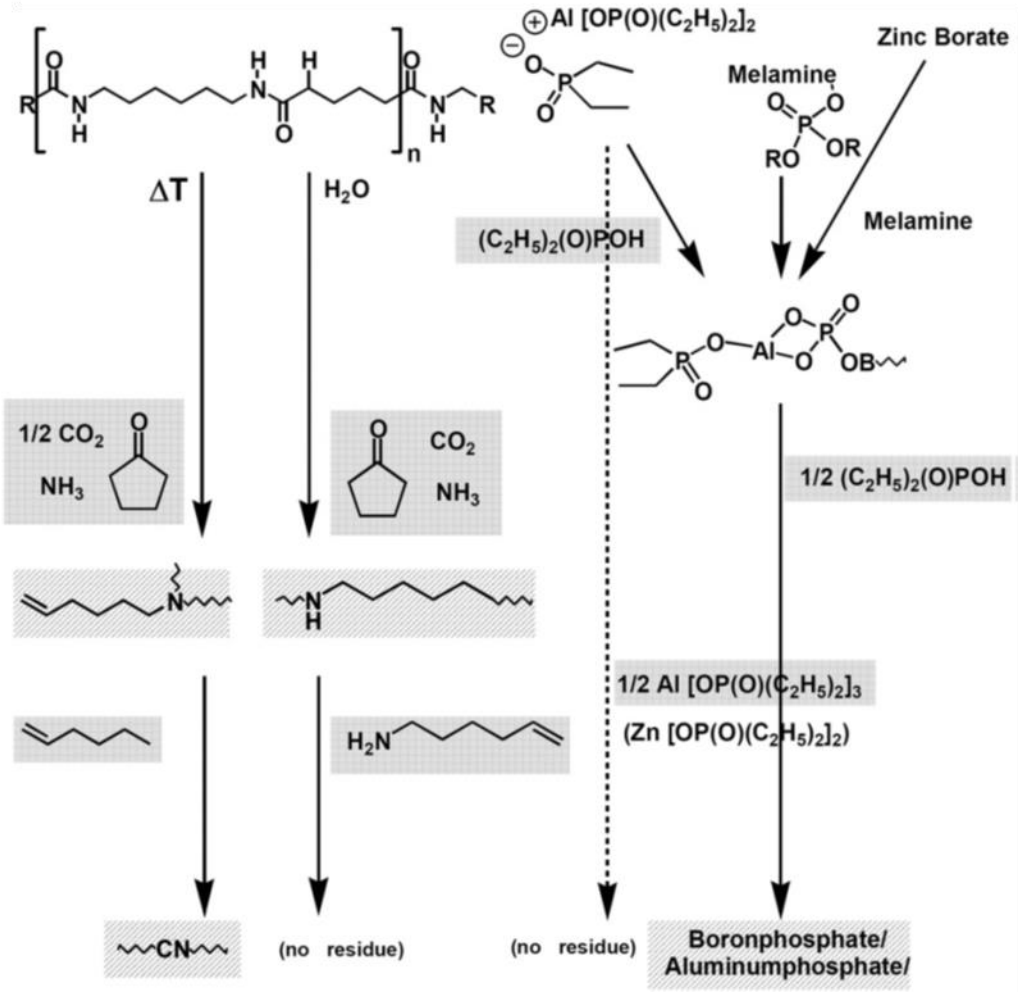

Figure 1.17. Decomposition pathway of PA66/GF-AlPi-MPP-ZnB [31].

Phosphorous intumescent systems act as a char forming agent and have been shown to have a synergistic effect when combined with nanoparticles, such as nanoclay and carbon nanotubes, whereby they combine to form a thermally insulating barrier on the polymer surface during combustion [18]. This synergistic effect will be discussed in more detail in Section 1.6.

1.4.2 Existing Flame Retardant Textiles

Flame retardant treatments of textiles date back to 1735 when borax, vitriol and other mineral based additives were patented to make flame retardant canvas and linen in the UK [32]. Since then, many more developments have been made particularly during the 20th century. In response to the institution of a series of government regulations on textile flammability standards in the early 1970s, researchers have developed many different approaches to produce flame retardant fibers. The three decades between 1950 and 1980 have witnessed the prolific development of various flame retardant treatment methods for natural and synthetic fibers, many of which are still of commercial relevance today [32, 33].

Current existing flame retardant treatments for textiles can be categorized into non-durable, semi-durable and durable treatments. Examples of durable treatments include Tetrakis (hydroxymethyl) phosphonium salts used on cotton, and nitrogen- and sulfur-containing polycondensates typically based on thiourea–formaldehyde formulations used in technical fabrics made of polyamide [33]. Those treatments were developed more than 50 years ago and require formaldehyde-based crosslinking resins [33, 34]. In particular, the THPX cross-linking chemistry presents a demanding treatment processes as well as production regulation and high cost challenges exemplified by the precondensate ammonia process, known as Proban [32-35].

Flame retardant finishes or back coatings of nylon fabrics have been available for many years. Some FR treatments of nylon are based on decabromodiphenyl oxide, antimony oxide, and a polymeric binder, while others use thiourea-formaldehyde thermally cured with acid catalyst, commercially known as FlameGuard® [7]. In addition to cost and processing difficulties, there have been growing concerns about potential leach of harmful

substances during wear or burning of FR textiles processed by various methods including formaldehyde resins and halogen and heavy metal containing treatments [29, 33, 34].

Research to resolve this issue focused on incorporating non halogenated FR additive or reactants into the fibers without the reliance on formaldehyde chemistry. For instance, Asrar has patented the use of a reactive intermediate (Figure 1.18 left) to graft phosphinate to the nylon polymer chain [36]. Another approach by Pickett and Stoddard incorporated a phosphine oxide-containing dicarboxylic acid in nylon 66 (Figure 1.18 right) [37]. The resulting FR nylon 66 fibers have promising properties, however this method is economically unfavorable [7].

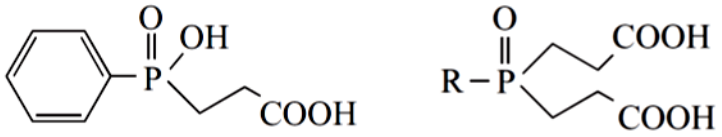

Figure 1.18. Chemical structures of FR modifiers for nylon fibers.

In a more recent study, Coquelle et al. [38] incorporated ammonium sulfamate (AS) into melt spun PA6 fibers. A 30.4% reduction in PHRR was observed for PA6 with 7% AS loading. One of the major challenges for the FR incorporated PA fiber processing is the degradation of mechanical properties. In this case, the tensile strength and elongation at break of the PA6/AS fibers are not affected when the AS loading is below 5%.

In addition to flame retardant modified textiles mentioned above, there are also commercially available high performance inherently flame retardant fibers, such as DuPont's Kevlar® and Normex®, DSM's Twaron® and PBI's poly(benzimidazole) [39]. Compared to surface treatment, high performance inherently flame retardant fibers have better flame resistance, and durability. Despite the exceptional properties of these flame

retardant fibers, high production costs limit their applications to niche markets such as high cost protective clothing for special military and firefighter uniforms.

To fill the gap between conventional FR treated textiles and high performance inherently FR fibers, there is a need for low cost flame retardant fibers based on widely used commodity and engineering polymers such as nylon. Indeed, an inherently FR and non-drip PA6 fiber could provide a cost-effective FR solution that extends beyond niche markets to encompass high-volume textile applications that benefit the society at large.

In this study, we will pursue this objective by capitalizing on the opportunities offered by novel solutions combining nanocomposite systems and commercially available flame-retardant additives that have been shown in previous research to achieve excellent FR properties in bulk plastics [40].

1.5 POLYMER NANOCOMPOSITES FOR FLAME RETARDANT APPLICATIONS

Polymer nanocomposites (PNC) are materials with nanofillers dispersed in the polymer matrix. These nanofillers with at least one dimension in the nanometer range [41] are used as reinforcements or as functional additives in the polymer matrix. It is well recognized that enhancements in properties, such as mechanical, thermal, electrical or chemical can be achieved by small loadings of nanofillers [42, 43]. Such nanofillers can be zero-dimensional particles (i.e., with all dimensions at the nanoscale or <100 nm), one-dimensional nanotubes (one dimension >100 nm), or two-dimensional nanoplatelets (two dimensions>100 nm). There is an extensive variety of nanofillers that have been used for different applications. For the application of flame retardants, nanoclay [18, 44, 45] and carbon nanotubes [42, 45] are the most commonly used nanofillers while POSS [42] and metal oxide nanoparticles [18, 45] have also been investigated.

1.5.1 Nanoclay

Since the Toyota group successfully made clay/nylon 6 nanocomposites by in-situ polymerization, polymer-clay nanocomposites have been extensively studied for their improved mechanical, thermal, and biodegradability properties [46, 47]. Some of the most promising applications of clay nanocomposites include flame retardant materials, such as FR coatings for electronics and electrical equipment [48, 49], and protective textiles [45].

Montmorillonite (MMT) is one of the most commonly used nanofillers for polymer nanocomposites because of its large surface to volume ratio. From this point, nanoclay or organoclay shall specifically refer to the MMT clay. MMT clay has a plate structure (Figure 1.19) which consists of an octahedral layer sandwiched between two silicate tetrahedral layers [43]. The octahedral layer in the middle is composed of an aluminum oxide sheet in which some aluminum atoms are replaced by magnesium. This composition variation creates negative charges in the sheet and the charges are balanced by positive ions, such as sodium ions between the platelets [43]. MMT clays have an irregular shape in the range of 100-200 nm in lateral direction; the thickness of single layer is about 1 nm [50].

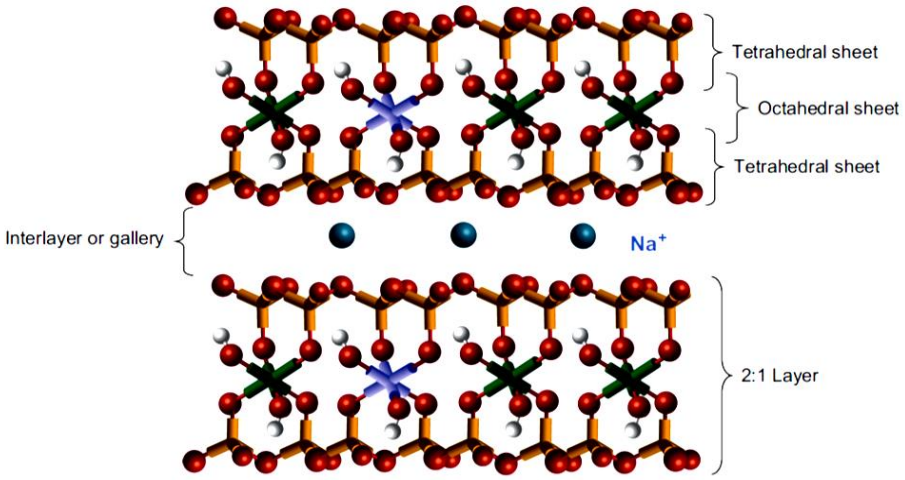

Figure 1.19. Illustration of MMT nanoclay structure [43].

Studies on MMT nanocomposites have shown that one of the most important factors affecting the properties of polymer-clay nanocomposites is the degree of nanoclay dispersion [51]. Figure 1.20 shows three typical dispersion states of nanoclay: 1. immiscible (microdispersed or microcomposite), 2. intercalated and 3. miscible or exfoliated. Immiscible nanoclays have micron sized aggregates that are composed of clusters of stacked clay platelets. The XRD pattern of immiscible nanoclay composites are usually identical to raw nanoclay powder. The regularity of packed clay platelets results in distinct 2θ angles peaks around 5° [52, 53]. Intercalated nanoclay usually has a lower 2θ peak from the original powder, and this is due to the expansion of d-spacing caused by the insertion of polymer chains or oligomers. Exfoliated nanoclay has individually separated clay platelets. Because there is no regularity in the clay platelets, XRD peaks of the nanoclay will not be detected in exfoliated nanoclay composites [43].

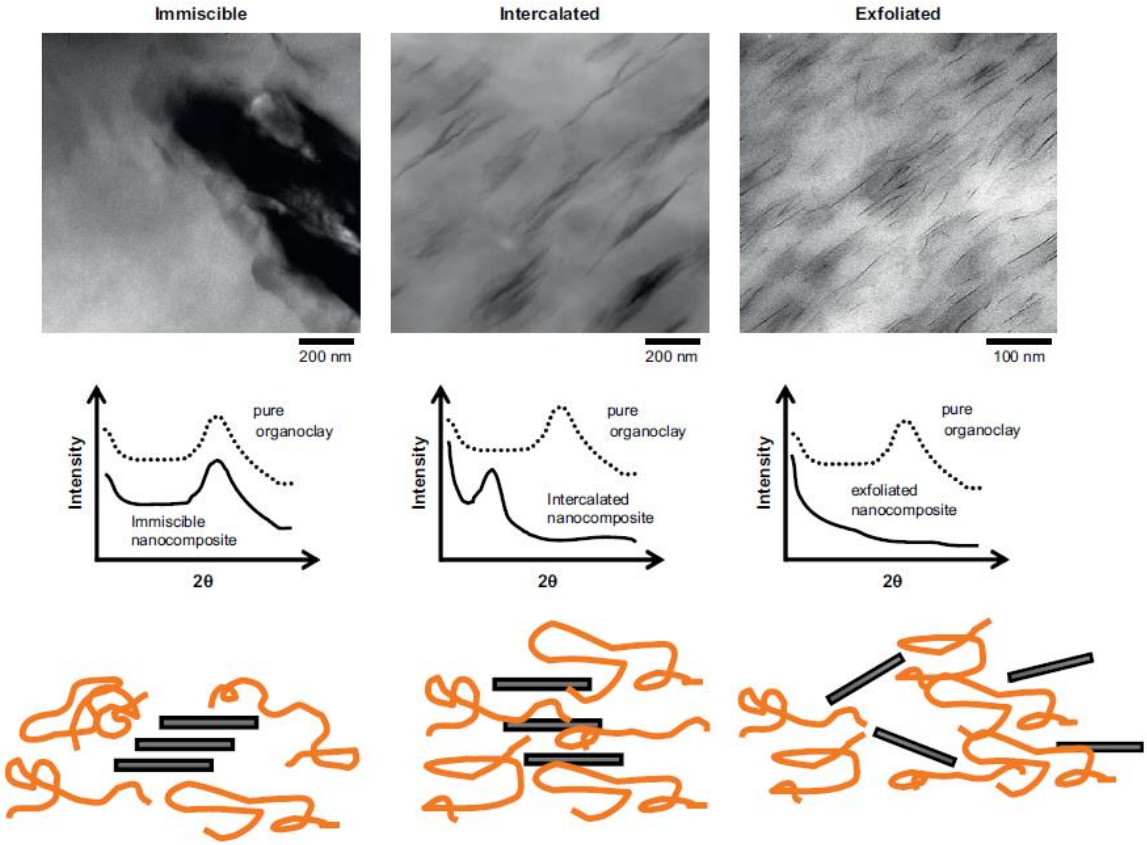

Figure 1.20. Nanoclay dispersion with corresponding WAXS and TEM [43].

Pristine MMT is not compatible with most polymer matrices, therefore, surface modification is necessary to obtain a high level of dispersion. Organic surface modification of clay is usually carried out by ion exchange reactions with primary, secondary, tertiary, or quaternary alkylammonium or alkylphosphonium in the interlayer spacing. This reaction will decrease the surface energy of the inorganic host and improve the affinity with the polymer matrix. The exfoliation of individual nanoclay layers can be achieved by in-situ polymerization or melt-extrusion. Paul et al. [43, 54] showed that PA6 has a good affinity with silicate surfaces modified by the method mentioned above, and therefore high levels of exfoliation can be achieved [51].

Gilman et al. pioneered the work of clay/nylon 6 nanocomposites for flame retardant application [44, 55]. A 63% reduction in heat release rate (HRR) and tougher char layer made of accumulated clay platelets was achieved when nylon 6 was filled with 5 wt% of nanoclay [44]. Thermal decomposition of the organomodifier creates strong protonic catalytic sites on the clay surface that facilitate the formation of a stable char layer [18, 56, 57]. In addition, exfoliated clay nanocomposites have an increased melt viscosity during burning, preventing dripping and helping with char formation [18]. This char layer formation was shown to effectively slow down heat transfer into the pristine polymer, as well as the release of combustible decomposition products, and oxygen diffusion into the material [18, 58-60].

Bourbigot et al. [61] compared cone calorimetry results of EVA nanocomposites with exfoliated MMT clays modified by methyl, tallow, bis-2-hydrooxyethyl, quaternary ammonium chloride (30B), and with micro-dispersed raw MMT (Na^+). EVA-Na nanocomposites reduced the peak heat release by 25% whereas the exfoliated EVA-30B achieved 50% reduction.

Zanetti et al. [58] summarized the flame retardant mechanism of clay/EVA nanocomposite as shown in Figure 1.21. In general, when a material is exposed to an external heat source or existing flame, thermal decomposition of the polymer material and the organoclay will take place. The decomposition of clay will produce protonic catalytic sites around the clay layer (step 1). After ignition occurs, the temperature of the material will keep increasing and the viscosity of the polymer melt on the burning surface will decrease. This allows for the decomposition products to escape from the material to support further combustion. However, this diffusion process will be slowed down by the organoclay because of a prolonged path through the clay layers. This phenomenon is called "labyrinth barrier effect" (step 2). As the viscosity keeps decreasing, the catalytic sites will

reassemble the clay layers close to the burning surface in a process the authors referred to as ablative reassembly (step 3). Higher molecular weight decomposition product polyenes will undergo catalyzed oxidative dehydrogenation, resulting in conjugated polyenes (step 4). A char layer will be formed by crosslinking and dehydrogenation of the conjugated polyenes (step 5). This char layer will be reinforced by the layered clay structure and a clay nanocomposite char layer is formed (step 6).

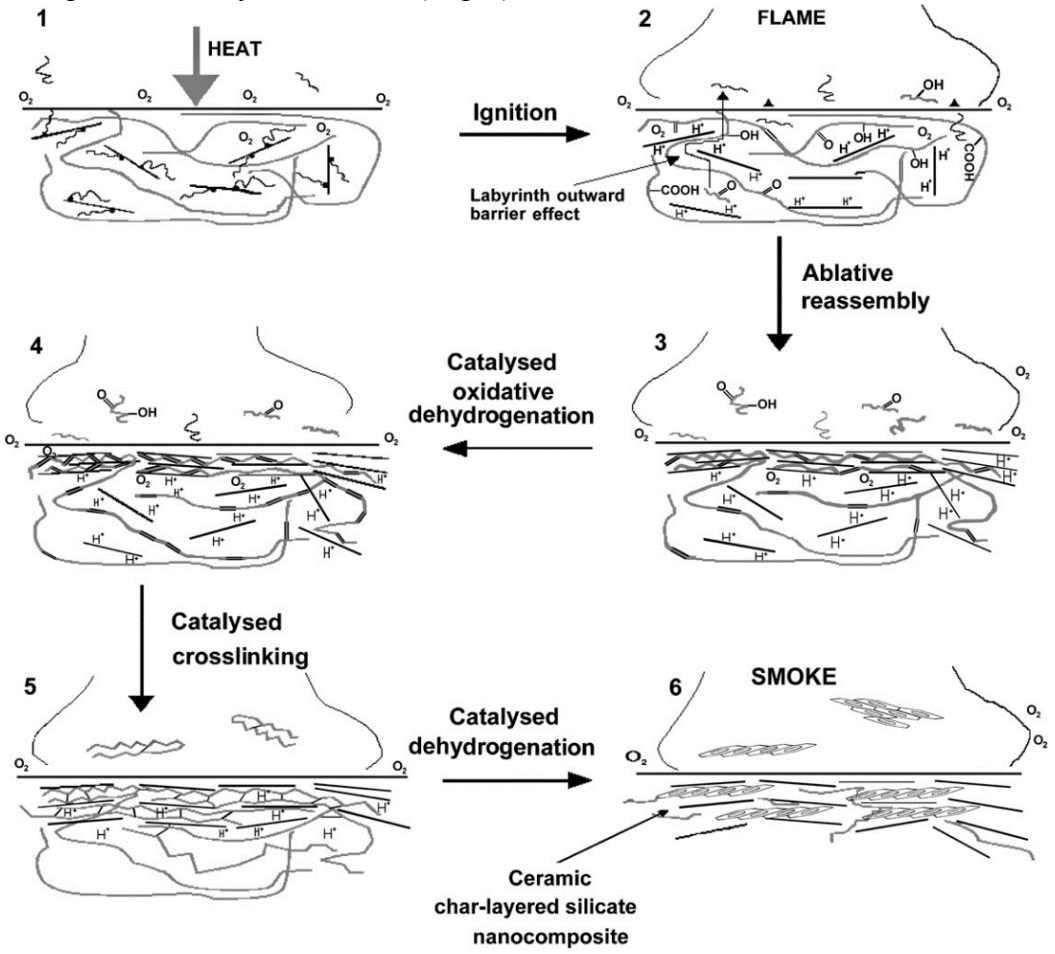

Figure 1.21. Schematic representation of flame combustion mechanism and ablative reassembly of clay nanocomposites [18, 58].

Kashiwagi et al. [62] studied the char formation mechanism of PA6/clay nanocomposites. They proposed that the clay-rich char layer could be caused by either pyrolysis of the polymer leaving the clay platelets on the surface or bursting bubbles of the polymer melt pushing the clay towards the surface. Lewin [59] also carried out a thorough investigation of the mode of formation of the char layers for PP/clay nanocomposites. He found that the migration of clay occurs at a temperature far below its pyrolysis temperature and could be caused by 3 factors: temperature and viscosity gradients of the melt; gas bubbles from the decomposing surfactant and polymer propelling the organically layered silicon to the surface; and difference in surface free energy between the polymer and the polymer/clay aggregate. Lewin also pointed out that migration depends on the amount of exfoliated clay particles and the nature of the surfactant.

1.5.2 Carbon Nanotubes (CNT)

Carbon nanotubes are one of the most widely studied one-dimensional nano-additives for flame retardant applications. Similar to nanoclays, a very small loading of CNTs (less than 3 wt%) was shown to improve flame retardant properties of a wide range of polymers because of their tremendously large aspect ratio [18]. There are two types of nanotubes: single-walled CNTs and multi-walled CNTs. Single-walled CNTs have smaller diameter (1-2 nm) and usually better performance than multi-walled CNTs (10-100 nm). However single-walled CNTs are considerably more expensive than their counterpart.

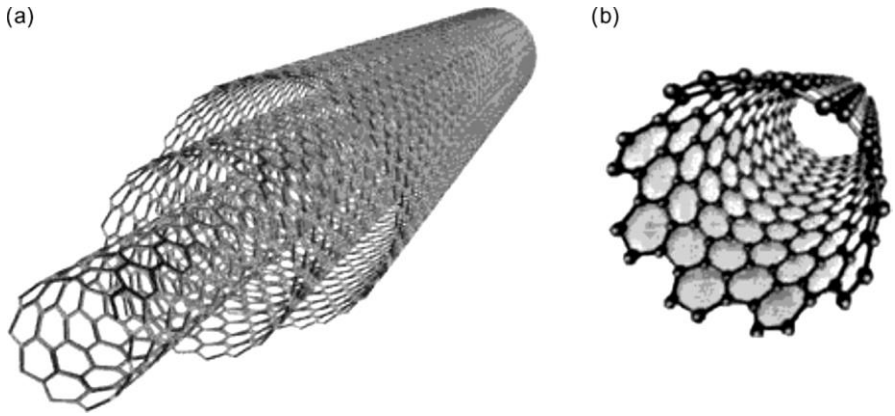

Figure 1.22. Structures of (a) multi-walled and (b) single-walled carbon nanotubes [18].

The FR mechanism and processing methods of CNT is somewhat analogous to that of nanoclay: a nanotube network formed during combustion functions as a thermal shield protecting the polymers from external heat flux. Kashiwagi et al. [63] showed that dispersion of CNTs could largely affect the flame retardant properties of PMMA/CNT nanocomposites. With only 0.5 wt% CNT loading, well-dispersed samples lowered heat release rate by more than 50%, whereas the poorly dispersed sample showed minimal effect on cone calorimetry results [63]. It was also pointed out that CNT loadings could affect the heat release rate. For PMMA nanocomposites at CNT loadings under 0.2 wt%, only discontinuous char layers were formed and this correlated with no change in the heat release curve obtained from cone calorimeter test. On the other hand, when CNT loadings reach a certain threshold level, a continuous char layer could be observed as shown in Figure 1.23 [64].

Laoutid et al. suggested that the flame retardant properties of CNT nanocomposites is governed by a balance of the shield property of the structural CNT network and the increased thermal conductivity [18].

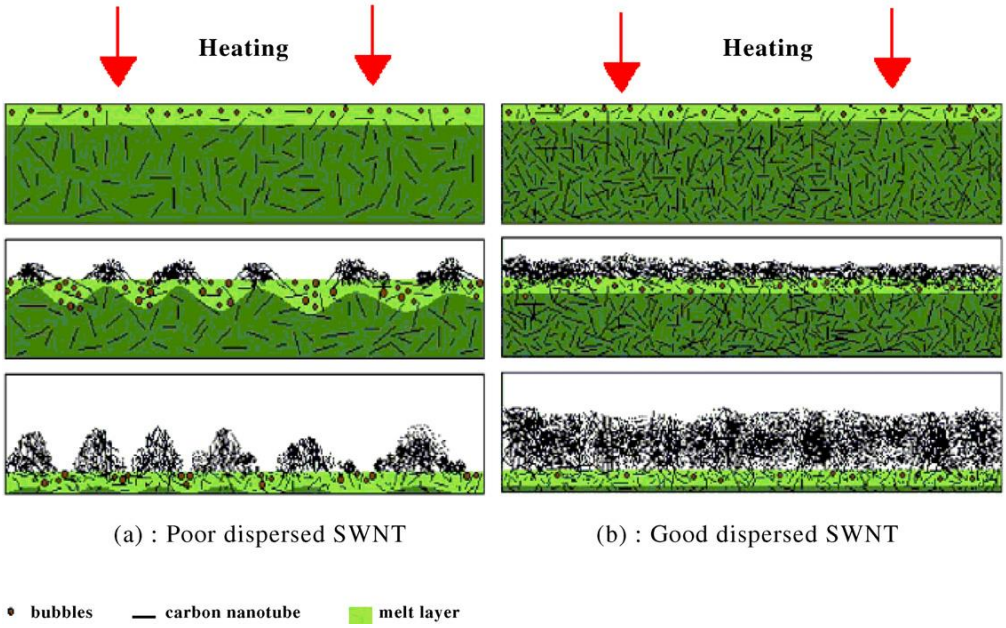

Figure 1.23. Schematic representation of the effect of CNT dispersion on char forming [64].

1.5.3 Other Nanoparticles

In addition to nanoclay and carbon nanotubes, other nanomaterials, such as POSS, halloysite nanotubes (HNT), graphene oxide, and metallic oxide nanoparticles have also been cited as promising nano-additives for FR nanocomposites.

Polyhedral oligomeric silsesquioxane (POSS) is a hybrid material that combines properties of both organic and inorganic materials [65]. It has drawn significant research interest recently due to its unique three-dimensional cage-like molecular structure. With general formula $(R\text{-}Si\text{-}O_{1.5})_n$ where R could be hydrogen or an organic group, such as alkyl or phenol, POSS can be tailored to be compatible with various polymers.

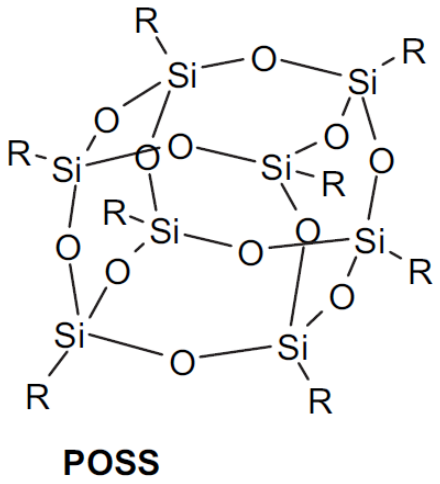

Figure 1.24. Structure of POSS (where R can be alkyl, aryl, cycloaliphatic, vinyl, amino, nitrile, halogen, alcohol, ester, isocyanate, glycidyl etc.) [43].

If homogeneously dispersed, POSS could improve thermal stability and tensile properties of many polymer matrices, such as polyolefin and polyamides [66]. Upon combustion, POSS promotes the formation of ceramic materials with high thermal stability which will act as a thermal barrier to impede the combustion process [18]. Unlike nanoclay or carbon nanotube (CNT) nanocomposites which suffer from substantial loss of ductility [40, 67], POSS nanocomposites can even enhance the elongation at break of PA6 [68]. Lichtenhan et al. [69] examined the flammability of POSS in polyether block amides polymer (PEBAX). The peak heat release rate of the nanocomposites observed using cone calorimetry was 77% lower than the neat polymer. Bourbigot et al. [70] showed that using 10wt% of Poly(vinylsilsesquioxane) POSS in thermoplastic polyurethane could decrease the PHRR by 80% through an intumescent mechanism.

Halloysite nanotubes (HNTs) is a naturally occurring tubular nanoparticle of aluminosilicate [$Al_2Si_2O_5(OH)_4 \cdot 2H_2O$]. HNTs are typically 0.5–5μm in length with an outer diameter of less than 100nm. Advantages of HNTs include high strength, high

ductility, low density, and low cost. Compared to other nanofillers, HNTs are less detrimental to the elongation and toughness properties of polymeric nanocomposite materials. Marney et al. [71] studied flame retardant properties of HNT/PA6 nanocomposites and cone calorimetry results showed that increasing concentrations of HNTs lead to a decrease in PHRR. However, HNTs did not alleviate the dripping of PA6 melt during burning. As a result, none of the samples passed UL94 V-0 regardless of HNT concentration.

Other nanoparticles tested for FR application include metal oxide, such as aluminum oxide, ferric oxide, and titanium dioxide. Laachachi et al. [72] studied the FR performance of titanium dioxide (TiO_2) and ferric oxide (Fe_2O_3) nanoparticles incorporated within poly(methyl methacrylate) (PMMA). The PHRR of the nanocomposite material was reduced by 50% with 20 wt% of TiO_2, while the same amount of Fe_2O_3 with similar morphology only decreased it by 37%. They attributed the reduced PHRR to the restriction of polymer chain mobility caused by the strong interaction between PMMA and the nanoparticles.

Overall, polymer nanocomposites appear to share a similar flame retardant mechanism regardless of the type of nanofillers. Based on current literature, even though nanoclay and carbon nanotube reinforced nanocomposites usually exhibit lower PHRR as measured by cone calorimetry, there is no reduction in total heat release. In addition, shorter times to ignition have been observed in some cases. Many researchers have pointed out that the incorporation of nanoparticles alone often falls short of meeting minimum requirements of FR regulations and standards, such as UL 94 and LOI [18, 42, 73, 74], although it improves thermal stability and reduces the peak heat release rate. Therefore, combinations of nanofillers and conventional FR additives have been envisaged as an alternative approach.

1.6 SYNERGY BETWEEN CONVENTIONAL FR AND NANOPARTICLES

Combinations of conventional flame retardants such as intumescent additives in conjunction with small amount of nano-fillers could result in favorable FR performances. Because nanoparticles have high aspect ratio, they can act as reinforcement for the existing intumescent char layer. The reinforced char shield could further reduce the total heat release in addition to the PHRR [40, 67, 75-78]. To achieve the same flame retardant property, the synergistic effect can lower the necessary amount of conventional FR loading while potentially yielding better mechanical properties like ductility [75]. For example, Duquesne et al. [79] showed that nanoclay could largely improve the UL94 ratings of the EVA/APP/PA6 intumescent system from unclassified to V-0, the best UL94 rating available. The synergistic action was explained by an increased mechanical stability of the intumescent char layer. Laachachi et al. [72] studied the synergistic effect of alumina (Al_2O_3) and titanium oxide (TiO_2) combined with aluminum phosphinate (AlPi) in PMMA. Partial substitution of AlPi with alumina nanoparticles achieved the synergistic effects, while no significant difference was observed in the case of TiO_2 (Figure 1.25). Posttest specimens of alumina nanocomposite have a continuous char layer covering the entire sample surface while the TiO_2 samples were only partially covered.

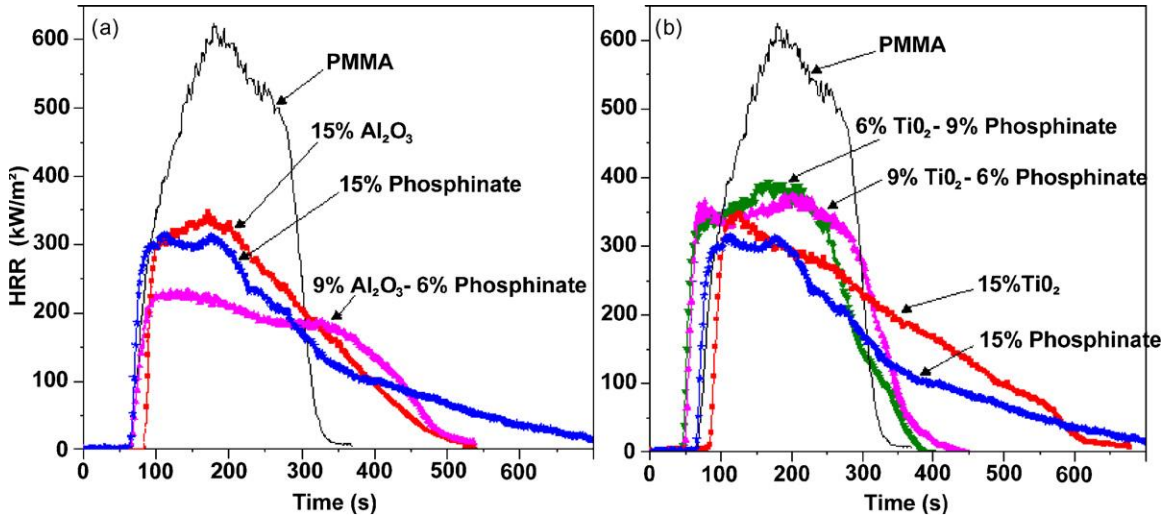

Figure 1.25. Cone calorimeter curves for combinations of phosphinate (Exolit OP 930, Clariant) with (a) Al_2O_3 and with (b) TiO_2 in PMMA (35 kW/m^2) [72].

1.7 RUBBER TOUGHENING

Thermoplastic elastomers can be used as a modifier for engineering thermoplastics including nylons to tailor the mechanical properties. Rubber toughening of semi-crystalline nylon 6 has been extensively studied [80-83]. The toughening mechanism was explained by preferential crystalline orientation along the rubber-matrix interface [83]. Ahn and Paul [80] reported on the use of a maleated elastomer in which the maleic anhydride reacts with the amine groups in nylon to form a block copolymer with good interfacial strength between the two phases. It was found that rubber toughening could effectively enhance the Izod impact strength, while a steady decrease in tensile strength and modulus occurs as the loading of elastomers increases [80-82]. Rubber toughened thermoplastics are also reported to have improved elongation at break, although in some cases the trend was not obvious because of factors, such as the potential introduction of impurities and defects during the melt blending process [84]. It has been demonstrated that the changes in mechanical properties are closely related to the microstructure of the blend, including

rubber particle size, particle concentration, and inter-particle distance [85-87]. Processing conditions can also have a significant impact on the toughened polymer properties. For instance, because of its high shear strength, twin-screw melt blending has the capability to yield smaller rubber particles than single-screw extrusion and therefore results in better enhancement in elongation at break [84]. It was reported that the impact of rubber particle size may vary with the molecular weight of nylon 6 and the type of elastomer [80]. Other factors that may impact the toughening process include the type of reinforcement and targeted functionalities of the composite systems. For instance, there has been a rich body of work on the use of rubbers to recover toughness of glass-fiber-reinforced composites [88], or more recently of organoclay/nylon 6 nanocomposites [89-91]. On the other hand, there has been little work specific to the functionality targeted in our nanocomposite system, i.e., on the impact on flammability of incorporating elastomers into FR thermoplastic composite systems.

1.8 OBJECTIVE

Based on the above discussion, effective durable FR and non-drip nylon fibers and fabrics remain unavailable for high volume applications in spite of the pressing need for them. Although various durable FR finishes have been developed in the 1950-1980 (as discussed in Section 1.4.2), cost-effective flame retardant nylon and nylon blend fabrics remain a challenge [92]. Apparel currently designed for and used in intense heat/flame environments, e.g., fire fighters, first responders and military personnel, are woven from extremely durable, meta-aramid (Nomex®) or polybenzimidazole (PBI) fibers that are inherently flame-resistant. While these staple fibers provide remarkable thermal and mechanical performance in these extreme environments, they are currently prohibitively expensive for widespread use.

Progress made in the area of polymer nanocomposites offers opportunities to meet the need described above. Recent developments could enable the formulation of non-drip inherently FR PA6 fibers as a cost-effective alternative for use in high volume FR fabrics. This research aims to explore the processing of nanocomposite fibers for the purpose of creating flame retardant textiles and study the *processing-structure-performance* relationship of the composite materials. The goal is to develop methods to produce intrinsically flame retardant non-dripping nylon 6 nanocomposite fibers. The inclusion of nanoparticles, such as nanoclay, carbon nanotubes (CNT) and POSS into polymers has been extensively studied by many researchers, however, there is limited literature that focuses on the flame retardant nanocomposite fibers. Transferring the knowledge of nanocomposites from bulk to fiber materials offers the potential to produce higher performance fibers based on existing thermoplastics. The resultant product will be beneficial for making low cost protective clothing or other related products.

This dissertation include 5 chapters. The first chapter provides an overview and background information of this research. The FR nylon nanocomposite systems we developed in this research were first tested and optimized in bulk material form in order to select a subset of formulations for fiber spinning. Thus, Chapter 2 presents the *processing-structure-performance* relationship of injection molded FR PA6 nanocomposite formulations. In particular, the balance between mechanical properties and flame retardant performance will be discussed. In Chapter 3, two isoconversion methods based on multiple heating rate TGA results were used to characterize the thermal stability of the flame retardant formulations. The effect of each component in the system will be discussed. Melt spinning process for the FR nylon 6 fibers is described in Chapter 4. Two set of non-drip FR fibers with different diameters were successively manufactured and characterized. Finally, Chapter 5 will summarize the results from previous chapter and discuss about the

significant of this research. To expand the scope of the current research, some future works are recommended.

1.9 REFERENCES

[1] T.F.Y. GmbH, The Fiber Year 2015, The Fiber Year GmbH, (2015).
[2] I.K. Melvin, M.I. Kohan, Nylon Plastics Handbook, Hanser/Gardner Publications (1995).
[3] M.N. Grigg, Thermo-oxidative degradation of polyamide 6, (2006). PhD dissertation, Queensland University of Technology.
[4] T.D. Fornes, D.R. Paul, Crystallization behavior of nylon 6 nanocomposites, Polymer 44(14) (2003) 3945-3961.
[5] E. Piorkowska, G.C. Rutledge, Handbook of polymer crystallization, John Wiley & Sons (2013).
[6] Spherulite. <https://commons.wikimedia.org/wiki/File:Spherulite2.PNG>, (2016).
[7] E.D. Weil, S. Levchik, Current Practice and Recent Commercial Developments in Flame Retardancy of Polyamides, Journal of Fire Sciences 22(3) (2004) 251-264.
[8] S.V. Levchik, E.D. Weil, Combustion and fire retardancy of aliphatic nylons, Polymer International 49(10) (2000) 1033-1073.
[9] N.F.P.A. (NFPA), Fires in the U.S., www.nfpa.org, (2015).
[10] H.H.G. Jellinek, The combustion of organic polymers, C. F. Cullis and M. M. Hirschler, Eds., Oxford university press, London, 1981, Journal of Polymer Science: Polymer Letters Edition 20(11) (1982) 606-606.
[11] S.V. Levchik, E.D. Weil, M. Lewin, Thermal decomposition of aliphatic nylons, Polymer International 48(7) (1999) 532-557.
[12] R.S. Lehrle, I.W. Parsons, M. Rollinson, Thermal degradation mechanisms of nylon 6 deduced from kinetic studies by pyrolysis-g.c, Polymer Degradation and Stability 67(1) (2000) 21-33.
[13] B.J. Holland, J.N. Hay, Thermal degradation of nylon polymers, Polymer International 49(9) (2000) 943-948.
[14] R.D. Davis, J.W. Gilman, D.L. VanderHart, Processing degradation of polyamide 6/montmorillonite clay nanocomposites and clay organic modifier, Polymer Degradation and Stability 79(1) (2003) 111-121.
[15] F. Fiala, J. Králíček, The influence of a cation on thermal degradation of anionic polymerizates of ε-caprolactam, Collection of Czechoslovak Chemical Communications 40(4) (1975) 1155-1162.
[16] C.A. Wilkie, A.B. Morgan, Editors, Fire Retardancy Of Polymeric Materials, Second Edition, CRC Press (2010).
[17] J.G. Quintiere, Fundamentals of Fire Phenomena, John Wiley & Sons Ltd. (2006).
[18] F. Laoutid, L. Bonnaud, M. Alexandre, J.M. Lopez-Cuesta, P. Dubois, New prospects in flame retardant polymer materials: From fundamentals to nanocomposites, Materials Science and Engineering: R: Reports 63(3) (2009) 100-125.
[19] A.M. Calcraft, K. Maries, Burning of plastics. Part II A mathematical model of thermal response, Plast. Polym 42 (1974) 247.
[20] C.J. Hilado, Flammability handbook for plastics, CRC Press (1998).
[21] R.E. Lyon, R.N. Walters, A microscale combustion calorimeter, National Technical Information Service (NTIS), Springfield, Virginia 22161, (2002).

[22] R.E. Lyon, R.N. Walters, S.I. Stoliarov, Screening flame retardants for plastics using microscale combustion calorimetry, Polymer Engineering & Science 47(10) (2007) 1501-1510.
[23] S. C. Lao, J. H. Koo, T. J. Moon, M. Londa, C. C. Ibeh, G. . Wissler, a.L. Pilato, Flame-retardant Polyamide 11 Nanocomposites: Further Thermal and Flammability Studies, J. of Fire Sciences 29(6) (2011) 479-498.
[24] T.S. Lin, J.M. Cogen, R.E. Lyon, Correlations between microscale combustion calorimetry and conventional flammability tests for flame retardant wire and cable compounds, Proceedings of the 56th IWCS, (2007).
[25] R.E. Lyon, M.L. Janssens, Polymer Flammability, National Technical Information Service (NTIS), Springfield, Virginia 22161, Washington, DC 20591, (2005).
[26] C.Q. Yang, Q. He, Applications of micro-scale combustion calorimetry to the studies of cotton and nylon fabrics treated with organophosphorus flame retardants, Journal of Analytical and Applied Pyrolysis 91(1) (2011) 125-133.
[27] R.E. Lyon, R.N. Walters, S.I. Stoliarov, Thermal analysis of flammability, Journal of Thermal Analysis and Calorimetry 89(2) (2007) 441-448.
[28] E. Pearce, Flame-retardant polymeric materials, Springer Science & Business Media (2012).
[29] A. Blum, B.N. Ames, Flame-retardant additives as possible cancer hazards, Science 195(4273) (1977) 17-23.
[30] H.F. Mark, J.I. Kroschwitz, Encyclopedia of polymer science and engineering, Wiley (1986).
[31] U. Braun, B. Schartel, M.A. Fichera, C. Jäger, Flame retardancy mechanisms of aluminium phosphinate in combination with melamine polyphosphate and zinc borate in glass-fibre reinforced polyamide 6,6, Polymer Degradation and Stability 92(8) (2007) 1528-1545.
[32] E.D. Weil, S.V. Levchik, Flame Retardants in Commercial Use or Development for Textiles, Journal of Fire Sciences 26(3) (2008) 243-281.
[33] A.R. Horrocks, Flame retardant challenges for textiles and fibres: New chemistry versus innovatory solutions, Polymer Degradation and Stability 96(3) (2011) 377-392.
[34] A.R. Horrocks, B.K. Kandola, P.J. Davies, S. Zhang, S.A. Padbury, Developments in flame retardant textiles – a review, Polymer Degradation and Stability 88(1) (2005) 3-12.
[35] W. Wu, Flame retardant finishing for cotton using a hydroxy-functional organophosphorus oligomer, PhD dissertation, Dept. of Textiles, Merchandizing and Interiors, The University of Georgia, Athens, GA, (2004) p. 213.
[36] J. Asrar, Polymer-bound non-halogen fire resistant compositions, US Patent US 5750603 A , (1998).
[37] O.A. Pickett Jr, J.W. Stoddard, Phosphorus-containing copolyamides and fibers thereof, US Patent US 4092302 A , (1977).
[38] M. Coquelle, S. Duquesne, M. Casetta, J. Sun, S. Zhang, S. Bourbigot, Investigation of the decomposition pathway of polyamide 6/ammonium sulfamate fibers, Polymer Degradation and Stability 106 (2014) 150-157.

[39] W.C. Smith, High Performance and High Temperature Resistant Fibers-Emphasis on Protective Clothing, Industrial Textile Associates, (1999) p. 17.
[40] H. Wu, X. Yin, M. Krifa, M. Londa, J. Koo, Fabrication and Characterization of Flame Retardant Polyamide 6 Nanocomposites via Electrospinning, SAMPE TECH 2011, Fort Worth, TX, (2011).
[41] IUPAC. Compendium of Chemical Terminology, 2nd ed. (the "Gold Book"). Compiled by A. D. McNaught and A. Wilkinson. Blackwell Scientific Publications, Oxford (1997). XML on-line corrected version: http://goldbook.iupac.org (2006-) created by M. Nic, J. Jirat, B. Kosata; updates compiled by A. Jenkins. ISBN 0-9678550-9-8. doi:10.1351/goldbook.).
[42] S. Bourbigot, S. Duquesne, C. Jama, Polymer Nanocomposites: How to Reach Low Flammability?, Macromolecular Symposia 233(1) (2006) 180-190.
[43] D.R. Paul, L.M. Robeson, Polymer nanotechnology: Nanocomposites, Polymer 49(15) (2008) 3187-3204.
[44] J.W. Gilman, T. Kashiwagi, J.D. Lichtenhan, Nanocomposites: a revolutionary new flame retardant approach, Sampe Journal 33 (1997) 40-46.
[45] M. Norouzi, Y. Zare, P. Kiany, Nanoparticles as effective flame retardants for natural and synthetic textile polymers: application, mechanism, and optimization, Polymer Reviews 55(3) (2015) 531-560.
[46] A.B. Morgan, Flame retarded polymer layered silicate nanocomposites: a review of commercial and open literature systems, Polymers for Advanced Technologies 17(4) (2006) 206-217.
[47] B.N. Jang, C.A. Wilkie, The effect of clay on the thermal degradation of polyamide 6 in polyamide 6/clay nanocomposites, Polymer 46(10) (2005) 3264-3274.
[48] S. Bourbigot, E. Devaux, X. Flambard, Flammability of polyamide-6/clay hybrid nanocomposite textiles, Polymer Degradation and Stability 75(2) (2002) 397-402.
[49] F. Dabrowski, M. Le Bras, R. Delobel, J.W. Gilman, T. Kashiwagi, Using clay in PA-based intumescent formulations. Fire performance and kinetic parameters, Macromolecular Symposia 194(1) (2003) 201-206.
[50] H.J. Ploehn, C. Liu, Quantitative Analysis of Montmorillonite Platelet Size by Atomic Force Microscopy, Industrial & Engineering Chemistry Research 45(21) (2006) 7025-7034.
[51] F. Samyn, S. Bourbigot, C. Jama, S. Bellayer, S. Nazare, R. Hull, A. Fina, A. Castrovinci, G. Camino, Characterisation of the dispersion in polymer flame retarded nanocomposites, European Polymer Journal 44(6) (2008) 1631-1641.
[52] F. Chavarria, R.K. Shah, D.L. Hunter, D.R. Paul, Effect of melt processing conditions on the morphology and properties of nylon 6 nanocomposites, Polymer Engineering & Science 47(11) (2007) 1847-1864.
[53] M. Paci, S. Filippi, P. Magagnini, Nanostructure development in nylon 6-Cloisite® 30B composites. Effects of the preparation conditions, European Polymer Journal 46(5) (2010) 838-853.
[54] J.W. Cho, D.R. Paul, Nylon 6 nanocomposites by melt compounding, Polymer 42(3) (2001) 1083-1094.

[55] J.W. Gilman, Flammability and thermal stability studies of polymer layered-silicate (clay) nanocomposites, Applied Clay Science 15(1-2) (1999) 31-49.
[56] B.N. Jang, M. Costache, C.A. Wilkie, The relationship between thermal degradation behavior of polymer and the fire retardancy of polymer/clay nanocomposites, Polymer 46(24) (2005) 10678-10687.
[57] R. Song, Z. Wang, X. Meng, B. Zhang, T. Tang, Influences of catalysis and dispersion of organically modified montmorillonite on flame retardancy of polypropylene nanocomposites, Journal of Applied Polymer Science 106(5) (2007) 3488-3494.
[58] M. Zanetti, T. Kashiwagi, L. Falqui, G. Camino, Cone Calorimeter Combustion and Gasification Studies of Polymer Layered Silicate Nanocomposites, Chemistry of Materials 14(2) (2002) 881-887.
[59] M. Lewin, Reflections on migration of clay and structural changes in nanocomposites, Polymers for Advanced Technologies 17(9-10) (2006) 758-763.
[60] J.W. Gilman, C.L. Jackson, A.B. Morgan, R. Harris, E. Manias, E.P. Giannelis, M. Wuthenow, D. Hilton, S.H. Phillips, Flammability Properties of Polymer−Layered-Silicate Nanocomposites. Polypropylene and Polystyrene Nanocomposites†, Chemistry of Materials 12(7) (2000) 1866-1873.
[61] S. Bourbigot, S. Duquesne, Fire retardant polymers: recent developments and opportunities, Journal of Materials Chemistry 17(22) (2007) 2283-2300.
[62] T. Kashiwagi, R.H. Harris, X. Zhang, R.M. Briber, B.H. Cipriano, S.R. Raghavan, W.H. Awad, J.R. Shields, Flame retardant mechanism of polyamide 6-clay nanocomposites, Polymer 45(3) (2004) 881-891.
[63] T. Kashiwagi, F. Du, K.I. Winey, K.M. Groth, J.R. Shields, S.P. Bellayer, H. Kim, J.F. Douglas, Flammability properties of polymer nanocomposites with single-walled carbon nanotubes: effects of nanotube dispersion and concentration, Polymer 46(2) (2005) 471-481.
[64] B.H. Cipiriano, T. Kashiwagi, S.R. Raghavan, Y. Yang, E.A. Grulke, K. Yamamoto, J.R. Shields, J.F. Douglas, Effects of aspect ratio of MWNT on the flammability properties of polymer nanocomposites, Polymer 48(20) (2007) 6086-6096.
[65] J.D. Lichtenhan, N.Q. Vu, J.A. Carter, J.W. Gilman, F.J. Feher, Silsesquioxane-siloxane copolymers from polyhedral silsesquioxanes, Macromolecules 26(8) (1993) 2141-2142.
[66] R. Misra, B.X. Fu, A. Plagge, S.E. Morgan, POSS-nylon 6 nanocomposites: Influence of POSS structure on surface and bulk properties, Journal of Polymer Science Part B: Polymer Physics 47(11) (2009) 1088-1102.
[67] X. Yin, H. Wu, M. Krifa, M. Londa, J. Koo, Flame retardant polyamide 6-MWNT nanocomposites: Characterization and processing via electrospinning, SAMPE TECH 2011, Fort Worth, TX, (2011).
[68] S.K. Lim, E.-P. Hong, Y.-H. Song, H. Choi, I.-J. Chin, Thermodynamic interaction and mechanical characteristics of Nylon 6 and polyhedral oligomeric silsesquioxane nanohybrids, Journal of Materials Science 47(1) (2012) 308-314.
[69] J.D. Lichtenhan, J.W. Gilman, Preceramic additives as fire retardants for plastics, US Patent US 6362279 B2, (2002).

[70] S. Bourbigot, T. Turf, S. Bellayer, S. Duquesne, Polyhedral oligomeric silsesquioxane as flame retardant for thermoplastic polyurethane, Polymer Degradation and Stability 94(8) (2009) 1230-1237.
[71] D.C.O. Marney, L.J. Russell, D.Y. Wu, T. Nguyen, D. Cramm, N. Rigopoulos, N. Wright, M. Greaves, The suitability of halloysite nanotubes as a fire retardant for nylon 6, Polymer Degradation and Stability 93(10) (2008) 1971-1978.
[72] A. Laachachi, M. Cochez, M. Ferriol, J.M. Lopez-Cuesta, E. Leroy, Influence of TiO2 and Fe2O3 fillers on the thermal properties of poly(methyl methacrylate) (PMMA), Materials Letters 59(1) (2005) 36-39.
[73] A.B. Morgan, C.A. Wilkie, Practical issues and future trends in polymer nanocomposite flammability research, John Wiley & Sons, New York, NY, USA, (2007).
[74] S.C. Lao, C. Wu, T.J. Moon, J.H. Koo, A. Morgan, L. Pilato, G. Wissler, Flame-retardant polyamide 11 and 12 nanocomposites: thermal and flammability properties, J. Compos. Mater. 43(17) (2009) 1803-1818.
[75] H. Wu, M. Krifa, J.H. Koo, Flame retardant polyamide 6/nanoclay/intumescent nanocomposite fibers through electrospinning, Textile Research Journal 84(10) (2014) 1106-1118.
[76] Y. Hu, S. Wang, Z. Ling, Y. Zhuang, Z. Chen, W. Fan, Preparation and Combustion Properties of Flame Retardant Nylon 6/Montmorillonite Nanocomposite, Macromolecular Materials and Engineering 288(3) (2003) 272-276.
[77] Y. Chen, Z. Fang, C. Yang, Y. Wang, Z. Guo, Y. Zhang, Effect of clay dispersion on the synergism between clay and intumescent flame retardants in polystyrene, Journal of Applied Polymer Science 115(2) (2010) 777-783.
[78] H. Lu, C.A. Wilkie, Study on intumescent flame retarded polystyrene composites with improved flame retardancy, Polymer degradation and stability 95(12) (2010) 2388-2395.
[79] S. Duquesne, J. Lefebvre, S. Bourbigot, R. Delobel, P. Recourt, Thermal Stability and Fire Behavior of Intumescent Systems in Presence of Layered Inorganic Fillers and Silica, Fire and Polymers IV, American Chemical Society, (2005) pp. 89-102.
[80] Y.C. Ahn, D.R. Paul, Rubber toughening of nylon 6 nanocomposites, Polymer 47(8) (2006) 2830-2838.
[81] A.J. Oshinski, H. Keskkula, D.R. Paul, The role of matrix molecular weight in rubber toughened nylon 6 blends: 1. Morphology, Polymer 37(22) (1996) 4891-4907.
[82] A.J. Oshinski, H. Keskkula, D.R. Paul, Rubber toughening of polyamides with functionalized block copolymers: 1. Nylon-6, Polymer 33(2) (1992) 268-283.
[83] O.K. Muratoglu, A.S. Argon, R.E. Cohen, M. Weinberg, Toughening mechanism of rubber-modified polyamides, Polymer 36(5) (1995) 921-930.
[84] J.J. Huang, H. Keskkula, D.R. Paul, Rubber toughening of an amorphous polyamide by functionalized SEBS copolymers: morphology and Izod impact behavior, Polymer 45(12) (2004) 4203-4215.
[85] R.J.M. Borggreve, R.J. Gaymans, J. Schuijer, J.F.I. Housz, Brittle-tough transition in nylon-rubber blends: effect of rubber concentration and particle size, Polymer 28(9) (1987) 1489-1496.

[86] A. Margolina, S. Wu, Percolation model for brittle-tough transition in nylon/rubber blends, Polymer 29(12) (1988) 2170-2173.
[87] S. Wu, A generalized criterion for rubber toughening: The critical matrix ligament thickness, Journal of Applied Polymer Science 35(2) (1988) 549-561.
[88] D.M. Laura, H. Keskkula, J.W. Barlow, D.R. Paul, Effect of rubber particle size and rubber type on the mechanical properties of glass fiber reinforced, rubber-toughened nylon 6, Polymer 44(11) (2003) 3347-3361.
[89] A. Dasari, Z.-Z. Yu, Y.-W. Mai, Effect of blending sequence on microstructure of ternary nanocomposites, Polymer 46(16) (2005) 5986-5991.
[90] I. Kelnar, J. Kotek, L. Kaprálková, B.S. Munteanu, Polyamide nanocomposites with improved toughness, Journal of Applied Polymer Science 96(2) (2005) 288-293.
[91] S.C. Tjong, S.P. Bao, Impact fracture toughness of polyamide-6/montmorillonite nanocomposites toughened with a maleated styrene/ethylene butylene/styrene elastomer, Journal of Polymer Science Part B: Polymer Physics 43(5) (2005) 585-595.
[92] C.Q. Yang, H. Yang, The Flame Retardant Nomex/Cotton and Nylon/Cotton Blend Fabrics for Protective Clothing, in: S. Vassiliadis (Ed.), Advances in Modern Woven Fabrics Technology, InTech (2011).

Chapter 2: Flame Retardant Nylon 6 Nanocomposites by Injection Molding

2.1 INTRODUCTION

Injection molded FR PA6 finds applications in electronics packing and automotive industry [1]. This chapter aims to study the *processing-structure-performance* relationship of different injection molded FR PA6 nanocomposite formulations. As discussed in the previous chapter, one of the most effective and widely used nanoparticles in the area of flame retardant applications is nanoclay. Numerous studies have demonstrated that the incorporation of nanoclay even at very low loadings could greatly suppress the peak heat release rate by creating a protective char layer during combustion [2, 3]. Although the nanoclay could effectively lower the peak HRR as characterized by cone calorimetry or microscale combustion calorimetry, the material sometimes falls short in some other flammability tests such as UL-94 [4, 5]. Therefore, a conventional intumescent flame retardant additive is also included in this system. Due to the health concerns of halogenated flame retardants, a non-halogenated flame retardant additive based on organic aluminum phosphinates is used in this study. Its flame retardant mechanism is through intumescence, whereby a protective foam is formed to isolate heat and oxygen from the combustion fuel source [6, 7].

Existing literatures and a preliminary study of our own have shown that incorporation of the FR through melt extrusion results in significant degradation in mechanical properties including tensile strength and ductility [8, 9]. Studies have shown that thermoplastic elastomers can be used as a modifier for nylons to tailor the mechanical properties [10-13]. The toughening mechanism is discussed in more detail in Chapter 1. The primary functionality sought in our nanocomposite system is flame retardancy, and there has been little work on the impact on flammability of incorporating elastomers into

thermoplastic composite systems. Thus, one of the primary question this chapter addresses is whether it is possible to successfully toughen flame retardant PA6 using blends with elastomer without compromising flame retardant performance.

There have been studies by Le Bras et al. [14, 15] showing that the incorporation of intumescent-containing PA6 into polyolefin elastomeric materials, such as ethylene–vinyl acetate (EVA), yields a better reduction of flammability than the EVA/intumescent system with no PA6 [14]. The authors explain these results by the fact that nylon plays the role of charring agent in the ternary system [14, 15]. In addition, it was suggested that the combination of EVA with PA6 suppresses the migration of FR particles during solidification of the polymer melt, which could also explain the improved flame retardant performance of the ternary blend compared to those observed with the single-polymer matrix [15].

Based on the research discussed above, it appears feasible to use rubber toughening to recover the ductility of our flame retardant PA6/intumescent composite, while at the same time preserving flame retardant performance. This chapter reports experimental results testing this hypothesis. Thus, PA6/intumescent flame retardant/thermoplastic elastomer ternary blends of various mixing ratios were evaluated for mechanical and flame retardant properties, with the objective of recovering ductility and elongation at break while reducing flammability.

Dispersion of the additives, i.e., FR, elastomers, and nanoclay, was examined by means of X-ray diffraction (XRD) and transmission electron microscopy (TEM). Crystallization behavior of the formulations were characterized by differential scanning calorimetry (DSC). Mechanical properties including tensile and Izod impact results are reported. Finally, flammability of the FR PA6 composites were evaluated by multiple test standards.

2.2 EXPERIMENTAL

2.2.1 Materials

The PA6 used in this study is medium viscosity extrusion grade nylon 6 (Aegis® H95ZI) in pellet form produced by Honeywell Inc. This type of PA6 is designed for mono and multifilament applications. The typical filament tenacities range from 5 to 8 grams per denier (gdp) [16]. A summary of some physical parameters of the PA6 is shown in Table 2.1. All the PA6 pellets are dried at 80°C for at least 24 hours prior to processing.

Table 2.1. Physical parameters of PA6 [16].

Parameter	Test method	Unit	Value
Viscosity	ASTM D-789	cP	86-98
Moisture Content	ASTM D-6869	%	Max. 0.08
Melting Point	ASTM D-3418	°C	220
Density	ASTM D-1505	g/cm^3	1.13

Intumescent flame retardant additive Exolit® OP1312 was kindly provided by Clariant International Ltd. Exolit® OP1312 is a non-halogenated flame retardant additive based on organic aluminum phosphinates. Its flame retardant mechanism is through intumescence, whereby a protective char layer is formed to isolate heat and oxygen from the combustion fuel source [6, 7, 17]. Some properties of OP1312 are listed in Table 2.2.

Table 2.2. Properties of Exolit® OP1312 flame retardant additive [18].

Property	Unit	Value
Phosphorus	% (w/w)	18.7-19.7
Moisture content	% (by wt.)	Max. 0.3
Decomposition temperature	°C	>350
Density at 20°C	g/cm^3	≈1.6

The SEBS elastomer Kraton® FG1901 G was purchased from Kraton Polymers Inc. Kraton® FG1901 G is a maleated triblock copolymer containing styrene-hydrogenated butadiene-styrene (SEBS-g-MA). Styrene-Ethylene-Butylene-Styrene (SEBS) elastomer can be used as a modifier for engineering thermoplastics, including nylons, to tailor the mechanical properties. The SEBS elastomer functionalized with maleic anhydride (Figure 2.1) forms covalent bonding with the amine groups in the nylon, creating a block copolymer which has good interfacial strength between the two phases [10]. It has been shown that SEBS-g-MA have good dispersion within PA6 even without high shear mixing [19]. The properties of FG1901 G is summarized in Table 2.3 [20].

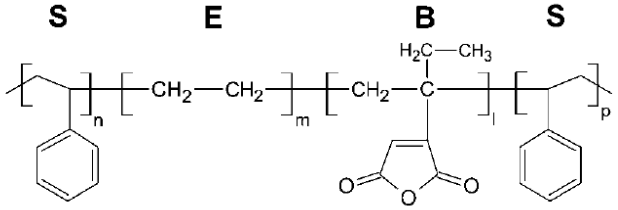

Figure 2.1. Chemical structure of maleic anhydride modified SEBS elastomer.

Table 2.3. Properties of Kraton® FG1901 elastomer [20].

Property	Test method	Unit	Value
Melt Flow, 230C/5000g	ASTM D1238	g/10min	14 to 28
Maleic Anhydride, Bound	BAM 1026	%w	1.4 to 2.0
Water	BAM 1024	ppmw	<=500
Tensile Strength	ASTM D412	Psi	5000
Specific Gravity	ASTM D792	g/cm^3	0.91
Styrene/Rubber ratio			30/70
Elongation at Break	ASTM D412	%	500
Solution Viscosity	BAM 922	Cps	5000

Montmorillonite (MMT) organoclay Cloisite® 30B was purchased from Southern Clay Products. Cloisite® 30B is produced by cation exchange and treated with 90 mequiv./100 g clay of Ethoquad T12 with methyl bis-2- hydroxyethyl tallow quaternary ammonium chloride (Figure 2.2) [10]. Table 2.3 shows a summary of some physical properties of Cloisite® 30B.

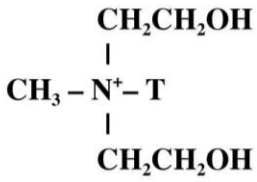

Where T is Tallow (~65% C18; ~30% C16; ~5% C14)

Figure 2.2. Surface modifier for Cloisite® 30B nanoclay [21].

Table 2.4. Physical properties of Cloisite® 30B [21].

Property	Unit	Value
Density	g/cm	1.98
Bulk Density	g/cm	0.2281-0.3638
Particle size	μm	10%≤2μm
		50%≤6μm
		90%≤13μm
Moisture Content	%	≤2%
X-Ray Diffraction d-spacing (001)	Å	18.5

2.2.2 Processing

2.2.2.1 Twin Screw Extrusion

Twin screw extrusion is used as the main processing technique throughout this study. To process larger samples following the initial screening phase, we used a Process 11 co-rotating twin-screw extruder manufactured by Thermo-Scientific Inc. (Figure 2.3). Process 11 has fully segmented screws with a diameter of 11 mm. Its large L/D ratio (L/D: 40) provides exceptional amount of shear and mixing for polymers with additives including nanoparticles. It also has 8 heating zones which can be controlled individually by the computer. The throughput rate can be adjusted from 20 g/hr to 2.5 kg/hr. To ensure a homogenous dispersion prior to melt compounding, formulations with varying concentrations were pre-mixed using the Thinky® Planetary Mixer (Figure 2.4). Water cooled continuous filament was obtained by using a 3mm diameter die with barrel temperature of 240°C and screw speed of 150 rpm. The feeding rate of neat PA6 was set to 220 g/hr. A pelletizer was used to cut the filament into pellets in preparation for the injection molding process.

Figure 2.3. Process 11 Parallel (co-rotating) Twin Screw Extruder (picture from Thermo Scientific website).

Figure 2.4. Thinky® Planetary Mixer and its working principle.

2.2.2.2 Injection Molding

Extruded materials from Process 11 were injection-molded into ASTM D638 standard tensile bars, using a Mini-Jector injection molding system (Figure 2.5) with barrel temperature at 270°C and mold temperature at 60°C. All pellets were dried at 80°C for at least 8 hours before injection molding.

Figure 2.5. Haake Minijet (left) and Mini Jector (right) injection molding machine.

2.2.3 Formulations

Table 2.5 shows the formulations were tested with the goal of developing non-drip flame retardant PA6 fibers. A study was first performed to examine the effect of FR performances between nanoclay and intumescent flame retardants. PA6 incorporated with intumescent FR and nanoclay achieved high performance in terms of flame retardancy. However, it suffered from significant loss in certain mechanical properties, especially elongation at break. This loss in ductility imposes a challenge for applications, such as fiber spinning where material ductility is a critical issue. In order to recover the lost elongation at break, various amounts of thermoplastic elastomer were compounded with flame retardant and PA6 (sample 1-6). The second step was performed to formulate rubber toughened FR nanocomposite by lowering the FR concentration and adding nanoclay to the materials matrix (sample 7-13). The elastomer concentrations were selected based on the results from sample 1-6. The nanoclay loading was based on extensive publications on

FR PA6 nanocomposites [2, 22]. In the following discussion, the label for each formulation is composed of three number, the first number indicates the weight concentration of the FR, the second number indicate the elastomer loading, and the last one indicates the nanoclay loading. For example, 15_10_2.5 means there are 15 wt% FR, 10 wt% elastomer and 2.5 wt% nanoclay in the PA6.

Table 2.5. FR PA6 formulations for injection molding.

Sample ID	**Label**	**PA6 (wt%)**	**Flame retardant (wt%)**	**Elastomer (wt%)**	**Nanoclay (wt%)**	**Category**
1	Neat	100	0	0	0	Effect of
2	20FR	80	20	0	0	rubber
3	20_5	75	20	5	0	toughening
4	20_10	70	20	10	0	of FR PA6
5	20_15	65	20	15	0	
6	20_20	60	20	20	0	
7	Neat	100	0	0	0	Study of
8	15_5_2.5	77.5	15	5	2.5	rubber
9	15_5_5	75	15	5	5	toughening
10	15_10_2.5	72.5	15	10	2.5	effect of FR
11	15_10_5	70	15	10	5	PNC
12	15_15_2.5	67.5	15	15	2.5	
13	15_15_5	65	15	15	5	

2.2.4 Characterization Techniques

2.2.4.1 Scanning Electron Microscopy (SEM)

High resolution SEM characterization of fiber morphology and char morphology was carried out using a Hitachi S-5500 STEM equipped with Energy-dispersive X-ray spectroscopy (EDS) detector. Char residues from MCC tests were transferred to the SEM sample holder and directly put into the sample chamber without coating. The accelerating voltage for imaging was 5 kV and in order to get a better signal to noise ratio, 30 kV was used for EDS. Bruker ESPRIT software was used for image acquisition and data analysis.

2.2.4.2 Transmission Electron Microscopy (TEM)

The elastomer toughened FR system and nanoclay dispersion were characterized by TEM. Ultrathin sections of the extruded composite samples were obtained by cryogenic microtoming using a Leica Ultramicrotome with a diamond knife at -110°C. The sections were then placed on 400 mesh copper grids. The grids were transferred into an FEI Tecnai Transmission Electron Microscope (TEM) setting accelerating voltage at 80 kV for phase contrast imaging. TEM images of samples under two different conditions were taken. To observe the nanoclay and flame retardant particles, sample sections were directly put into TEM for observation. In order to resolve the elastomer/nylon interface, samples were stained with 2% phosphotungstic acid (PTA) for 30min to let the WO_3 penetrate into the amorphous phase of nylon. Stained samples were rinsed with water and dried before imaging.

2.2.4.3 X-ray Diffraction (XRD)

Wide-angle X-ray diffraction (WAXD) was carried out on both injection molded samples and melt-spun fibers using a Rigaku R-Axis Spider with curved image plate (Cu Kα radiation). A small piece (~1 mm) of the injection molded samples were cut from the

surface and directly placed on the sample holder with mineral oil. All samples were set to rotate at 10°/sec during scanning with 10min.

2.2.4.4 Differential Scanning Calorimetry (DSC)

DSC was carried out using a Q20 from TA Instruments. For the DSC tests, injection molded samples were cut into 7-8 mg square pieces were directly put into the crucible for testing. To erase the thermal history, all samples were first heated from room temperature to 260°C at 10°C/min; after holding at 240°C for 2 min, the samples were cooled down to room temperature at -10°C/min. A second heating cycle then started at the same rate to the maximum of 260°C. The nitrogen flow rate was held constant at 50 ml/min at all time. To calculate the percent of crystallinity, the heat of fusion ΔH_f for pure crystalline of 240 J/g was used. The ΔH_f values for each sample are based on the amount of pure PA6 within the formulation.

2.2.4.5 Flammability Tests

Thermal combustion properties of the FR PA6 formulations were measured using a Micro-scale Combustion Calorimeter (MCC), UL-94 vertical tests and LOI. For the MCC test, a model MCC-2 by Govmark Organization Inc. (Figure 2.6) was used according to ASTM D7309-2007. Before each test, all specimens are measured between 2-5 mg. The combustor temperature was held constant at 900°C, and the samples were heated in the pyrolyzer from 100°C to 750°C at 1°C/sec. The flow rate of nitrogen and oxygen were 80 ml/min and 20 ml/min, respectively. Each formulation was tested 5 times to calculate average and error bars.

Figure 2.6. Micro-Combustion Calorimeter (model MCC-2 by The Govmark Organization Inc.).

For vertical UL-94 test, samples were injection molded into 125 mm × 13 mm × 3 mm specimens as stipulated in the standard method. Before each test, the specimen was held in the vertical position from one end as a burner flame was applied at its free end for two 10-second intervals.

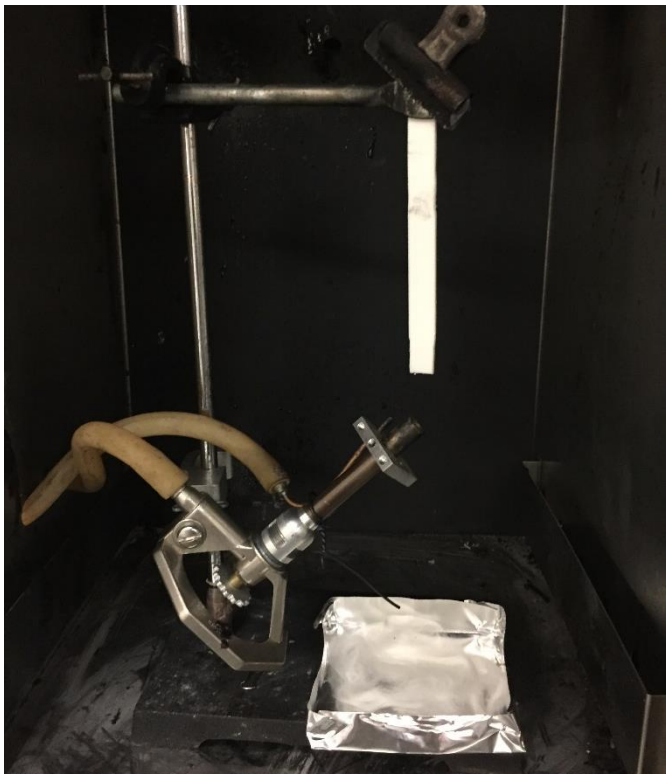

Figure 2.7. UL-94 vertical burning test set-up.

LOI tests were carried out using a lab made LOI apparatus in accordance with ASTM D2836 (Figure 2.8). Two digital flow meters controls the flow rate of oxygen and nitrogen as they are mixed in the glass tube. Samples were ignited with a lighter and the burning time was recorded.

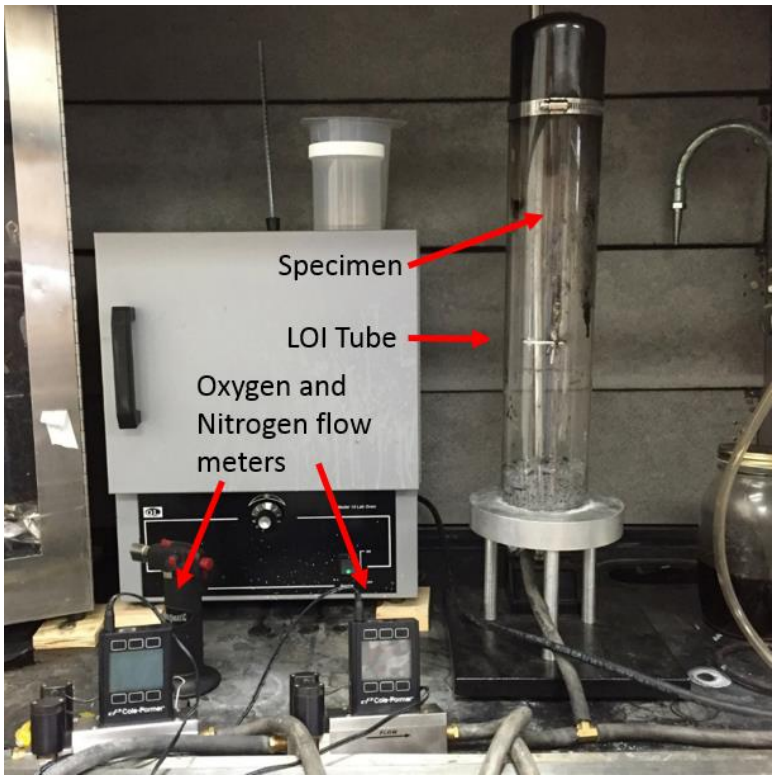

Figure 2.8. Picture of the LOI apparatus.

2.2.4.6 Tensile Test

Tensile tests were carried out in accordance to ASTM D638 using an Instron 5966. Samples were injection molded into type I specimens with overall length of 165 mm and 3.2 mm in thickness. The crosshead speed was 5 mm/min with gauge length of 50 mm. The distance between grips was 115 mm. Average values and error bars were calculated based on 3 testes on each formulation.

2.2.4.7 Izod Impact Test

Izod impact strength of selected samples was tested using a Shanta Engineering Izod/Charpy Impact Tester (India) in accordance with ASTM D256. The dimension of the test coupon was 100 mm×10 mm×4 mm and a 2.5 mm deep notch was cut on each

specimen. Five specimens were tested for each formulation. All Izod impact specimens were conditioned at 21°C and 50% RH for at least 48 hours before testing.

2.3 RESULTS AND DISCUSSION

2.3.1 X-Ray Diffraction (XRD)

XRD patterns of neat PA6, sonicated FR and injection molded PA6 with 20 wt% FR are shown in Figure 2.9. The 2θ peaks at 10.9° and 21.3° correspond to (020) and (002) planes of the γ phase crystal of PA6 [23]. This indicates that the injection molding process favored the formation of the less stable γ crystals due to slow cooling in the mold [24]. On the other hand, the distinct peaks of FR additives at 9.1°, 14.7°, 18.6°, and 26.3° suggest that FR crystals are mixed within the PA6 without changing its crystalline structure.

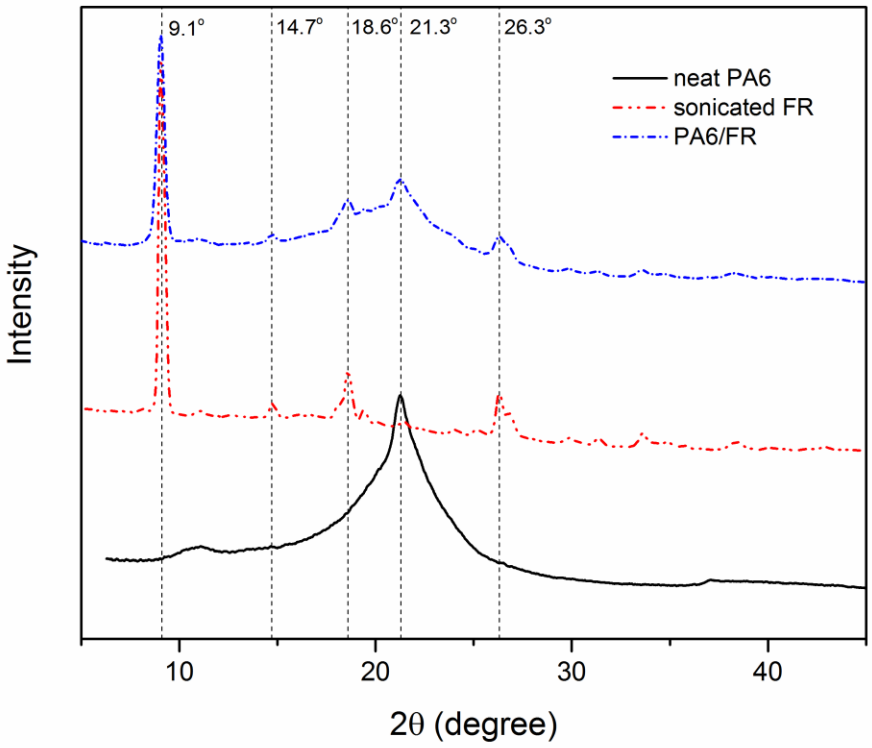

Figure 2.9. XRD patterns of neat PA6, sonicated FR and injection molded PA6 with 20 wt% FR.

To examine the effect of elastomers on the crystalline structures of PA6/FR/elastomer blends, XRD were performed on neat elastomer pellets and PA6 compounded with 20 wt% FR and various amount of elastomer, i.e. 5 wt%, 10 wt%, and 20 wt%. As shown in Figure 2.10, the diffraction pattern of neat elastomer has a very broad peak around 19.1°. The broad peak suggest that the SEBS elastomer used in this study is mostly amorphous if any crystalline structure of polyethylene exists in the block copolymer. Because of the amorphous nature, the variation of elastomer loading does not have significant influence on XRD results of the polymer blend.

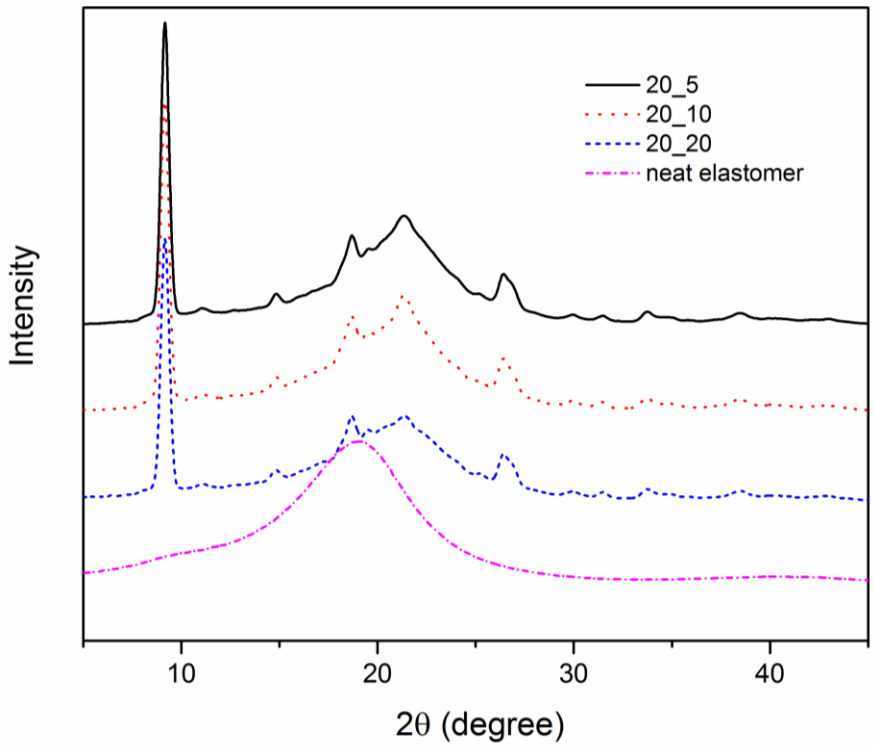

Figure 2.10. XRD patterns of neat elastomer and PA6/FR/elastomer blends containing 20 wt% FR and various amount of elastomers (5 wt%, 10 wt%, and 20 wt%).

Figure 2.11 depicts XRD patterns of neat nanoclay powders and a FR PA6 formulation containing 5 wt% nanoclay. Neat nanoclay powder exhibits distinct basal reflections of the stacked clay structure with 2θ peaks at 4.8°, 19.7°, and 35.2° corresponding to interlayer d-spacing of 18.7 Å, 4.6 Å, and 2.6 Å respectively. Since the intensity of the lower angle peak at 4.8° is significantly higher than the other two, it is considered as the main crystalline d-spacing of the Cloisite® 30B nanoclay used in this study. After twin screw extrusion, the reflection peaks of nanoclay disappeared for all nanoclay formulations as shown in Figure 2.11. The disappearance of nanoclay reflection peaks suggest that high level exfoliation of nanoclay platelets was achieved. This observation is further confirmed by TEM results which will be discussed in the following

section. Moreover, it is noted that the incorporation of nanoclay had no influence on the crystalline structure of the PA6: γ-form crystal is still the dominant crystal structure as characterized by its 2θ peak at 21.3°.

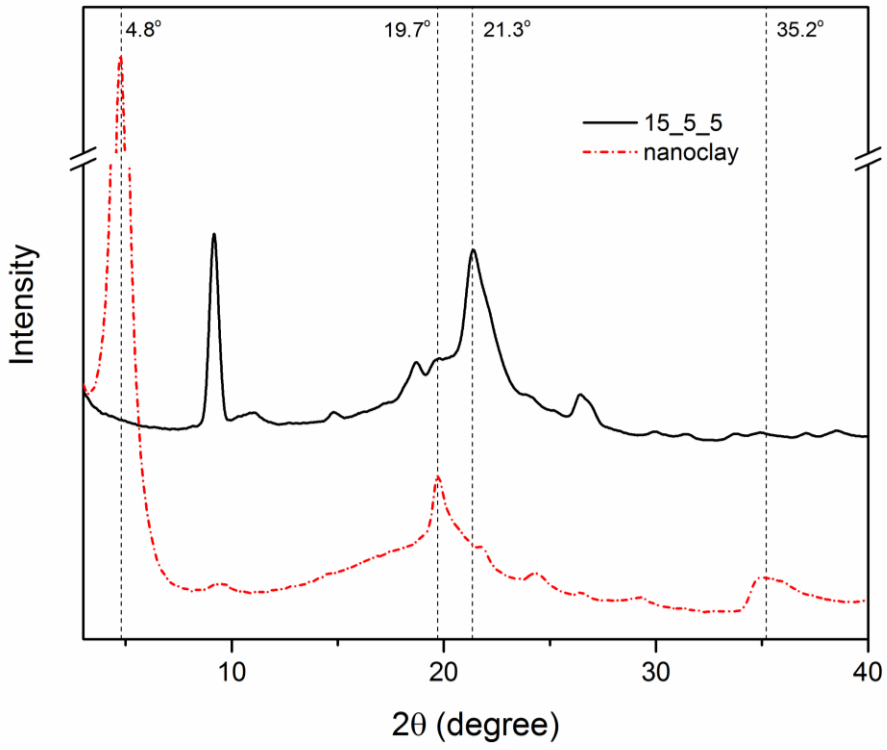

Figure 2.11. XRD patterns of neat nanoclay powders and PA6/FR/elastomer/nanoclay blend containing 15 wt% FR, 5 wt% elastomer, and 5 wt% nanoclay.

2.3.2 Transmission Electron Microscopy (TEM)

The processing method is an important factor that dictates the dispersion of additives within polymer matrix. TEM is a highly effective tool to evaluate the quality of the additive dispersion. To examine the state of additive dispersion, TEM images were taken on selected samples that contains the components used in this study: FR, elastomer, and nanoclay. The results will be representative of all other formulations since the same processing conditions were used.

Figure 2.13 shows TEM micrographs of PA6/FR/Elastomer blend. The irregularly shaped large dark particles shown in the Figure 2.12 are flame retardant particles with various sizes ranging from hundreds of nanometers to microns. From the TEM micrographs, the overall distribution of the flame retardants appeared to be uniform throughout the PA6.

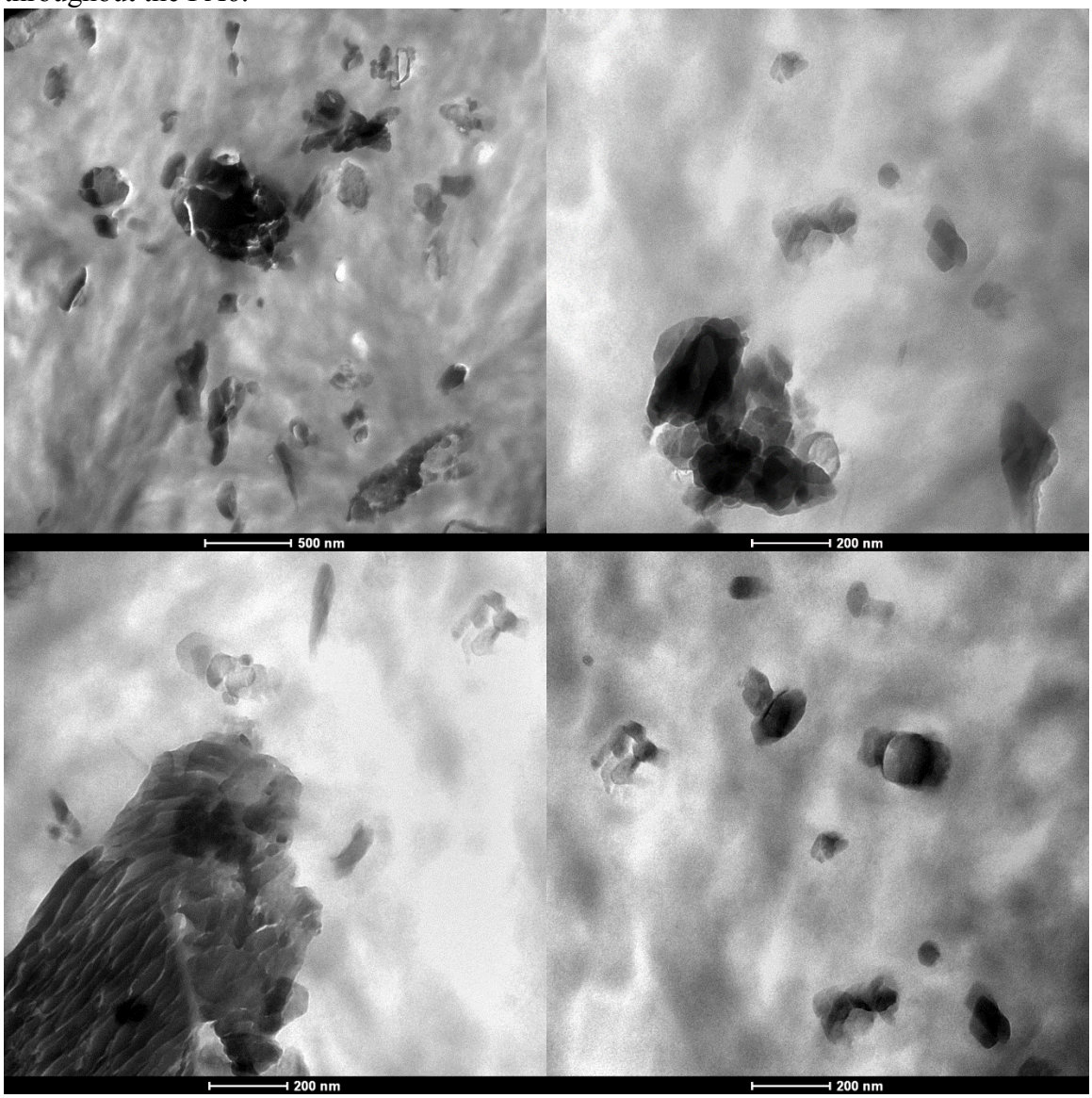

Figure 2.12. TEM micrographs showing large FR particles of injection molded PA6 with 20 wt% flame retardant and 15 wt% elastomer (unstained).

TEM is also a powerful tool to characterize the morphology of polymer blends both qualitatively and quantitatively. Because most polymer blends are organic materials in both phases, similar electron density make it difficult for TEM to generate enough contrast between the two phases. To obtain enhanced contrast, one commonly used method is staining which involves the incorporation of electron dense element into a specific polymer phase [25]. In this study, phosphotungstic acid (PTA) was used to stain the nylon phase. Figure 2.13 shows TEM micrographs of PTA stained samples. The spheres of elastomers with diameters around 50 to 100 nm appear well dispersed in the PA6 matrix. The sub-micron sized large bright spots represent the sites where the flame retardant particles were located before they were washed off the cross-section surface during staining. Because PTA only stained the amorphous regions of the PA6, the dark areas in Figure 2.13 are amorphous regions of PA6 and the lines shown in the higher magnification image are the crystalline lamellae. The crystalline lamellae appear packed preferentially along the nylon/elastomer interface forming stacked layers around the elastomer particles. This observation is consistent with previous publications [11, 13, 26].

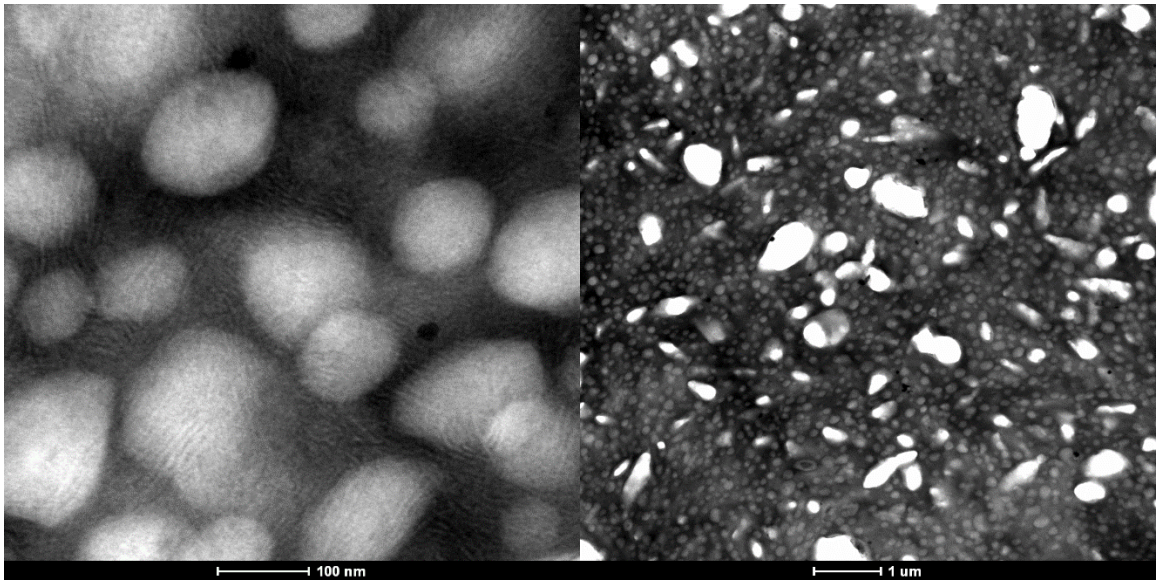

Figure 2.13. TEM micrographs showing elastomer dispersion of injection molded PA6 with 20 wt% flame retardant and 15 wt% elastomer (stained with PTA).

Figure 2.14 shows high magnification TEM images of sample #11 containing 15 wt% flame retardant, 10 wt% elastomer, and 5 wt% nanoclay. Although some intercalated nanoclay platelets exist within the sample, most nanoclays appear exfoliated and uniformly dispersed in the polymer matrix.

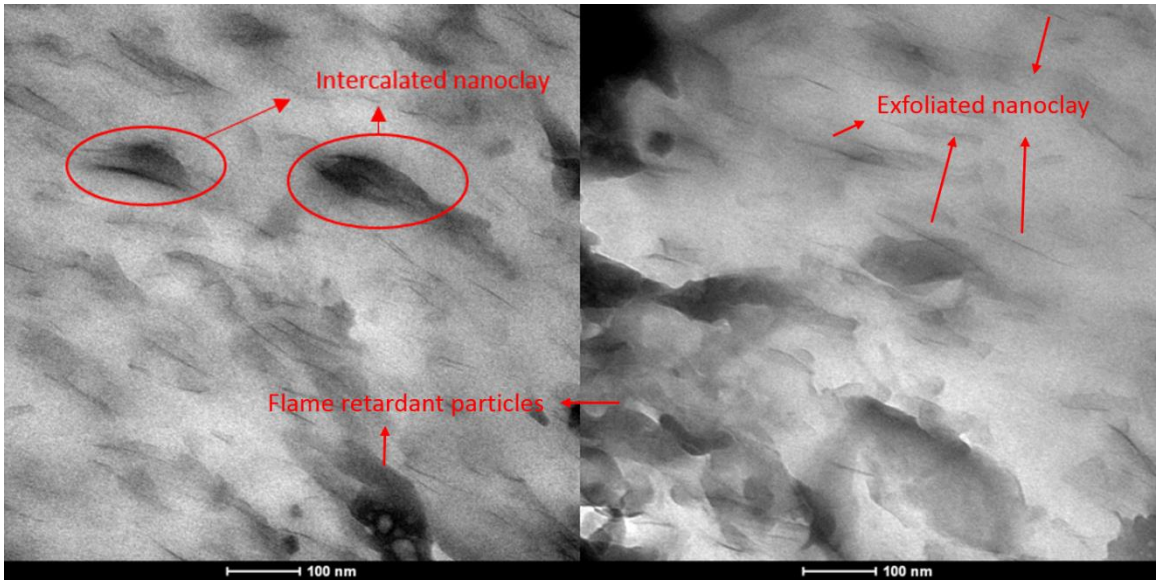

Figure 2.14. TEM micrographs showing nanoclay dispersion within injection molded PA6 nanocomposites containing 15 wt% flame retardant, 10 wt% elastomer, and 5 wt% nanoclay (unstained).

2.3.3 Differential Scanning Calorimetry (DSC)

Figure 2.15 shows the DSC first heating endotherms of samples taken from injection molded neat PA6 and five different FR formulations. The melting peak temperature (T_m) and percent of crystallinity calculated from the heating scans are summarized in Table 2.6. The endotherms from the first heating allows for examination of the impact of different components in the FR formulation on the crystallization behavior of the PA6 matrix. Neat PA6 has two distinct endothermic peaks at 220.1°C and 225.1°C which correspond to the melting of γ crystalline and α crystalline, respectively. The small sloped shoulder before the melting peaks may be caused by the presence of γ crystals. Note that only γ crystals are detected from XRD results, this may be caused by the nature of the core-skin structure of the injection molded materials [27]. The skin part undergoes faster cooling and higher stress; therefore, γ crystal is dominant. The core experiences slower cooling and less stress; as a result, a fair amount of α crystal is formed [27]. From the

heating scans, neat PA6 have relatively low crystallinity which could be due to the lack of nucleus or fast cooling during the injection molding process. Adding 20 wt% of FR to the neat polymer diminished the separation of the two crystal melting peaks leaving only one major peak at 223.1°C, which corresponds to the melting of α crystal. The lower melting peaks may also be attributed to the decreased crystallite thickness of PA6 [27]. Elastomers seem to have no influence on the crystallization behavior of PA6 as no significant difference is observed in the exotherms. On the other hand, formulations containing nanoclay show a notable lower temperature peak corresponding to the γ crystal.

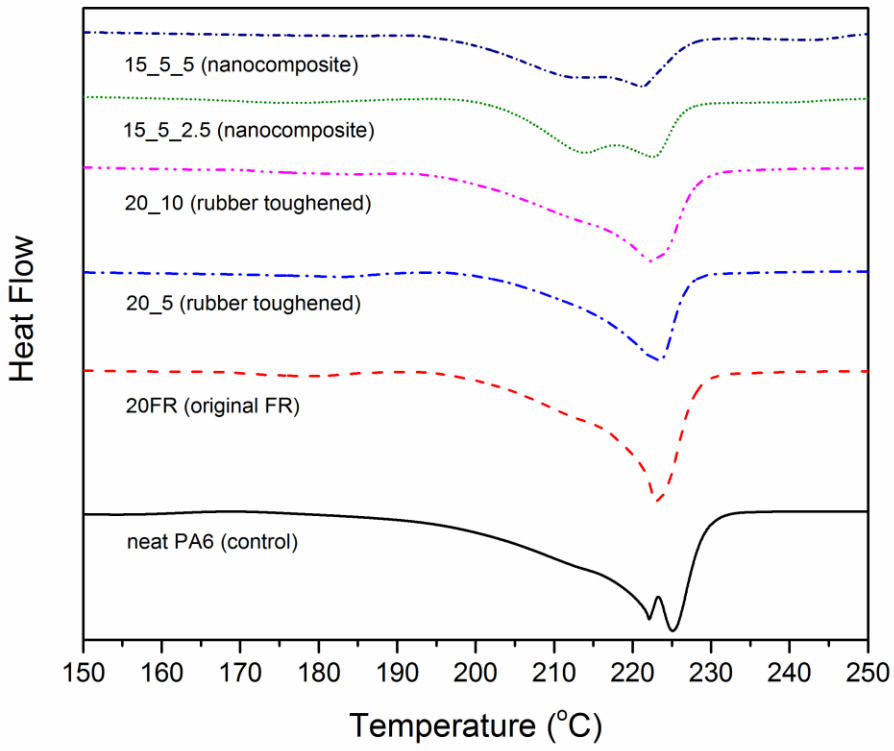

Figure 2.15. First DSC heating scans of different injection molded FR PA6 formulations (exotherms up). Samples were heated at 10°C/min. Scans are shifted for clarity.

Figure 2.16 compares the cooling scans for the same set of samples and Table 2.6 summarizes the peak crystallization temperature denoted as T_c. Unlike the heating scans, all cooling scans have only one exothermic peak. The neat PA6 has a crystallization peak at 182.7°C which is slightly lower than its FR formulations. Under controlled cooling rate of 10°C/min, all formulations yielded lower crystallinity than the neat PA6. 20FR increased the crystallization temperature to 185°C which suggest that the FR particles could lower the free energy barrier for crystallization by facilitating the heterogeneous nucleation within PA6. Samples containing elastomer have slightly lower crystallization temperature around 183.9°C this could be due to the finely dispersed elastomer phases hindering the chain mobility of PA6 which result in slower crystallization process. Adding nanoclay to the blend lead to small increase in crystallization temperature as compared to the PA6/FR/elastomer blend. This may be because of the well-known nucleation effect for PA6/clay nanocomposites [27, 28]. Higher clay loadings lead to lower crystallinity in both heating and cooling scans, this is explained by restrained space for crystalline growth caused by dispersed clay platelets.

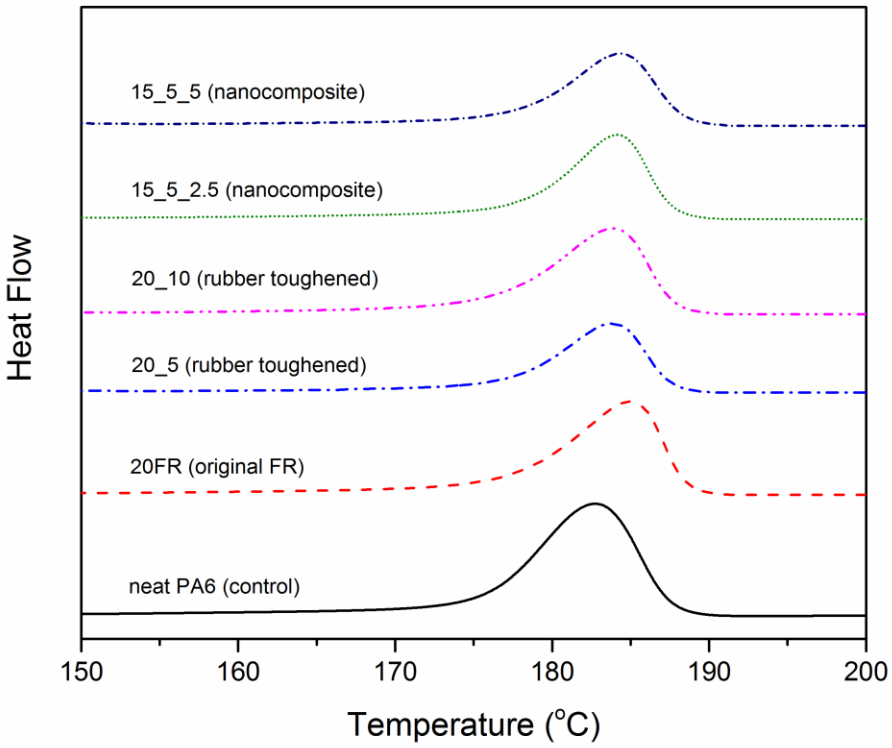

Figure 2.16. First DSC cooling scans of different injection molded FR PA6 formulations (exotherms up). Samples were cooled at 10°C/min. Scans are shifted for clarity.

Table 2.6. Summary of percent of DSC data for different injection molded FR PA6 formulations. ($X_{c,1}$ is the percent crystallinity calculated by inegration of the first heating peak, $X_{c,2}$ is the percent crystallinity calculated by integration of the first cooling peak).

Sample	T_m(°C)	T_c(°C)	$X_{c,1}^*$(%)	$X_{c,2}^*$(%)
neat PA6	222.1/225.1	182.7	21.8	25.1
20FR	223.1	185.0	24	24.1
20_5	223.0	183.8	22.8	24.2
20_10	222.2	183.9	24.1	23
15_5_2.5	213.1/222.6	184.2	21.3	24.5
15_5_5	211.4/221.2	184.3	20.8	23.5

2.3.4 Tensile Properties

A typical stress strain curve for the injection molded PA6 and its FR-clay nanocomposite is shown in Figure 2.17. With 20 wt% FR additives and 5 wt% clay loading, the tensile strength of the nanocomposite sample decreased by 23% while Young's modulus increased by 45% (Table 2.7). An increase in Young's modulus of PA6 with the addition of various nanoclay additives has been observed in the literature and was explained by the good interfacial properties between nanoclay and PA6 [27]. Usuki et al. [29] found that the negative charge on the montmorillonite layer interacted strongly with the ammonium end group on PA6. This ionic interaction could explain why the nanocomposite materials had higher stiffness, i.e. higher modulus.

The stress-strain curves in Figure 2.17 depict a major change in behavior of the FR nanocomposite system from ductile to brittle. The main disadvantage of this nanocomposite formulation is its significant reduction in elongation at break. From the stress strain curve in Figure 2.17, it is obvious that composite samples breaks at a substantially lower strain than the neat PA6. The same phenomenon has also been reported for nylon 11 with similar FR additive compositions [30]. Loss of ductility and impact resistance has also been widely reported with a numerous other hybrid materials ranging of glass-fiber-reinforced composites [19] to organoclay/PA6 nanocomposites [31-33].

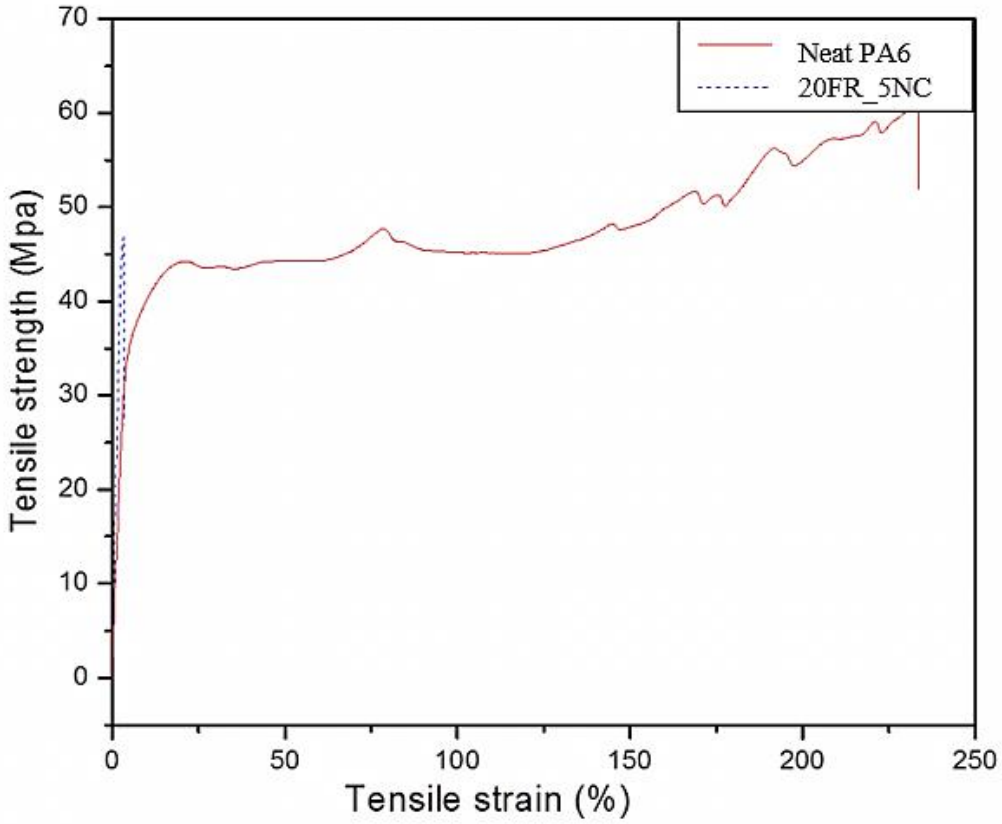

Figure 2.17. Comparison of typical stress-strain curve of injection molded neat PA6 and its FR nanocomposite.

Table 2.7. Tensile properties neat PA6 and its FR nanocomposite.

Formulation	Tensile Strength (MPa)	Young's Modulus (MPa)	Elongation at break (%)
Neat PA6	59.3±1.3	1436±32.2	230±14.8
20FR_5NC	45.4±0.5	2685±46.1	3.1±0.1

To improve the elongation break of the original FR PA6 formulation, Styrene-Ethylene-Butadiene-Styrene (SEBS), a type of elastic thermoplastic block copolymer, was added to the mixture while maintaining the flame retardant loading at 20 wt%.

Table 2.8 summarizes the room temperature mechanical properties of PA6 blends containing elastomer and flame retardant additives. In agreement with previous studies [34], all composite samples containing only flame retardant have lower ultimate tensile strength than the neat system. After adding 5 wt% elastomer, the tensile strength decreases even further. At 15 wt% elastomer loading the tensile strength dropped significantly to 30.2 MPa, further increase in elastomer concentration does not affect the strength by much, as can be seen from Figure 2.18.

It is known from our previous studies that the main impact of the flame retardants on mechanical properties lies in the elongation at break, which could degrade by more than 90% [34]. In this study, the addition of 20 wt% of flame retardant to the PA6 drops the elongation at break from 205% to 4.3%, a more than 97% decease (Figure 2.19). Samples with low concentrations of elastomer only slightly brought back the elongation at break. The elastomers start showing sizeable recovery of elongation at break when 10 wt% or more is added to the system. Samples containing 20 wt% flame retardant and 20 wt% elastomer exhibited a recovered elongation value of 68.8%.

Overall, the combined effects above show a positive influence in terms of Young's modulus with the addition of flame retardant. A 37% improvement in Young's modulus was observed in the 20FR formulation which was associated with a significantly stiffer and more brittle behavior than neat nylon (Figure 2.20). Because of the relatively low modulus of the elastomers, all samples containing elastomers have decreased modulus as expected. It is noted that samples with 20 wt% flame retardant and 10wt% elastomers have higher modulus than the one with 5 wt% elastomer. Thus, the mechanical behavior of the composite system can be tailored by varying the concentration of elastomers in the ternary blend.

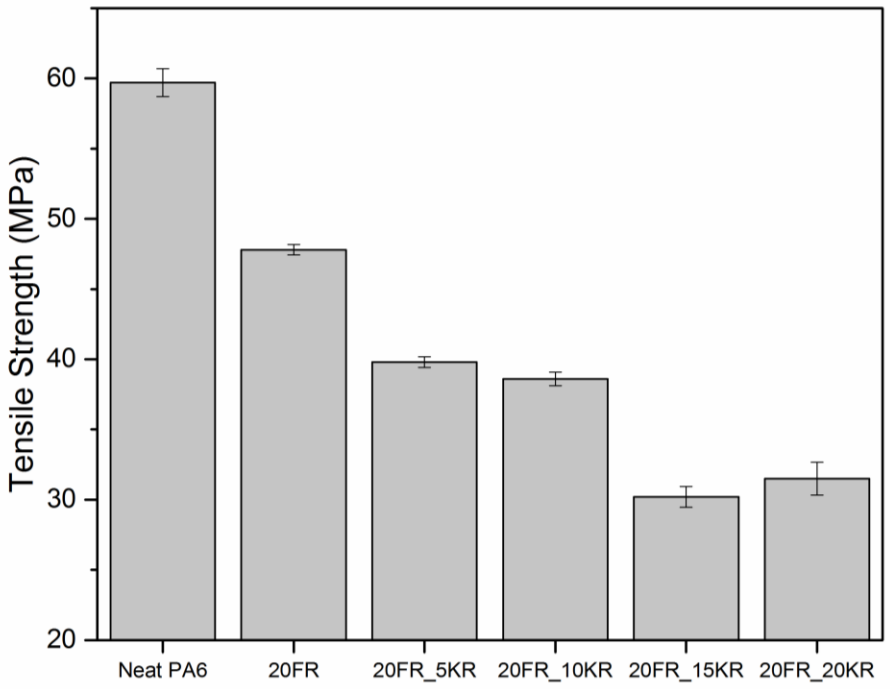

Figure 2.18. Tensile strength of flame retardant PA6/elastomer blends.

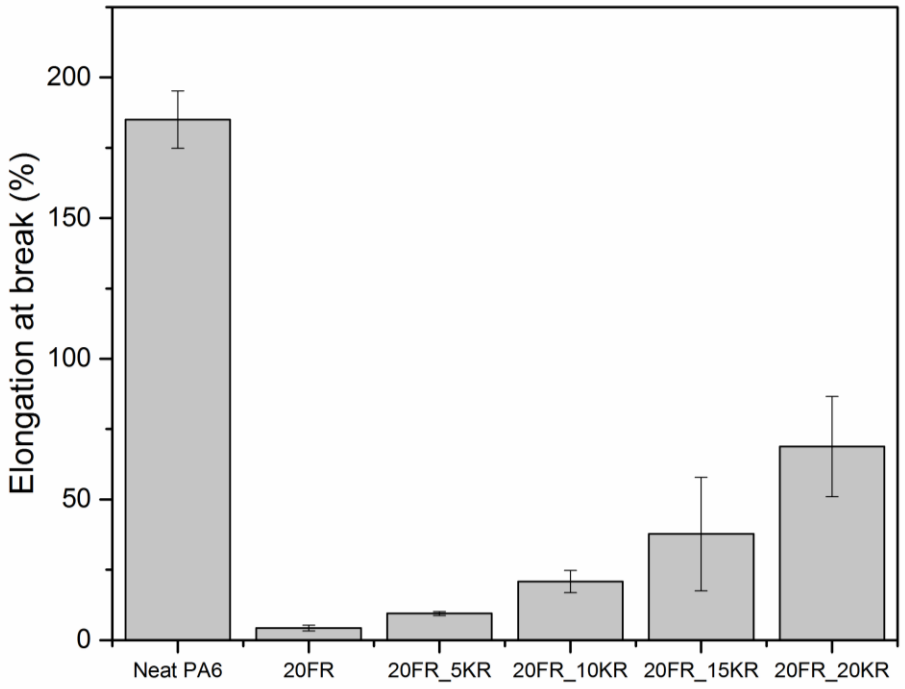

Figure 2.19. Elongation at break of flame retardant PA6/elastomer blends.

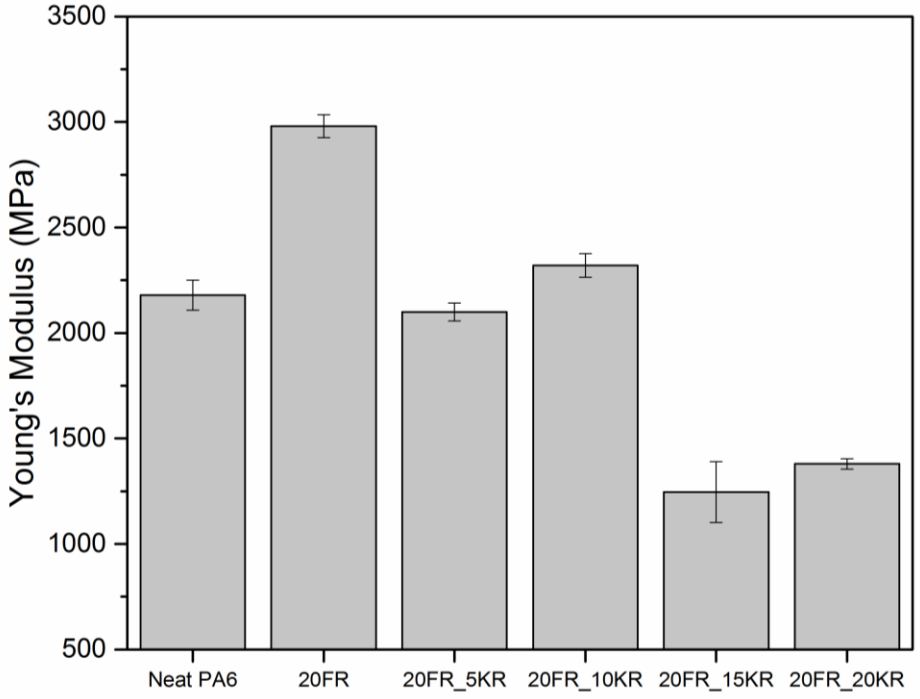

Figure 2.20. Young's modulus of flame retardant PA6/elastomer blends.

Table 2.8. Tensile properties of rubber toughened FR PA6 composites.

	Tensile strength (MPa)	**Modulus (MPa)**	**Elongation at break (%)**
Neat PA6	58.7±0.5	2175±71.1	205.4±12.6
20FR	47.8±0.3	2980±46	4.3±0.9
20FR_5KR	39.8±0.8	2100±42.2	9.5±0.7
20FR_10KR	38.6±0.5	2320±56.3	20.8±3.9
20FR_15KR	30.2±0.7	1246±143.9	37.8±20.2
20FR_20KR	31.5±1.2	1380±24.4	68.8±17.8

Table 2.9 summarizes the mechanical properties of neat PA6 and all formulations containing flame retardant, elastomer and nanoclay. Neat PA6 has tensile strength and Young's modulus of 58.7 and 2175 MPa, respectively. Note that the different values of neat PA6 and 20FR in Table 2.8 and Table 2.9 comes from the difference in specimen geometry (i.e. thickness, width) and test conditions (i.e. gauge length, pulling speed etc.).

Comparing formulations with same amount of FR and elastomer, higher nanoclay loadings will generally yield higher tensile strength and modulus except for the 15FR_15KR_2.5NC and 15FR_15KR_5NC, where the higher nanoclay content results in lower tensile strength (Figure 2.21). On the other hand, it is obvious that elastomers have positive influence on the elongation at break (Figure 2.23) while the opposite is true for nanoclay. With the 15 wt% elastomer loading, sample 15FR_15KR_2.5NC have the highest elongation at break of 76%.

Table 2.9. Tensile properties of FR PA6 nanocomposite formulations.

Formulation	**Tensile strength (MPa)**	**Young's Modulus (MPa)**	**Elongation at break (%)**
Neat PA6	58.7±0.5	2175±71.1	205.4±12.6
20FR	47.8±0.3	2980±46	4.3±0.9
15FR_5KR_2.5NC	45.1±0.5	2420±40	16.9±1.0
15FR_5KR_5NC	48.3±0.5	2730±29	6.8±0.7
15FR_10KR_2.5NC	41.0±0.3	2190±29	27.6±3.7
15FR_10KR_5NC	42.7±0.2	2450±25	12.0±0.6
15FR_15KR_2.5NC	39.8±0.6	1770±65	76.0±2.7
15FR_15KR_5NC	37.9±0.3	2012±22	20.7±1.9

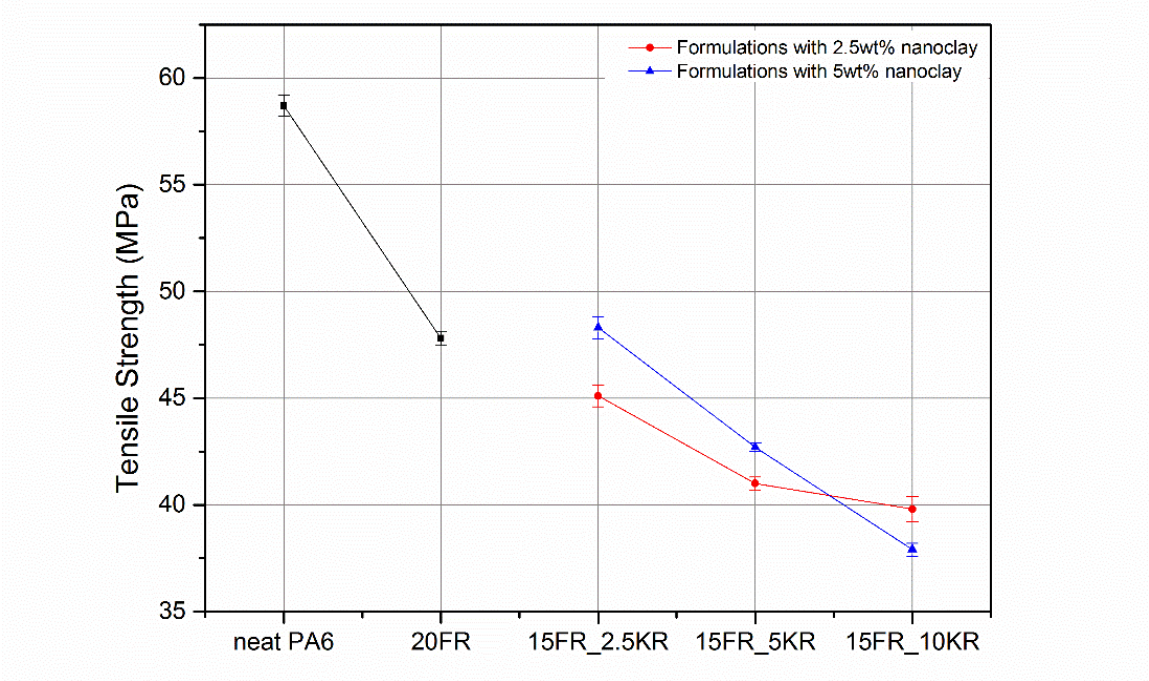

Figure 2.21. Tensile strength of FR PA6 nanocomposite formulations.

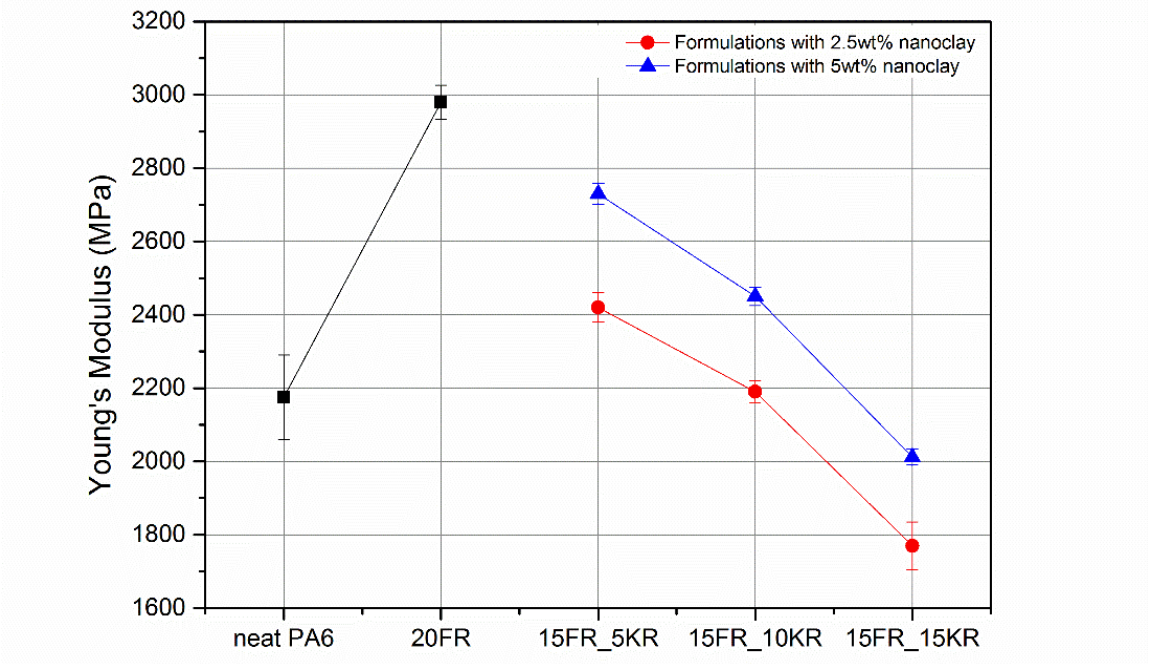

Figure 2.22. Young's modulus of FR PA6 nanocomposite formulations.

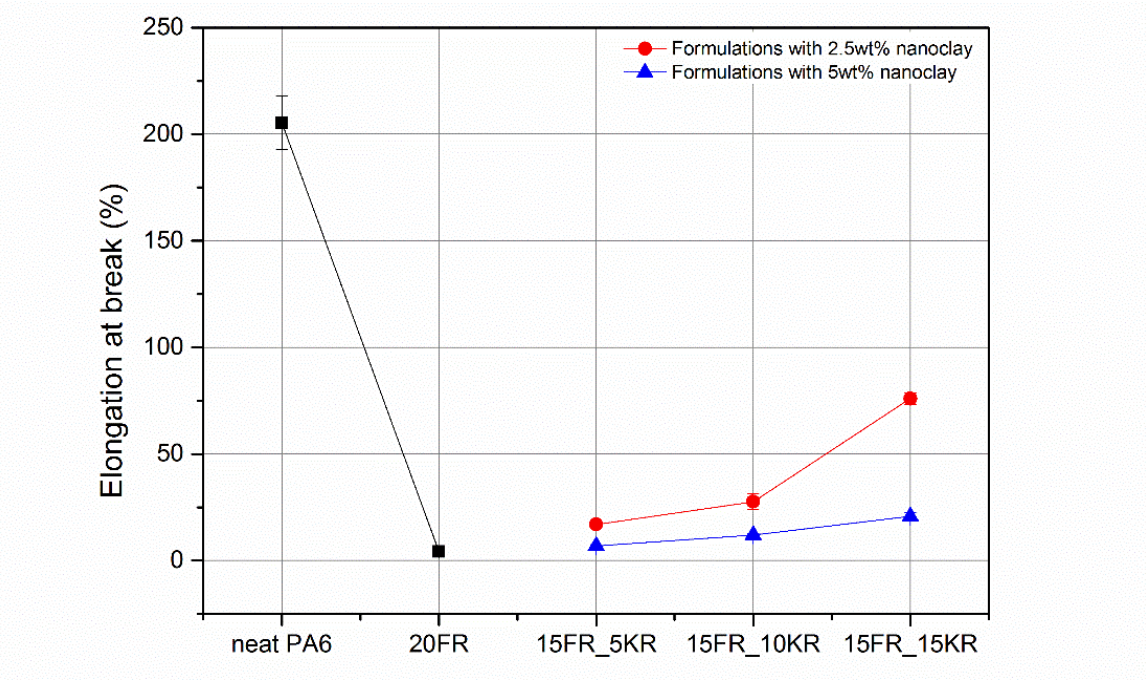

Figure 2.23. Elongation at break of FR PA6 nanocomposite formulations.

2.3.5 Izod Impact Strength

Izod impact strength measures toughness of samples with varying FR and elastomer concentrations shown in Figure 2.24. The impact strength of neat PA6 is 11.4 kJ/m^2. After adding 20 wt% of FR particles the impact strength decreased over 20% to 8.8 kJ/m^2. This loss in impact strength is consistent with the loss in elongation at break and can be explained by the presence of large FR agglomerates observed in TEM (Figure 2.12).

Such loss in toughness can be restored by addition of elastomers as seen in Figure 2.24. The sample with 20 wt% flame retardant and 5 wt% Kraton elastomer has impact strength of 10.6 kJ/cm^2, a 20% increase compared to the sample with only flame retardant. PA6 with 20 wt% FR and 10 wt% KR brings the impact strength back to 11.56 kJ/m^2 which is slightly higher than neat PA6. At 20 wt% elastomer loading, the impact strength reaches 15.4 kJ/cm^2. This is 35% higher than the neat PA6 and 75% higher than the formulation

with just flame retardant. This indicates that the SEBS elastomer could effectively toughen the original PA6/FR system.

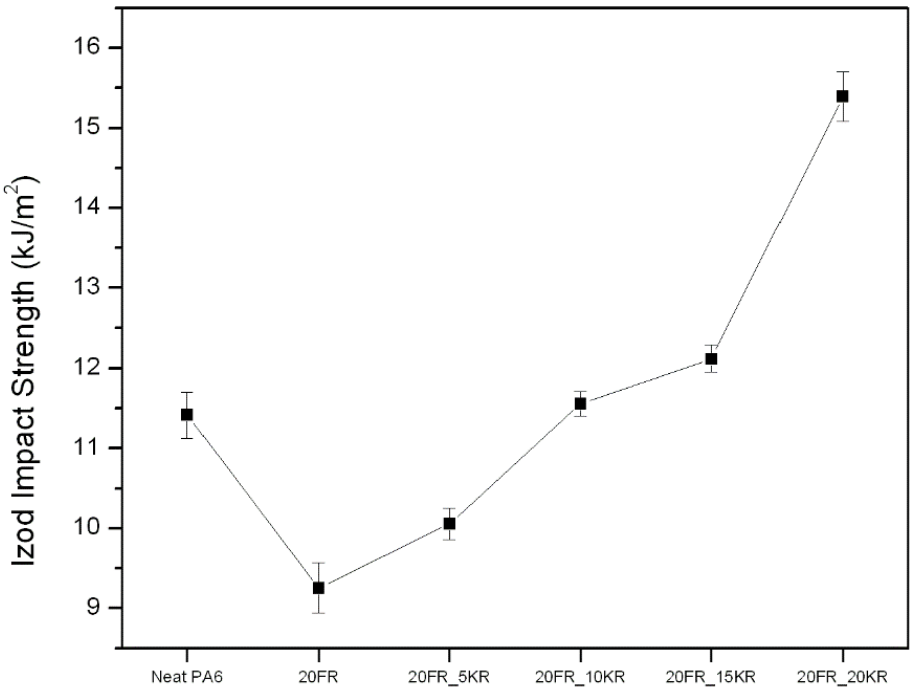

Figure 2.24. Comparison of Izod impact strengths of the rubber toughened FR PA6.

Izod impact strengths of neat polyamide 6 and its nanocomposites are compared in Figure 2.25 to evaluate the impact of nanoclay on the results above. On the other hand, it is not surprising to find that higher nanoclay loadings tend to have lower impact strength [10] except for nanocomposite samples containing 15 wt% FR and 10 wt% elastomer.

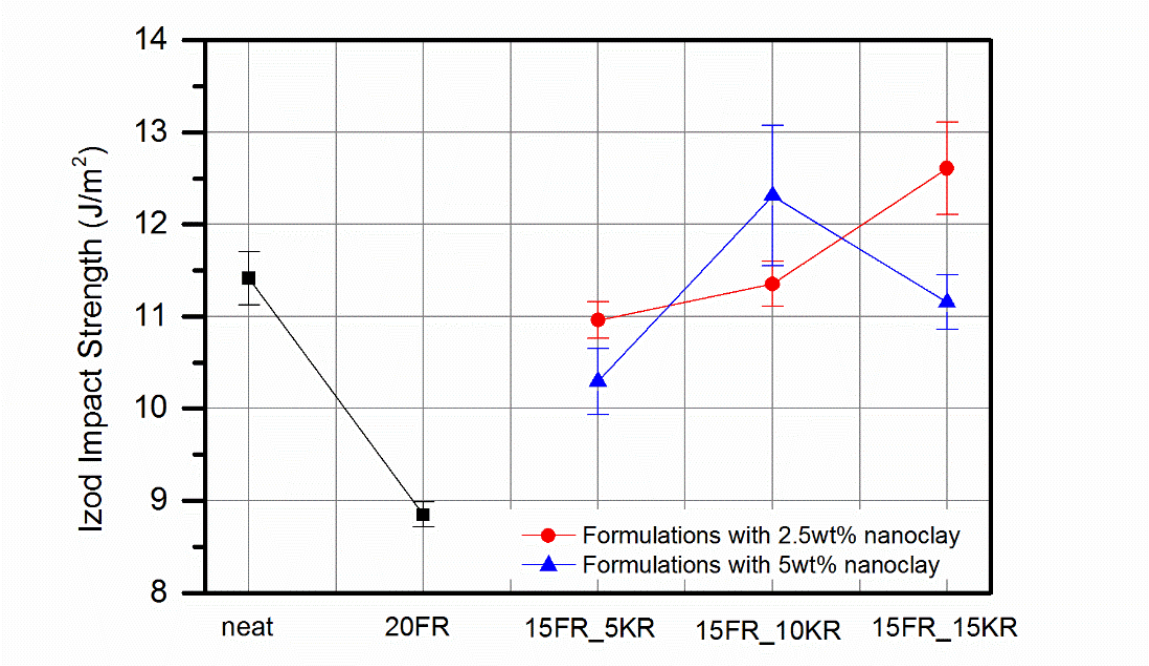

Figure 2.25. Izod impact strength of PA6 and its nanocomposites.

2.3.6 Flammability

2.3.6.1 Microscale Combustion Calorimetry

Figure 2.26 compares the heat release capacity (HRC) of rubber toughened FR PA6 formulations. Detailed MCC results are summarized in Table 2.10. Neat PA6 has a heat release capacity around 650 J/g-K which corresponds to levels typically observed in previous research [8]. Addition of 20 wt% flame retardant alone effectively reduced the HRC to 407.6 J/g-K, a value also consistent with previously published results [8]. On the other hand, blends containing both flame retardant and elastomers show interesting results. Indeed, it is notable that despite the substantially higher HRC of neat elastomer, the HRC of the ternary system did not increase with added elastomer. In contrast, MCC results for the blends containing flame retardant and elastomers show a slight decrease of HRC with increasing concentration of elastomer. All the formulations that contain elastomer and

flame retardant have slightly lower values of HRC compared to that of the formulation containing flame retardant alone. Samples with 20 wt% flame retardant and 20 wt% elastomer have the lowest heat release capacity of 368 J/g-k.

Typical MCC heat release curves of PA6/FR/elastomer formulations are shown in Figure 2.27. Because of the nature of the phosphorus intumescent FR additive discussed in Chapter 1, all FR formulations have lower onset degradation temperature than the neat PA6. Addition of the elastomers does not change the degradation temperature, but a small decrease in peak heat release rate is observed.

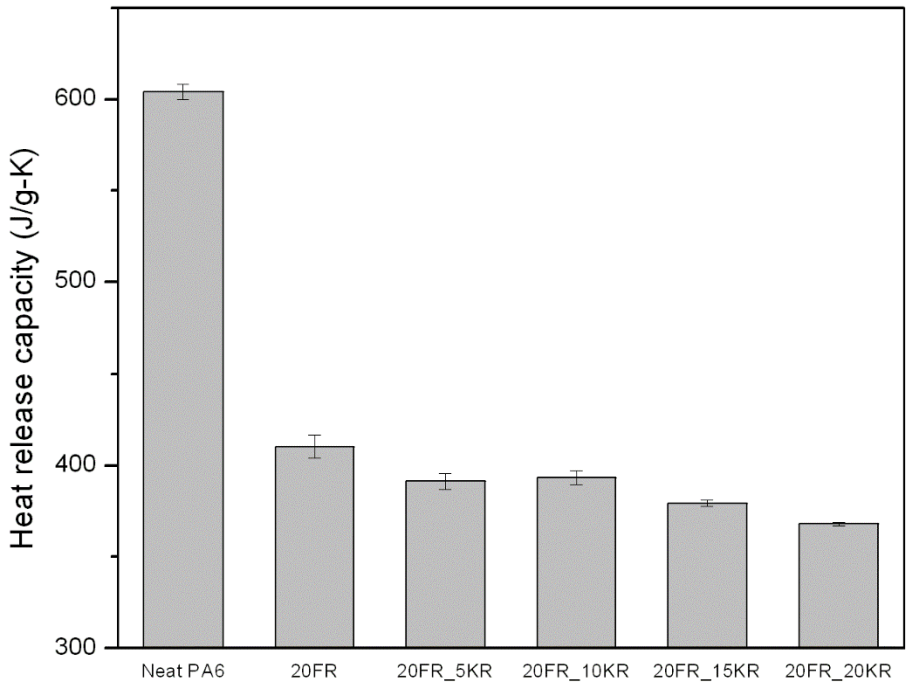

Figure 2.26. Heat release capacity of flame retardant PA6/elastomer blends.

Table 2.10. Heat release properties of neat PA6 and its polymer blends with SEBS elastomers.

Formulations	Heat Release Capacity (J/g-K)	Peak Heat Release Rate (W/g)	Total Heat Release (kJ/g)	Peak Temperature (C)
Neat PA6	604.0±4.3	705.1±4.9	29.9±0.1	482.9±0.7
20FR	407.6±6.5	472.7±7.9	26.7±0.1	442.5±1.4
20FR_5KR	391.4±4.4	456.1±5.5	26.5±0.1	455.4±0.8
20FR_10KR	393.4±3.7	458.8±4.3	27.7±0.2	451.7±2.6
20FR_15KR	379.4±1.7	442.0±1.9	28.0±0.1	453.8±6.0
20FR_20KR	368.0±1.0	429.2±1.3	28.4±0.1	447.2±0.5

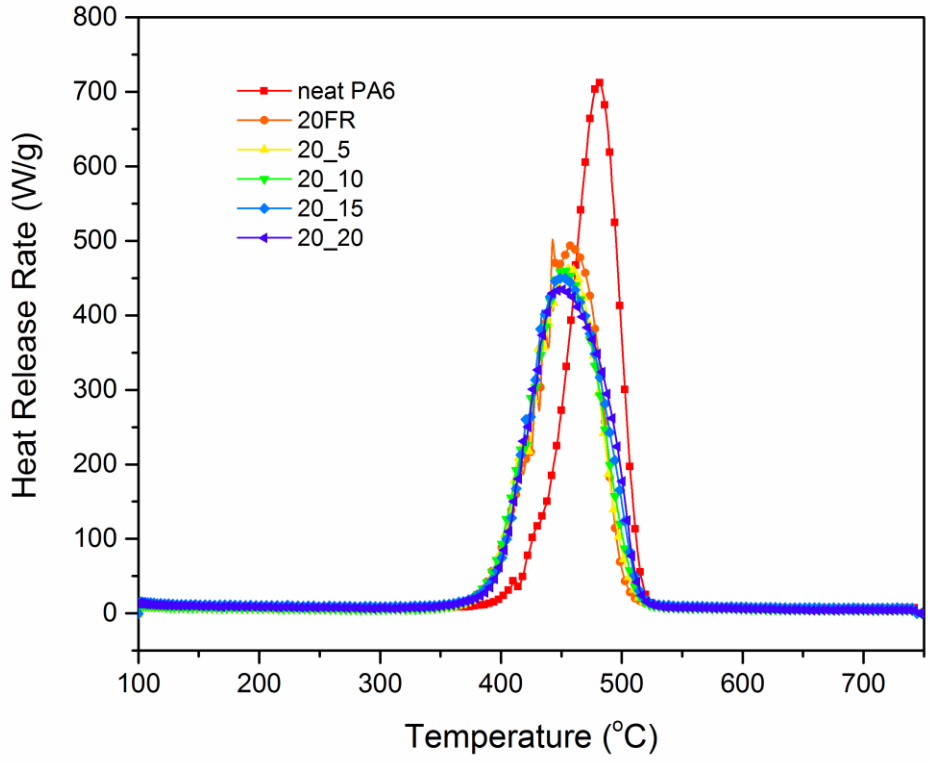

Figure 2.27. Typical heat release curves of flame retardant PA6/elastomer blends.

The impact of nanoclay addition is depicted in Figure 2.28 and Table 2.11 showing HRC of neat PA6 and seven different flame retardant formulations. With 15 wt% FR

loadings in all nanocomposite samples, lower HRC than the original 20FR sample were achieved in all formulations which is indicative of the enhancement effect between FR and nanoclay. At 10 wt% and 15 wt% elastomer level, higher concentration of nanoclay clearly leads to lower HRC. This is due to the barrier effect of a clay reinforced char layer which will be discussed in the char morphology section. However, this trend does not apply to samples with low elastomer concentration (5 wt%).

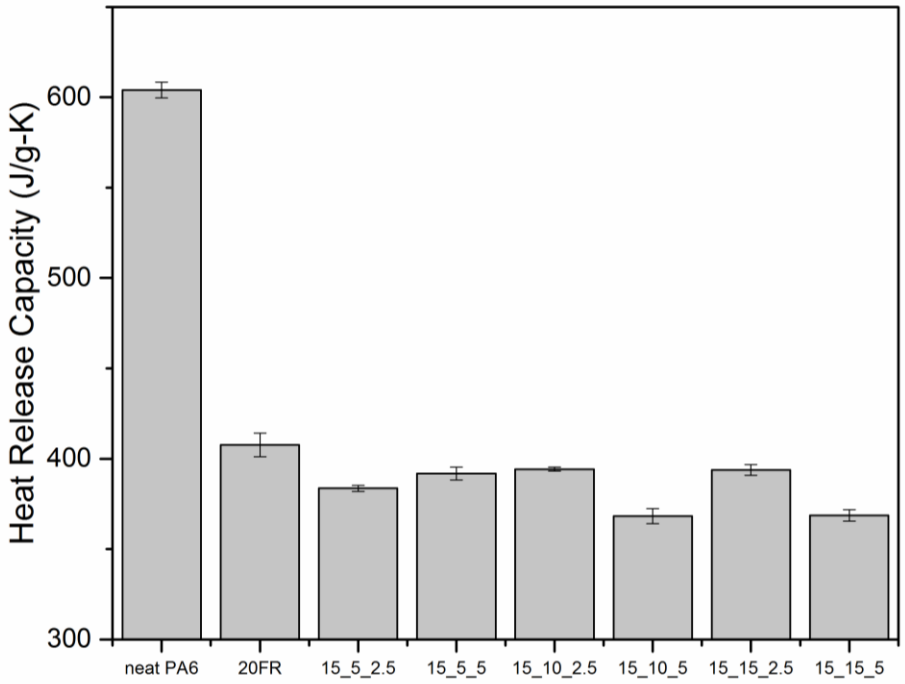

Figure 2.28. Heat release capacity of PA6 and its nanocomposites.

Table 2.11. Heat release properties of PA6 and its nanocomposites.

Formulations	Heat Release Capacity (J/g-K)	Peak Heat Release Rate (W/g)	Total Heat Release (kJ/g)	Peak Temperature (C)
15_5_2.5	383.6±1.7	537.8±2.6	28.5±0.1	474.5±0.8
15_5_5	391.8±3.5	552.8±4.8	28.0±0.5	478.4±0.5
15_10_2.5	394.2±1.1	557.0±1.4	29.3±0.0	478.0±0.4
15_10_5	368.2±4.2	517.5±5.7	28.1±0.1	479.8±0.5
15_15_2.5	393.8±3.0	554.6±4.0	29.2±0.1	480.1±0.9
15_15_5	368.6±3.2	520.9±4.3	28.4±0.1	483.4±1.1

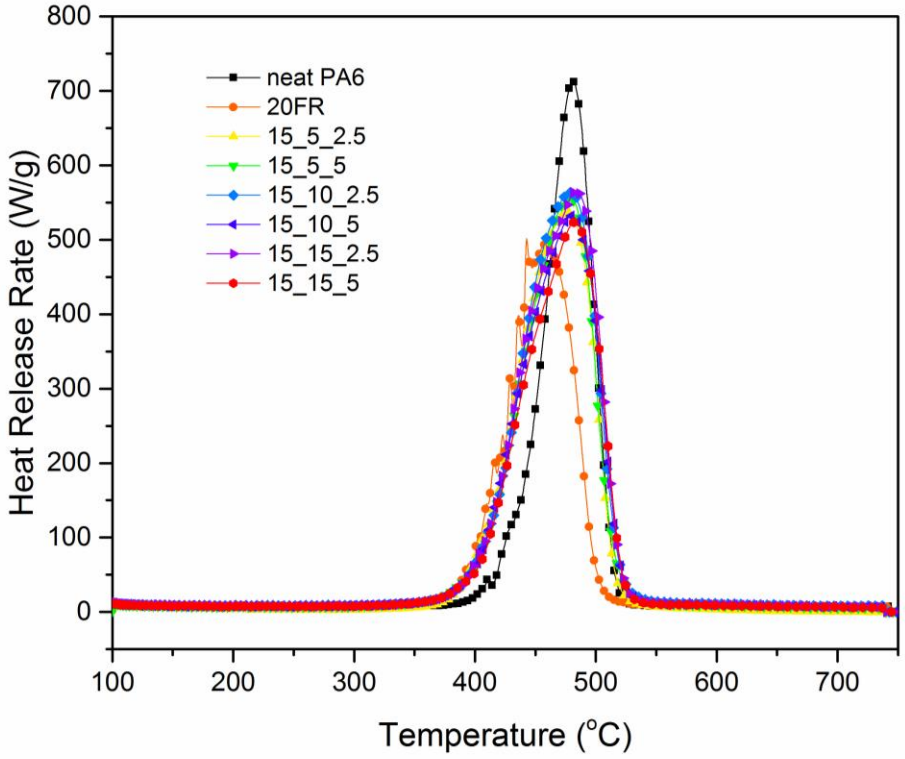

Figure 2.29. Typical heat release curves of PA6 and its nanocomposites.

2.3.6.2 UL-94 Vertical Test

UL-94 ratings of selected FR formulations are listed in Table 2.12. Pictures of post UL-94 test specimens are shown in Figure 2.30-32. Although neat PA6 eventually self–

extingushed after removal of the fire source, the polymer melt dripped and ignited the cotton indicator underneath; therefore, a worse UL-94 rating V2 rating was assigned. Addition of 20 wt% FR effectively stopped the dripping and self extinguished almost immediately after removal of the igniter. Thus a V-0 rating was satisfied. Samples with the lower elastomer content, i.e., 5, 10 and 15 wt%, appeared to retain the V-0 rating (Table 2.12) and exhibited charring behavior relatively similar to the FR formulation in the absence of elastomer (Figure 2.31, a, b, and c). However, some of the specimens in Figure 2.31-b and -c exhibit traces of burning along the edge of the bars. When 20 wt% elastomer was added to the polymer blend, the flame tended to persist longer after removal of the external heat source and only a V-1 rating was satisfied (Figure 2.31-d). Finally, the formulations combining FR, elastomer and nanoclay resulted in samples with V-0 rating (Table 2.12 and Figure 2.32).

Therefore, the rubber toughening of FR PA6 to recover material ductility while preserving FR performance appears feasible, to an extent. The addition of elastomer beyond a certain threshold appears to compromise flame resistance as characterized using the qualitative UL-94 standard. This is likely due to the higher flammability of the neat elastomer which exhibited a heat release capacity substantially higher than that of nylon. However, it was noted that in the discussion of MCC results the elastomer content had little to no effect on heat release behavior of the ternary composite formulations. Indeed, all rubber toughened formulations showed lower heat release capacity than the FR nylon alone in the absence of elastomer. This may be due to the fact that although the MCC heat release capacity measure has been shown to be a very good indicator of the fire hazard of a material, it does not perfectly correlate with incomplete burning processes like UL-94 test, where phenomena, such as charring and swelling play a role at least as important as the material's intrinsic combustion properties [35, 36].

Table 2.12. UL-94 ratings of FR PA6 formulations.

Sample	Neat	20FR	20_5	20_10	20_15	20_20
UL-94 rating	V2	V0	V0	V0	V0	V1
Sample	15_5_2.5	15_5_5	15_10_2.5	15_10_5	15_15_2.5	15_15_5
UL-94 rating	V1	V0	V0	V0	V0	V0

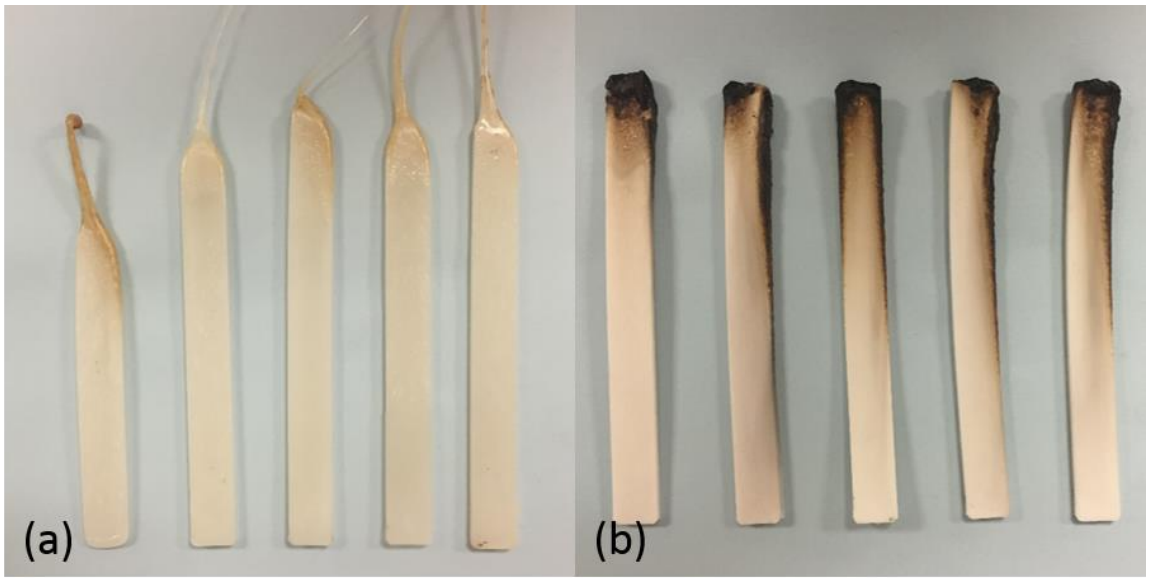

Figure 2.30. Pictures of posttest UL-94 samples (a. neat PA6 and b. 20FR).

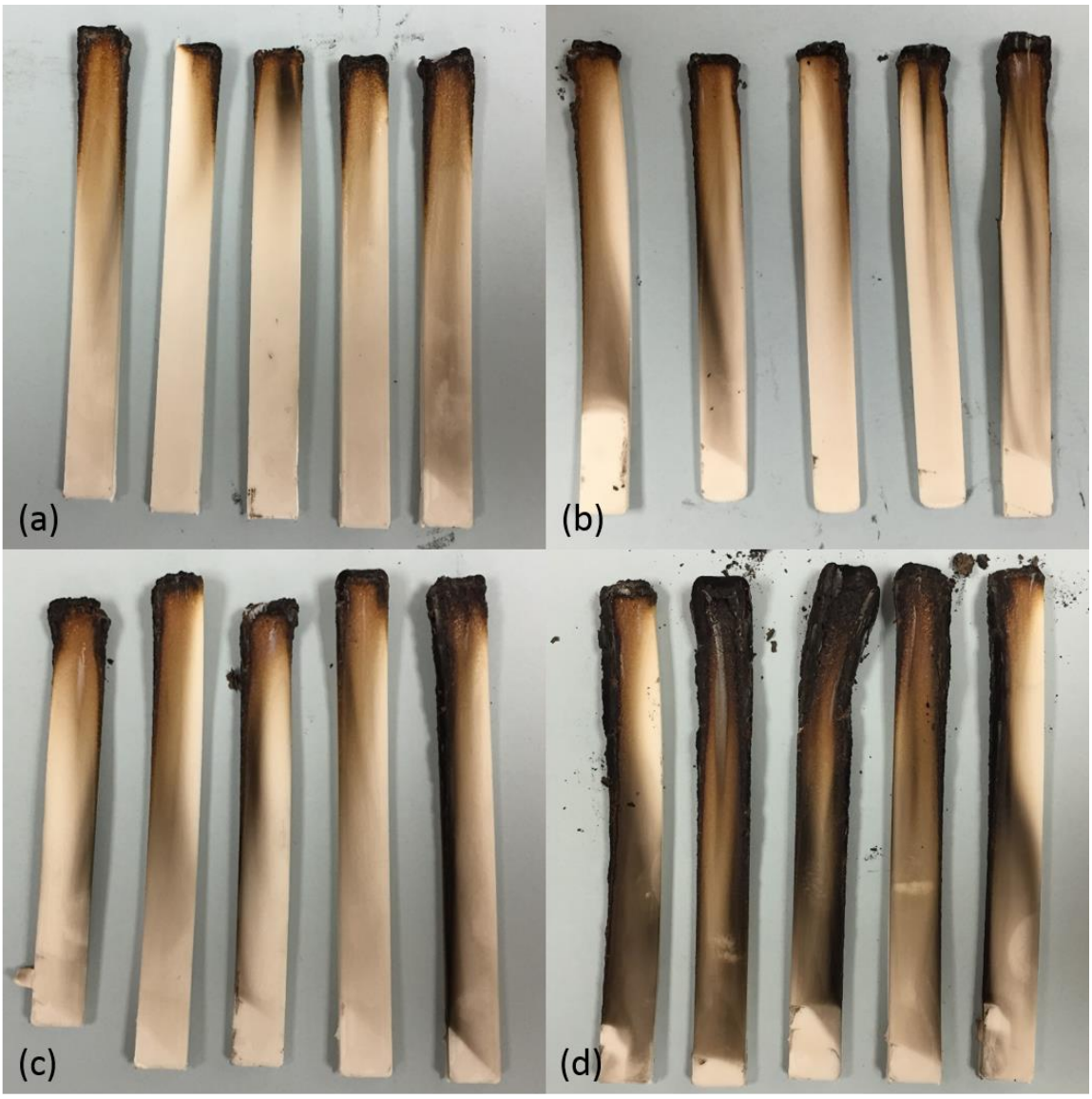

Figure 2.31. Pictures of posttest UL-94 samples of FR PA6/elastomer blend: (a) 20_5, (b) 20_10, (c) 20_15, and (d) 20_20.

Figure 2.32. Pictures of posttest UL-94 samples of rubber toughened FR PA6 nanocomposites [(a) 15_5_2.5, (b) 15_5_5, (c) 15_10_2.5, (d) 15_10_5, (e) 15_15_2.5, and (f) 15_15_5].

2.3.6.3 Limiting Oxygen Index (LOI)

LOI results of the rubber toughened FR PA6 samples are shown in Figure 2.33. Even though neat PA6 has an LOI of 26.6 which is higher than the oxygen concentration in air, the melt dripping remains a problem. All FR formulations have LOI higher than the neat PA6 indicating better flame retardant properties. At 20 wt% FR level, adding 10 wt% of elastomer result in lower LOI values compared to the original PA6/FR system. When comparing formuations with same amount of FR and elastomer, higher loadings of nanoclay yield higher LOI values.

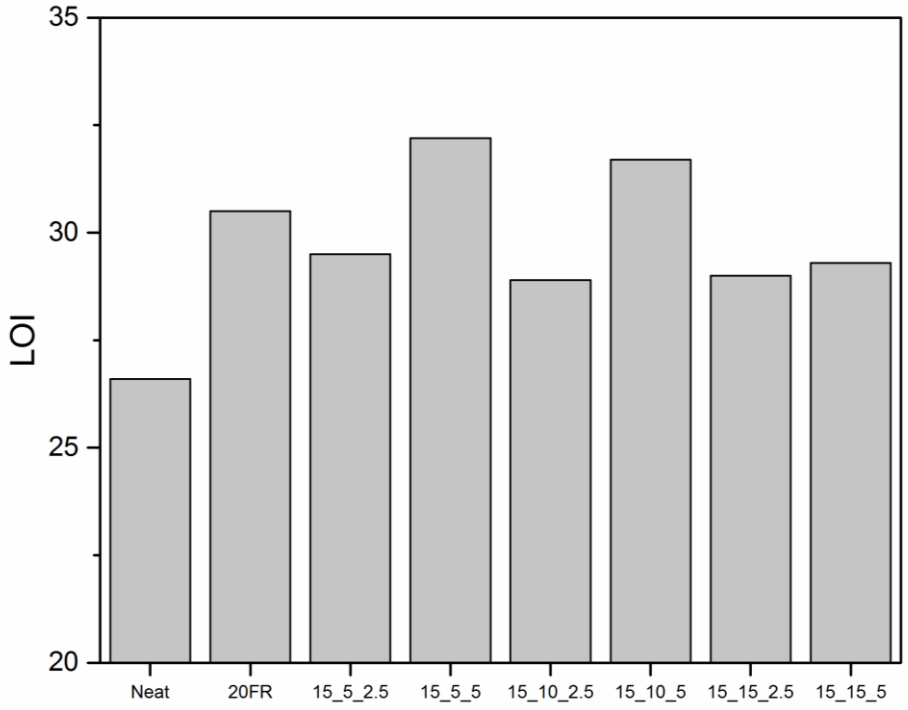

Figure 2.33. LOI comparison of rubber toughened FR PA6 nanocomposites.

Table 2.13. LOI values of FR PA6 formulations.

Sample	Neat	20FR	20_10	15_5_2.5	15_5_5	15_10_2.5	15_10_5	15_15_2.5	15_15_5
LOI	26.6	30.5	28.1	29.5	32.2	28.9	31.7	29.0	29.3

2.3.6.4 Char Morphology

High resolution SEM images of char surface after combustion tests show different char morphologies between samples containing FR particles in the absence of elastomer and those containing both FR and rubber additives. For samples containing 20 wt% FR (20FR) with no elastomer, the char surface is exclusively characterized by a highly granulated porous structure composed of micron-sized particles (Figure 2.34). Higher magnification images in Figure 2.34 reveal that these micro-sized particles are hollow. These hollow char particles were probably formed during the decomposition of PA6 and the flame retardants, a process in which the decomposition products include ammonia, carbon dioxide, water, caprolactam, phosphinic acid, phosphinate, and ethane [38]. Energy dispersive X-ray spectroscopy (EDS) on the char layers show signals of aluminum, zinc, and phophaspate which are the constituent elements of the flame retardant (Figure 2.34).

The same porous char surface structure was also found in sample 20_15. However, a different char morphology with fully covered char surface was also observed as shown in Figure 2.35. In this char structure, air bubbles generated from combustion can also be clearly seen. High resolution images from a cracked air bubble show a densely packed char layer about 200 nm thick. It should be noted that this type of fully covered char structure only covers a small portion of the whole char surface, especially around the char edge.

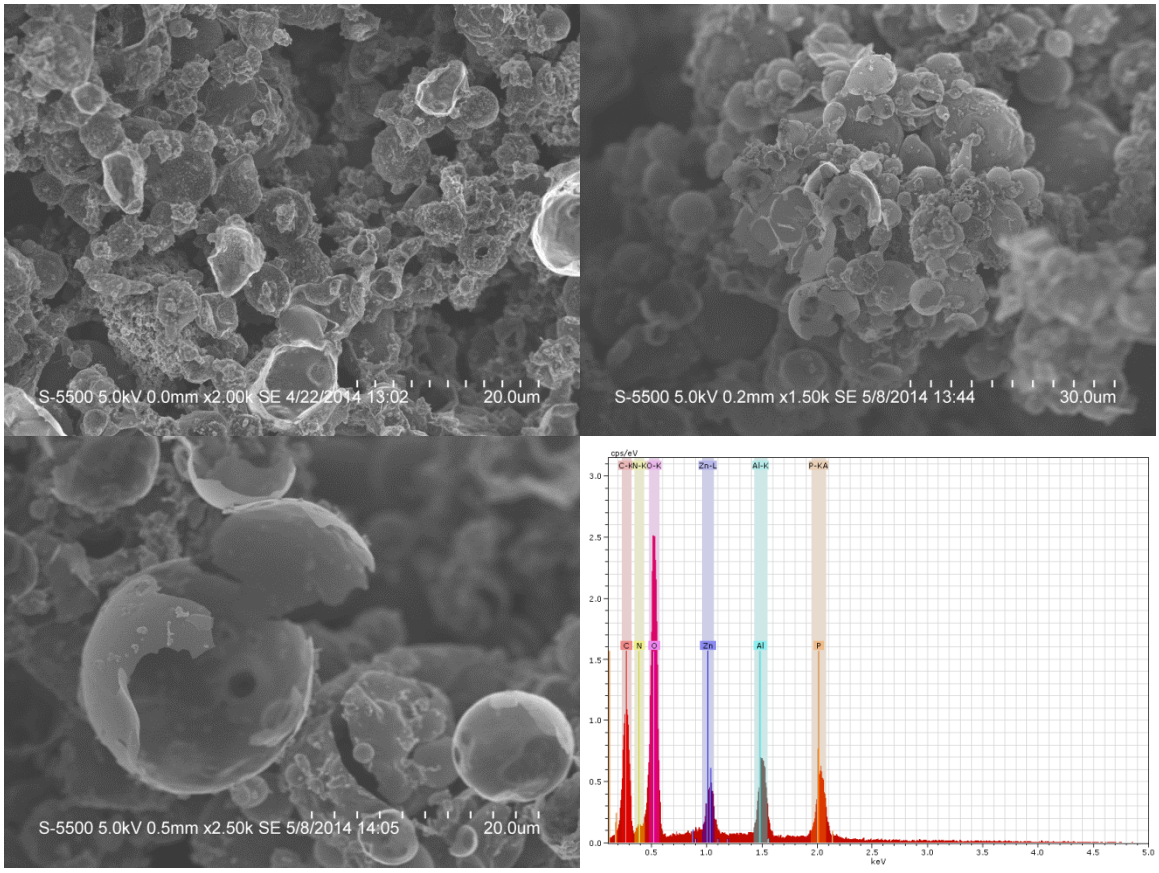

Figure 2.34. SEM images and EDS spectrum of the char surface of sample #2 containing 20 wt% intumescent flame retardant.

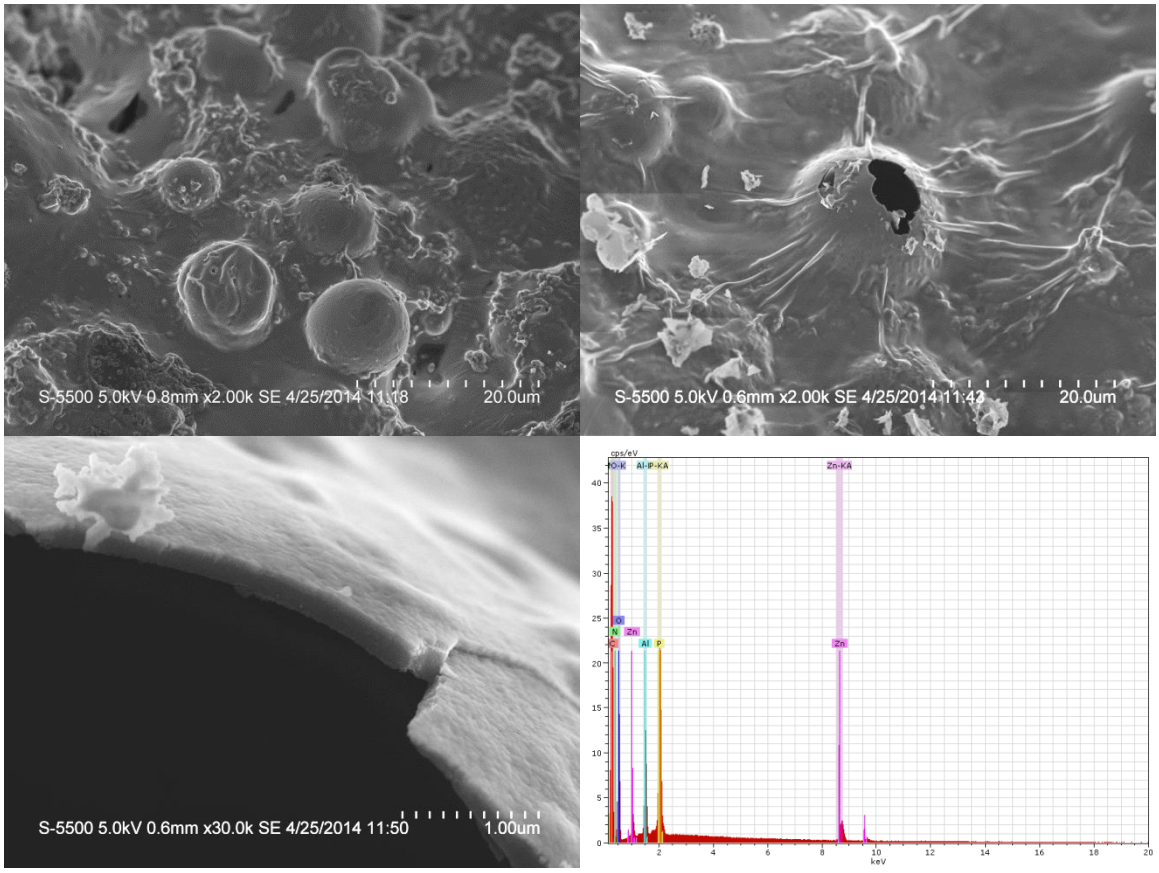

Figure 2.35. SEM images and EDS spectrum of the char surface of sample #5 containing 20 wt% intumescent flame retardant and 15 wt% elastomer.

Figure 2.36 below shows the char surface of nanocomposite sample 15_5_5 containing 15 wt% flame retardant, 15 wt% elastomer, and 5 wt% nanoclay. The char morphology is very different from the previous two samples: a coherent thick char layer covers most of the surface except some air bubbles. A closer look, shown on the right side, clearly reveals the stacked clay platelets.

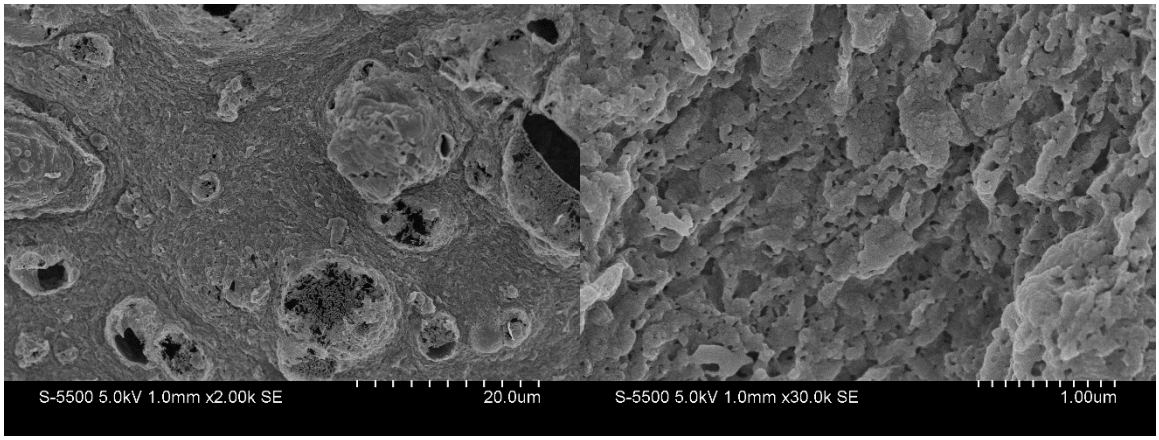

Figure 2.36. Top view of char morphology of sample #12 containing 15 wt% flame retardant, 15 wt% Kraton elastomer, and 5 wt% nanoclay.

Cross sectional view of sample #12 in Figure 2.37 show a char layer with thickness greater than 20 μm. Such a thick char layer may act as a better thermal shield, protecting virgin materials underneath the pyrolysis zone. Higher magnification images show closely packed char structures of clay layers. It needs to be noted that such char does not only exist on the surface of the specimen; it was also observed beneath the surface forming a 3D cellular structure throughout the char thickness.

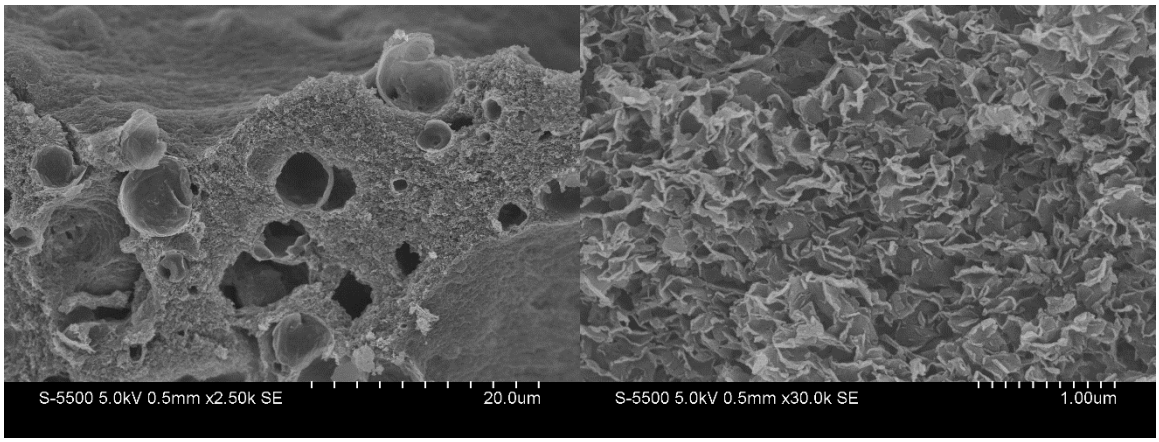

Figure 2.37. Cross sectional view of char morphology of sample #12 containing 15 wt% flame retardant, 15 wt% Kraton elastomer, and 5 wt% nanoclay.

2.4 CONCLUSION

In this chapter, rubber toughening of flame retardant PA6 and its nanocomposites was investigated in order to determine the feasibility of recovering ductile behavior and impact strength without sacrificing flame resistance. Flame retardant PA6/elastomer and PA6 elastomer/nanoclay blends with various contents of maleic anhydride modified SEBS elastomer were prepared by twin screw melt mixing.

The skin part of all the injection molded FR PA6 samples are primarily γ crystals while the core contains both α and γ crystals. TEM micrographs show an even distribution of flame retardant, elastomer and nanoclay particles. The PA6 crystal lamellae have preferential direction around the rubber particles. In addition, the recovery of elongation at break and improvement of impact strength were achieved without compromising flame retardant functionality.

From the first heating curves of the DSC results, it is found that the addition of flame retardant increased crystallinity of nylon whereas high concentrations of nanoclay result in lower crystallinity due to limited space for lamella growth. Micro-scale combustion calorimetry tests show that adding 20 wt% flame retardant could effectively lower the heat release capacity. Rubber toughening of the FR system, i.e., polymer blends with both flame retardant and elastomer, further reduced the heat release capacity compared to the original FR system in the absence of rubber. This improvement could be explained by a consolidated char surface structure as revealed by high resolution SEM images. These observations were consistent across all levels of rubber contents. However, UL-94 tests revealed a slightly degraded FR performance when elastomer content exceeded some threshold in the 15-20 wt% range. Nevertheless, rubber loadings of up to 15 wt% were possible while still achieving the highest UL-94 V0 rating. To further improve the flame retardant properties, a small amount of nanoclay was introduced to the system. The

enhancement effect of the nanocomposite FR formulations are observed from MCC results. Formulations with 15 wt% flame retardant, 10 wt% elastomer, and 5 wt% nanoclay also achieved UL-94 V-0. In conclusion, PA6/FR/elastomer/nanoclay nanocomposite blends could provide effective flame retardant performance with improved toughness and preserved ductility for the fiber spinning process.

2.5 REFERENCES

[1] S.V. Levchik, E.D. Weil, Combustion and fire retardancy of aliphatic nylons, Polymer International 49(10) (2000) 1033-1073.
[2] J.W. Gilman, T. Kashiwagi, J.D. Lichtenhan, Nanocomposites: a revolutionary new flame retardant approach, SAMPE Journal 33 (1997) 40-46.
[3] J.W. Gilman, Flammability and thermal stability studies of polymer layered-silicate (clay) nanocomposites, Applied Clay Science 15(1-2) (1999) 31-49.
[4] S. Bourbigot, S. Duquesne, C. Jama, Polymer Nanocomposites: How to Reach Low Flammability?, Macromolecular Symposia 233(1) (2006) 180-190.
[5] S. Bourbigot, S. Duquesne, G. Fontaine, S. Bellayer, T. Turf, F. Samyn, Characterization and reaction to fire of polymer nanocomposites with and without conventional flame retardants, Molecular crystals and liquid crystals 486(1) (2008) 325-1367.
[6] U. Braun, B. Schartel, M.A. Fichera, C. Jäger, Flame retardancy mechanisms of aluminium phosphinate in combination with melamine polyphosphate and zinc borate in glass-fibre reinforced polyamide 6,6, Polymer Degradation and Stability 92(8) (2007) 1528-1545.
[7] M. Doğan, E. Bayramlı, The flame retardant effect of aluminum phosphinate in combination with zinc borate, borophosphate, and nanoclay in polyamide-6, Fire and Materials 38(1) (2014) 92-99.
[8] H. Wu, M. Krifa, J.H. Koo, Flame retardant polyamide 6/nanoclay/intumescent nanocomposite fibers through electrospinning, Textile Research Journal 84(10) (2014) 1106-1118.
[9] E.D. Weil, S. Levchik, Current Practice and Recent Commercial Developments in Flame Retardancy of Polyamides, Journal of Fire Sciences 22(3) (2004) 251-264.
[10] Y.
C. Ahn, D.R. Paul, Rubber toughening of nylon 6 nanocomposites, Polymer 47(8) (2006) 2830-2838.
[11] A.J. Oshinski, H. Keskkula, D.R. Paul, Rubber toughening of polyamides with functionalized block copolymers: 1. Nylon-6, Polymer 33(2) (1992) 268-283.
[12] A.J. Oshinski, H. Keskkula, D.R. Paul, The role of matrix molecular weight in rubber toughened nylon 6 blends: 1. Morphology, Polymer 37(22) (1996) 4891-4907.
[13] O.K. Muratoglu, A.S. Argon, R.E. Cohen, M. Weinberg, Toughening mechanism of rubber-modified polyamides, Polymer 36(5) (1995) 921-930.
[14] C. Siat, M. Le Bras, S. Bourbigot, Combustion behaviour of ethylene vinyl acetate copolymer-based intumescent formulations using oxygen consumption calorimetry, Fire and Materials 22(3) (1998) 119-128.
[15] M. Le Bras, S. Bourbigot, E. Félix, F. Pouille, C. Siat, M. Traisnel, Characterization of a polyamide-6-based intumescent additive for thermoplastic formulations, Polymer 41(14) (2000) 5283-5296.

[16] Honeywell Resins and Chemicals, Product Specification: Aegis®H95ZI, https://www.honeywell-nylon6.com/?document=honeywell-aegis-h95zi-datasheet&download=1, (January 2010).
[17] Clariant GmbH, Division Pigments & Additives, Exolit® OP1312 Technical Datasheet, (2004).
[18] Product datasheet OP1312, Clariant, (2011).
[19] D.M. Laura, H. Keskkula, J.W. Barlow, D.R. Paul, Effect of rubber particle size and rubber type on the mechanical properties of glass fiber reinforced, rubber-toughened nylon 6, Polymer 44(11) (2003) 3347-3361.
[20] KRATON® FG1901 G Polymer Techinical Datasheet, http://docs.kraton.com/tl_warehouse/pdf_data_docs/WG_17864_WGC843.tmp.pdf, (2015).
[21] Cloisite® 30B Typical Physical Properties Bulletin, Southern Clay Products, (2012) p. 2.
[22] A.R. Horrocks, Flame retardant challenges for textiles and fibres: New chemistry versus innovatory solutions, Polymer Degradation and Stability 96(3) (2011) 377-392.
[23] G. Gururajan, S.P. Sullivan, T.P. Beebe, D.B. Chase, J.F. Rabolt, Continuous electrospinning of polymer nanofibers of Nylon-6 using an atomic force microscope tip, Nanoscale 3(8) (2011) 3300-3308.
[24] I.K. Melvin, M.I. Kohan, Nylon Plastics Handbook, Hanser/Gardner Publications, (1995).
[25] J.J. Huang, H. Keskkula, D.R. Paul, Rubber toughening of an amorphous polyamide by functionalized SEBS copolymers: morphology and Izod impact behavior, Polymer 45(12) (2004) 4203-4215.
[26] S. Wu, A generalized criterion for rubber toughening: The critical matrix ligament thickness, Journal of Applied Polymer Science 35(2) (1988) 549-561.
[27] T.D. Fornes, D.R. Paul, Crystallization behavior of nylon 6 nanocomposites, Polymer 44(14) (2003) 3945-3961.
[28] T.M. Wu, E.-C. Chen, C.-S. Liao, Polymorphic behavior of nylon 6/saponite and nylon 6/montmorillonite nanocomposites, Polymer Engineering & Science 42(6) (2002) 1141-1150.
[29] A. Usuki, A. Koiwai, Y. Kojima, M. Kawasumi, A. Okada, T. Kurauchi, O. Kamigaito, Interaction of nylon 6-clay surface and mechanical properties of nylon 6-clay hybrid, Journal of Applied Polymer Science 55(1) (1995) 119-23.
[30] S.C. Lao, W. Yong, K. Nguyen, T.J. Moon, J.H. Koo, L. Pilato, G. Wissler, Flame-retardant polyamide 11 and 12 nanocomposites: processing, morphology, and mechanical properties, J. Compos. Mater. 44(25) (2010) 2933-2951.
[31] A. Dasari, Z.-Z. Yu, Y.-W. Mai, Effect of blending sequence on microstructure of ternary nanocomposites, Polymer 46(16) (2005) 5986-5991.
[32] I. Kelnar, J. Kotek, L. Kaprálková, B.S. Munteanu, Polyamide nanocomposites with improved toughness, Journal of Applied Polymer Science 96(2) (2005) 288-293.

[33] S.C. Tjong, S.P. Bao, Impact fracture toughness of polyamide-6/montmorillonite nanocomposites toughened with a maleated styrene/ethylene butylene/styrene elastomer, Journal of Polymer Science Part B: Polymer Physics 43(5) (2005) 585-595.
[34] H. Wu, X. Yin, M. Krifa, M. Londa, J. Koo, Fabrication and Characterization of Flame Retardant Polyamide 6 Nanocomposites via Electrospinning, SAMPE TECH 2011, Fort Worth, TX, (2011).
[35] R.E. Lyon, R.N. Walters, S.I. Stoliarov, Screening flame retardants for plastics using microscale combustion calorimetry, Polymer Engineering & Science 47(10) (2007) 1501-1510.
[36] H.Q. Peng, Q. Zhou, D.-Y. Wang, L. Chen, Y.-Z. Wang, A novel charring agent containing caged bicyclic phosphate and its application in intumescent flame retardant polypropylene systems, Journal of Industrial and Engineering Chemistry 14(5) (2008) 589-595.
[37] U. Braun, H. Bahr, B. Schartel, Fire retardancy effect of aluminium phosphinate and melamine polyphosphate in glass fibre reinforced polyamide 6, e-Polymers (2010).

Chapter 3: Thermal Analysis of FR Nylon 6 Nanocomposites

3.1 INTRODUCTION

Thermal analysis measures materials' physical property change in a heating or cooling process. The goal is to establish relationships between temperature and physical properties in order to predict the latter. Many techniques have been developed for characterization of different thermal physical properties. Examples include differential scanning calorimetry (DSC), thermogravimetric analysis (TGA), and dynamic mechanical analysis (DMA). In this study, two isoconversion methods based on TGA tests are used to calculate the kinetic activation energy of different FR PA6 nanocomposite formulations. The influence of each component used will be discussed [1, 2].

3.2 KINETIC MODELS FOR THERMAL DECOMPOSITION

Thermal stability and kinetic parameters of a polymer can be characterized by TGA. This important information could help researchers gain insight into the thermal decomposition process at elevated temperatures. It can also help evaluate a material's processing and storage conditions as well as service lifetime. The goal is to establish a mathematical model that can provide the relationship between time, temperature, and fractional conversion, or in thermogravimetric analysis, the fractional mass loss of the polymer [1, 3].

For constant pressure conditions, the rate of decomposition process or conversion rate is usually simplified as a function of temperature (T) and fractional conversion (α) [1, 3]. The temperature can be controlled by the TGA instrument and the conversion is determined from TGA mass loss data. α at a given temperature is defined as [1]:

$$\alpha = \frac{w_0 - w_T}{w_0 - w_f} \tag{3.1}$$

where w_0 and w_f are the initial and final mass and w_T is the mass at temperature T.

For single step processes, the conversion rate can be calculated as the product of two individual functions, one is solely a function of temperature T and the other is solely a function of conversion α [1]:

$$\frac{d\alpha}{dt} = k(T)f(\alpha) \tag{3.2}$$

where $k(T)$ is the rate constant and $f(\alpha)$ is the reaction model. The temperature dependent function is generally simplified by an Arrhenius equation [1]:

$$k(T) = Aexp\left(\frac{-E_a}{RT}\right) \tag{3.3}$$

Where A is the pre-exponential factor, E_a is the activation energy and R is the universal gas constant. The term Kinetic triplet, often referred to in many publications, includes the reaction model $f(\alpha)$, the pre-exponential factor A, and the activation energy E_a [4].

Isothermal and isoconversion methods are two categories of commonly used methods to evaluate the conversion rate. Isothermal methods hold the temperature constant by fast heating and measure the conversion α vs time t. They are used to analyze reaction model $f(\alpha)$. The name isoconversion method originated from the assumption that at a given conversion the reaction rate is a function of temperature only. Isoconversion tests are typically performed at constant heating rates. The Isoconversion tests are more robust because they can also be used to calculate changing E_a vs. α for multi-step conversion processes.

Assuming that $k(T)$ is independent of α and $f(\alpha)$ is independent of T, integration of equation 3.2 can be written as [1]:

$$F(\alpha) = \int_{\alpha_0}^{\alpha} \frac{d\alpha'}{f(\alpha')} = \int_0^t k(T)dt' = \int_0^t Ae^{-E_a/RT}dt' \tag{3.4}$$

Where $F(\alpha)$ represents the mass loss function [4].

For isoconversion methods, a constant heating rate $\beta = {dT}/{dt}$ is applied and equation 3.4 can be rewritten as [1]:

$$F(\alpha) = \frac{A}{\beta}\int_{T_0}^{T} e^{-E_a/RT'}dT' \tag{3.5}$$

Equation 3.5 have no exact solution therefore different approximation methods have been used. One approximation by Doyle [5] gives:

$$F(\alpha) \approx 7.03 \times 10^{-3}\frac{AE_a}{\beta R}e^{-1.052E_a/RT} \tag{3.6}$$

For *Ea/RT>20*, The Flynn Wall and Ozawa gives:

$$ln\beta = \ln(AE_a(\alpha)/R) - 5.33 - \ln(1-\alpha) - 1.05\,(E_a/RT(\alpha)) \tag{3.7}$$

Where the activation energy E_a is determined from the slope of the $ln\beta$ vs. $1/T(\alpha)$ plot.

Lyon's method is based on approximations of the Arrhenius integral in which the activation energy is expressed as [1]:

$$E_a(\alpha) = -R\left[\frac{dln\beta}{d\,1/T(\alpha)} + 2T(\alpha)\right] \tag{3.8}$$

A detailed comparison of different isoconversion methods can be found in a review paper by Starink [4]. Both models require TGA test at multiple constant heating rates. In this study, four heating rates are used: 5, 10, 20 and 40 °C/min. TGA tests were performed using a TGA AutoTGA 2950HR from TA Instrument in nitrogen environment.

3.3 RESULTS AND DISCUSSION

Six formulations were chosen for thermal stability characterization: neat PA6, 20FR, 20_5, 20_10, 15_5_2.5 and, 15_5_5 (see Table 2.5). The TGA curves and the logarithm of heating rate β vs. 1/T at various fractional mass conversion α are plotted in Figure 3.1-6.

TGA thermographs show a typical single step decomposition for all samples, with a consistent shift to the right as the heating rate increases. The lnβ vs 1/T plots show good linearity, which indicate that both Lyon's and Flynn Wall and Ozawa's methods will be suitable for the isoconversion activation energy calculation.

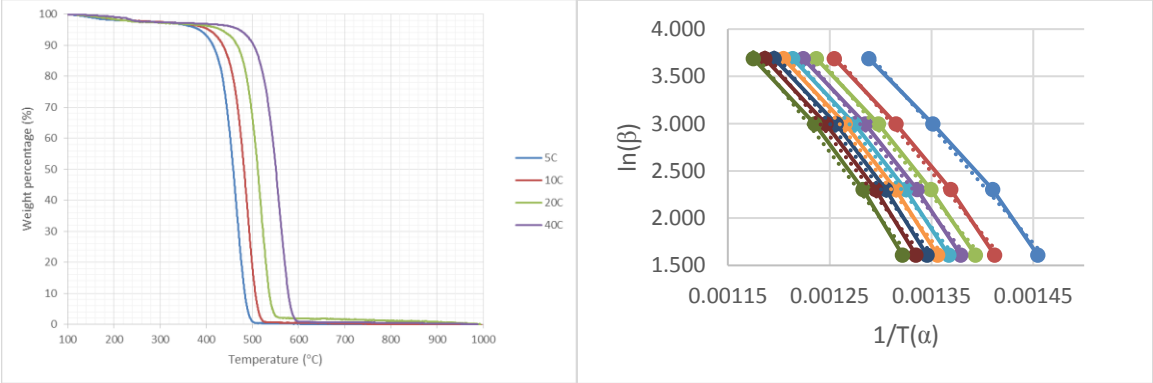

Figure 3.1. TGA mass loss curve and plot of natural logarithm of heating rate β versus the reciprocal temperature for conversion α from 0.1 to 0.9 (left to right) for neat PA6.

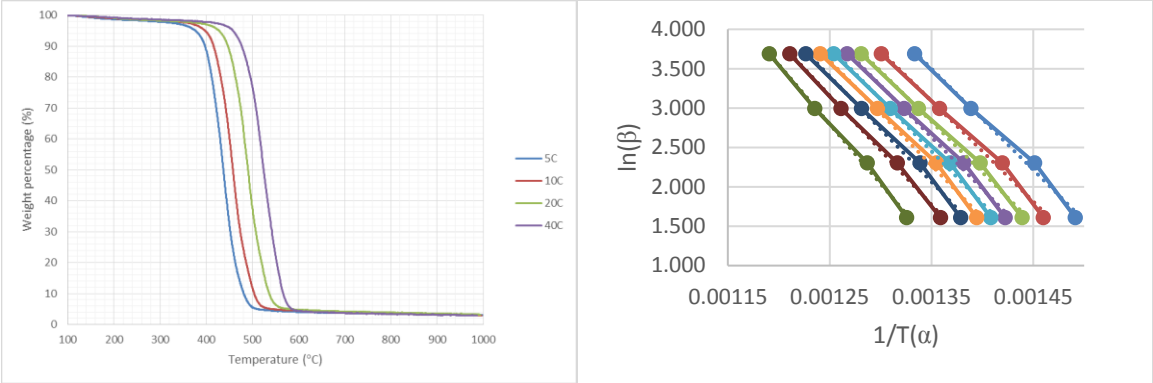

Figure 3.2. TGA mass loss curve and plot of natural logarithm of heating rate β versus the reciprocal temperature for conversion α from 0.1 to 0.9 (left to right) for PA6 with 20 wt% FR.

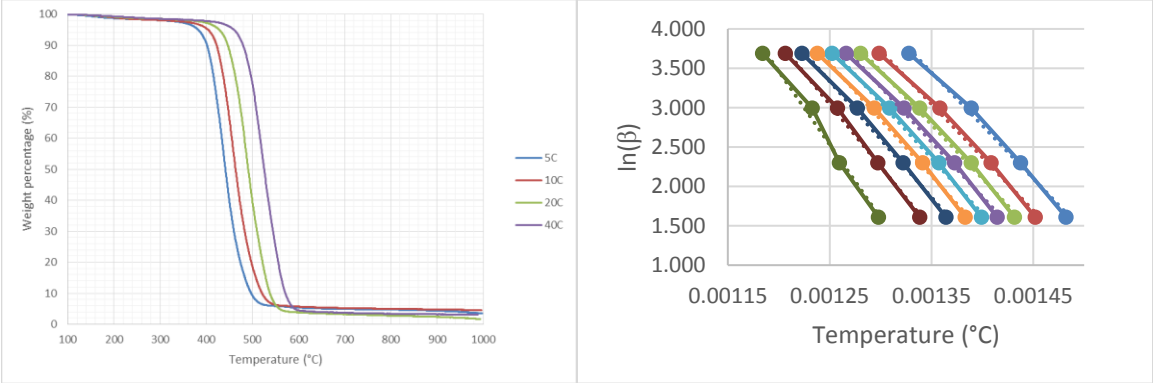

Figure 3.3. TGA mass loss curve and plot of natural logarithm of heating rate β versus the reciprocal temperature for conversion α from 0.1 to 0.9 (left to right) for PA6 with 20 wt% FR and 5 wt% elastomer.

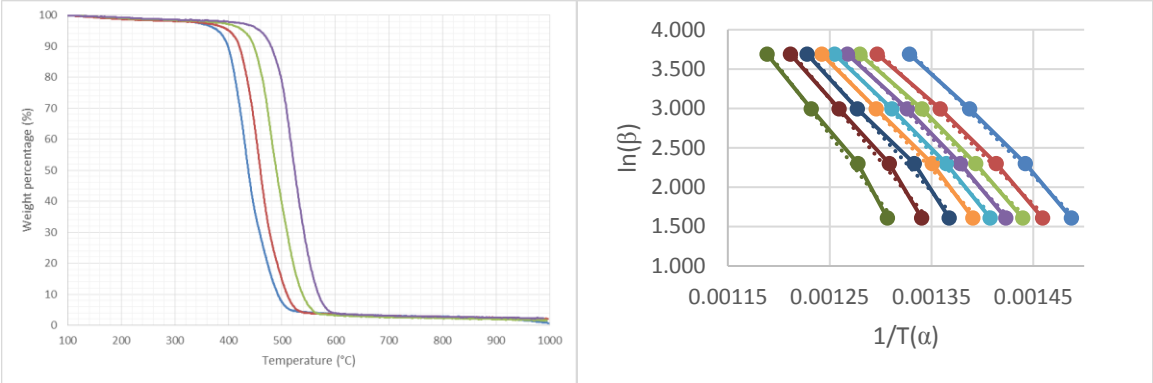

Figure 3.4. TGA mass loss curve and plot of natural logarithm of heating rate β versus the reciprocal temperature for conversion α from 0.1 to 0.9 (left to right) for PA6 with 20 wt% FR and 10 wt% elastomer.

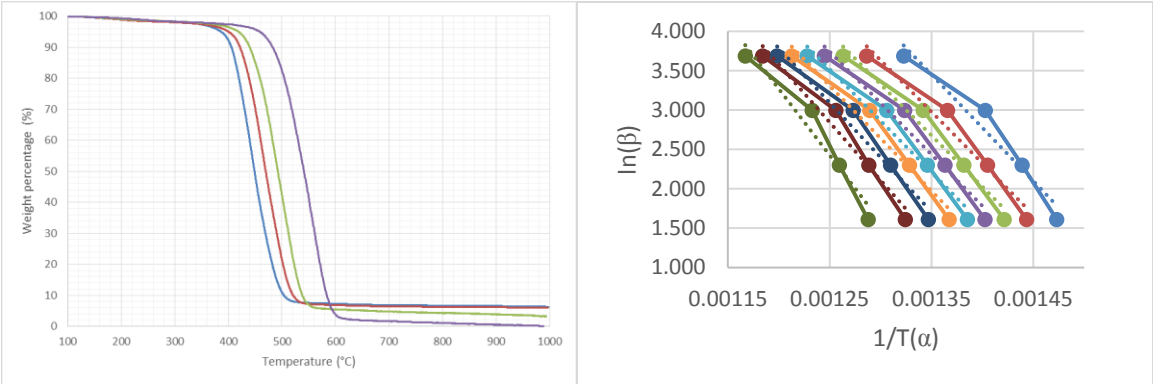

Figure 3.5. TGA mass loss curve and plot of natural logarithm of heating rate β versus the reciprocal temperature for conversion α from 0.1 to 0.9 (left to right) for neat PA6 with 15 wt% FR, 5 wt% elastomer and 2.5 wt% nanoclay.

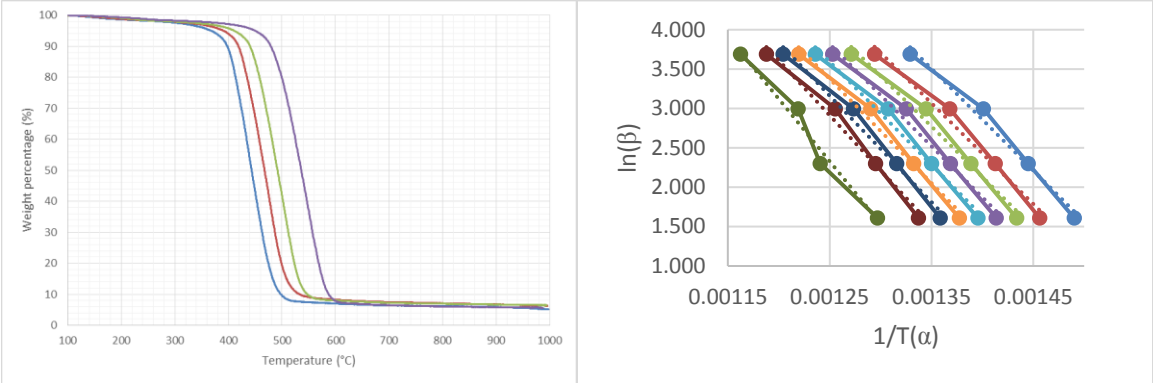

Figure 3.6. TGA mass loss curve and plot of natural logarithm of heating rate β versus the reciprocal temperature for conversion α from 0.1 to 0.9 (left to right) for neat PA6 with 15 wt% FR, 5 wt% elastomer and 5 wt% nanoclay.

Each slope in the lnβ vs 1/T plot corresponds to the activation energy at the given conversion. The activation energies at various conversions for all the selected samples are plotted in Figure 3.7 and the average activation energies are summarized in Table 3.1. For all six formulations, the activation energy increases with α. All samples show a steady increase in E_a for conversion from 0.1 to 0.7, while the increase becomes more significant for high α values at 0.8 and 0.9. This increase in activation energy with conversion may be related to two overlapped modes of thermal decomposition. At lower conversions or low temperatures, the decomposition is initiated by the weak links in nylon polymer chain, at higher extent of conversion, the dominant decomposition occurs by random scission and chain stripping which needs higher activation energy. The calculated activation energy shown in Figure 3.7 are composite values that take both modes of decomposition into account.

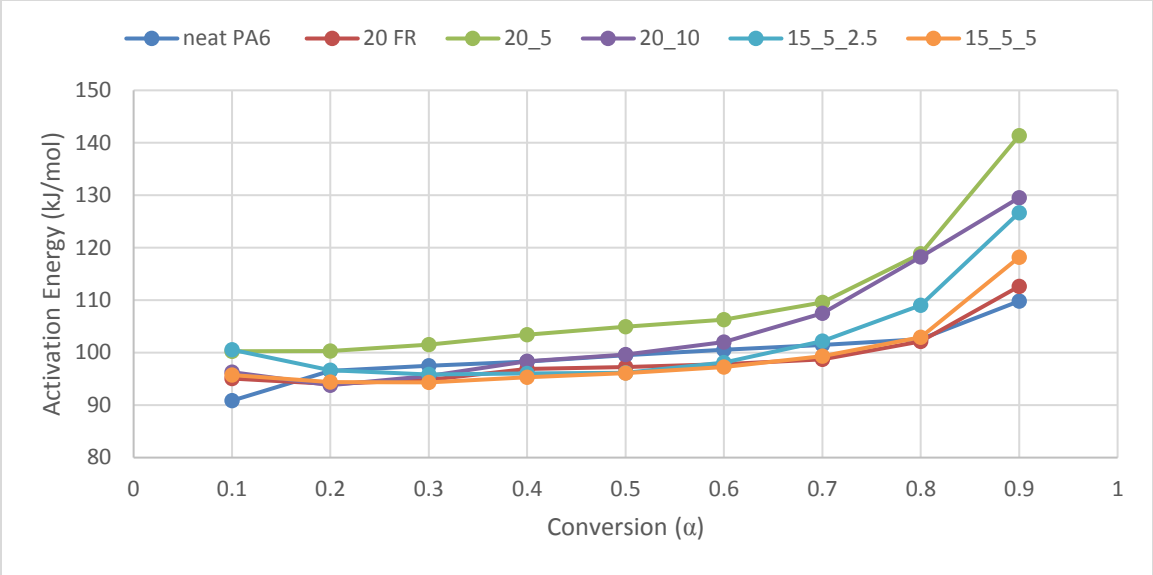

Figure 3.7. Activation energy versus conversion for selected FR PA6 formulations (Lyon's method).

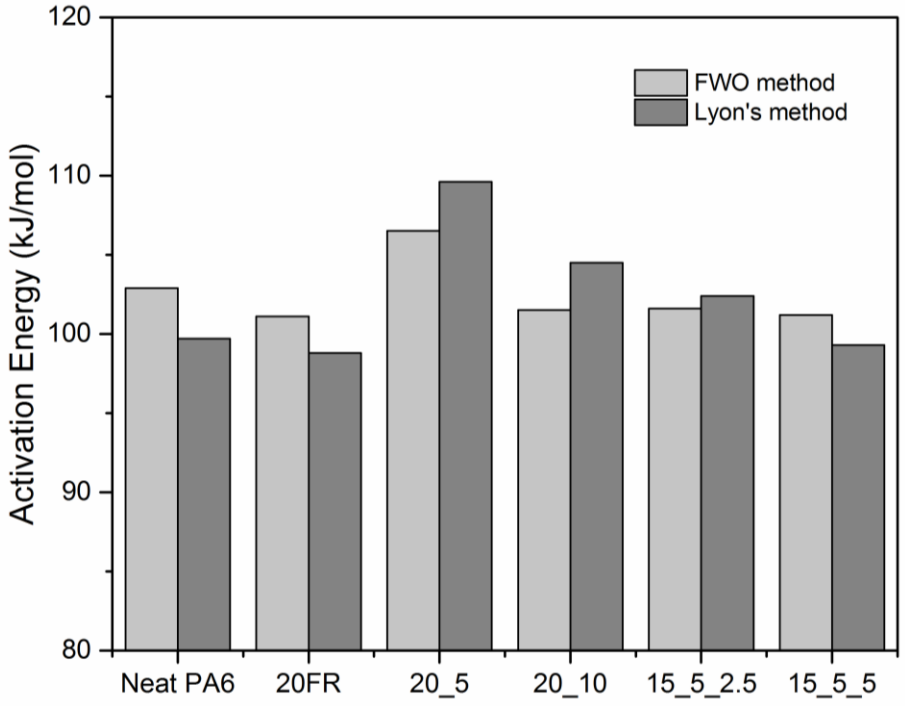

Figure 3.8. Comparison of activation energies of selected FR PA6 formulations using two isoconversion approximations.

Table 3.1. Average activation energies of selected FR PA6 formulations ($E_{a,1}$ is calculated from Ozawa method and $E_{a,2}$ is calculated from Lyon's method).

Sample	$E_{a,1}^*$ (kJ/mol)	$E_{a,2}^*$ (kJ/mol)
Neat PA6	102.9	99.7
20FR	101.1	98.8
20_5	106.5	109.6
20_10	101.5	104.5
15_5_2.5	101.6	102.4
15_5_5	101.2	99.3

The difference in calculated activation energy between the two methods is small across formulations (Table 3.1). To simplify the discussion, only the $E_{a,1}$ value from Lyon's method will be used in the following context (Figure 3.8). Neat PA6 has an activation energy of 99.7 kJ/mol. Adding 20 wt% FR slightly reduces the E_a to 98.8 kJ/mol. This is likely to be caused by the lower decomposition temperature of the intumescent FR additives [6]. The lower decomposition temperature corresponds to the degradation of the intumescent FR particles that ignites first then forms a protective layer that isolates the fuel source from heat and oxygen, thus slowing the combustion [6]. Interestingly, formulations with FR and elastomer have higher E_a than both the original FR formulation and neat PA6. The higher activation energy may be related to the potential for the maleic group grafted onto the PA6 chain to reduce the weak links where the thermal decomposition typically occurs [7]. . Nanocomposite FR formulations containing FR, elastomer, and nanoclay show slightly lower E_a than the FR/elastomer formulations which

could possibly be caused by the low decomposition temperature of the organic modifiers for nanoclay [8].

Table 3.2 summarizes the decomposition temperature at 10% and 50% weight loss and char residue for the selected formulations. The decomposition temperature at both mass loss percentages follows the same trend as the activation energy: 20FR have the lowest value due to the nature of the FR additive, FR/elastomer formulations have the highest decomposition temperature indicating good thermal stability. Compared to formulations with just FR and elastomer, addition of nanoclay slightly decreases the T_d because of the presence of the organic modifier. Neat PA6 has minimal char residue left after heating in nitrogen, FR additive greatly increased the residue mass to 2.9%. While small amounts of elastomer also help to yield higher char residue, the high thermal stability of nanoclay give the nanocomposite samples the highest char yields.

Table 3.2. Decomposition temperature and residue mass of selected FR PA6 formulations. Samples were heated at 10 °C/min in nitrogen.

Temperature and residue	Neat PA6	20FR	20_5	20_10	15_5_2.5	15_5_5
$T_{10\%}$ at 10% mass loss	436.2	416.0	422.6	420.3	421.8	418.9
$T_{50\%}$ at 50% mass loss (°C)	457.4	431.3	463.5	459.7	469.7	467.5
Residue (%)	0	2.9	4.5	2	5.9	6.3

3.4 CONCLUSION

Thermal decomposition of six different PA6 formulations were studied by TGA tests in nitrogen environment. Kinetics of the selected formulations were compared by calculating the activation energy by Ozawa Flynn Wall (FWO) and Lyon's method.

The FWO and Lyon's methods produce comparable results for estimation of the kinetic activation energy. Adding FR slightly decreased the activation energy as well as decomposition temperature. While low concentrations of elastomer is effective in improving activation energy and char residue, samples with higher elastomer loadings have the opposite effect. Although nanoclay does not appear to have a substantial influence on activation energy and decomposition temperatures, it is very effective in improving char residue, which is beneficial for flame retardant application.

In conclusion, the additives (FR, elastomer and nanoclay) do not significantly alter the thermal decomposition process of the PA6. The main mechanism for flame retardant properties are through intumescent char forming which has been discussed in the previous chapter.

3.5 REFERENCES

[1] R.E. Lyon, An integral method of nonisothermal kinetic analysis, Thermochimica Acta 297(1–2) (1997) 117-124.
[2] J.C. Lee, J.H. Koo, O.A. Ezekoye, K. Erickson, Heating rate and nanoparticle loading effects on thermoplastic polyurethane elastomer nanocomposite kinetics, AIAA Paper 4096 (2009).
[3] R.E. Lyon, R.N. Walters, S.I. Stoliarov, Thermal analysis of flammability, Journal of Thermal Analysis and Calorimetry 89(2) (2007) 441-448.
[4] M.J. Starink, The determination of activation energy from linear heating rate experiments: a comparison of the accuracy of isoconversion methods, Thermochimica Acta 404(1–2) (2003) 163-176.
[5] C.D. Doyle, Estimating isothermal life from thermogravimetric data, Journal of Applied Polymer Science 6(24) (1962) 639-642.
[6] H. Wu, M. Krifa, J.H. Koo, Flame retardant polyamide 6/nanoclay/intumescent nanocomposite fibers through electrospinning, Textile Research Journal 84(10) (2014) 1106-1118.
[7] J.D. Menczel, R.B. Prime, Thermal analysis of polymers, fundamentals and applications, John Wiley & Sons (2009).
[8] J.K. Pandey, K. Raghunatha Reddy, A. Pratheep Kumar, R.P. Singh, An overview on the degradability of polymer nanocomposites, Polymer Degradation and Stability 88(2) (2005) 234-250.

Chapter 4: Flame Retardant Nylon 6 Nanocomposite Fibers

Based on the characterization results discussed in Chapter 2, five FR formulations were chosen for the melt spinning process. First a preliminary effort was made to spin fibers at relatively low winding speeds which results in coarse filaments in the 200 μm range. To further reduce the fiber diameter, a high speed fiber winder was used to produce fibers about 30 μm in diameter. Detailed description of processing conditions is provided in the next section. The melt viscosity of the fiber formulations were tested at various temperatures. Fiber structures and morphologies were characterized by XRD, TEM, SEM and optical microscopy. Fiber linear density, mechanical and combustion properties were characterized and are discussed in this chapter.

4.1 EXPERIMENTAL

4.1.1 Melt spinning

The twin screw extrusion is similar to what is described in Chapter 2. Mixtures of the PA6 pellets, FR, elastomers and nanoclay were pre-mixed before extrusion. The screw temperature was set at 240 °C and rotation speed at 100 rpm. The feeding rate for the extruder of was about 35 g/hr for neat PA6.

Because of the limitations of the experimental apparatus, the filament cold-drawing process was not implemented in this study. All fibers were directly collected from the 0.5mm diameter extruder die onto the rotating winder. Two types of fiber winder were used in this study. The first is a Take-Up System by Dynisco Corp. shown in (Figure 4.1 left). The maximum rotating speed of this winder is about 300 rpm (0.47 m/sec). Another fiber winder manufactured by Randcastle was used to achieve higher drawing ratios (Figure 4.1 right). It has a 3.5 inch diameter drum and a rotating speed of 1000 rpm (4.7m/sec) was

used. For both winding process, the extruder feeding rate was kept at 35g/hr for neat nylon 6. All fibers were air cooled during the spinning process as shown in Figure 4.2.

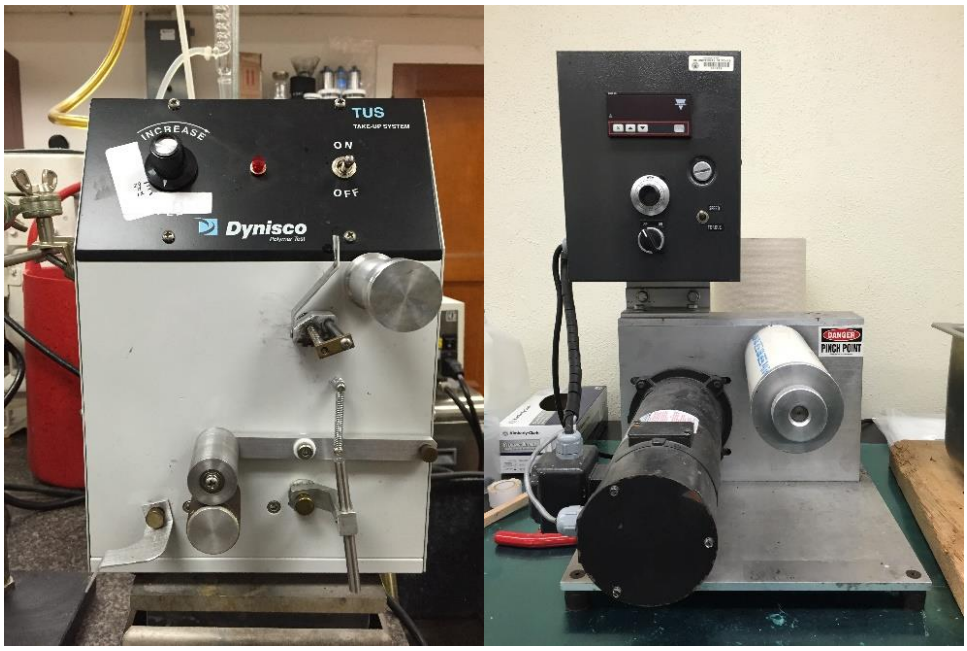

Figure 4.1. Two fiber winders used in this study: Dynisco on the left and Randcastle on the right.

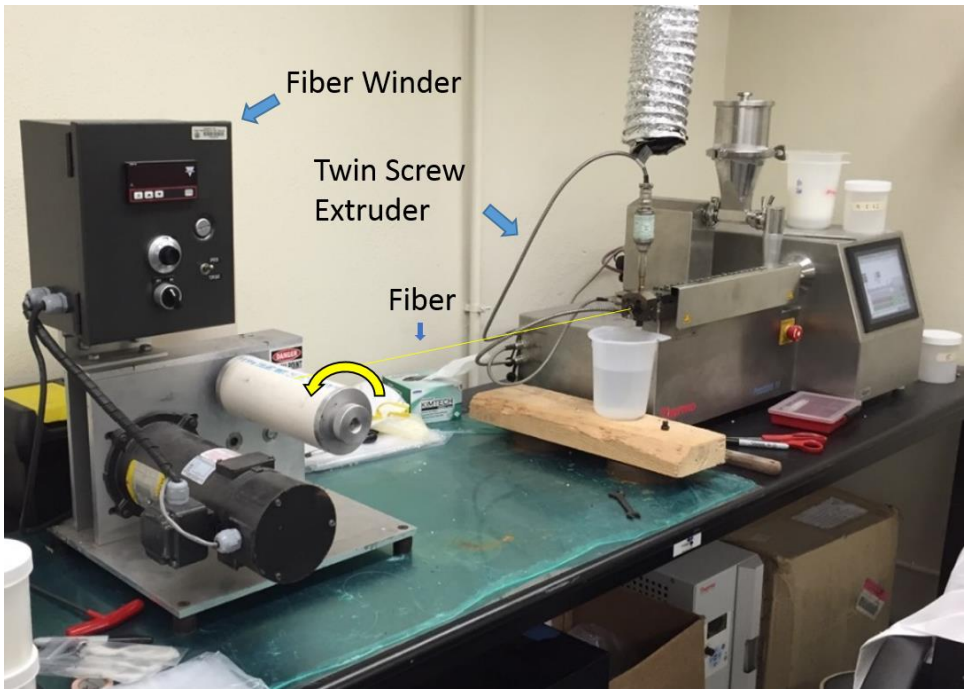

Figure 4.2. The melt spinning setup.

Based on results from the injection molding formulations (Chapter 2). A selection of formulations that have the best property balance were chosen for melt spinning (Table 4.1). The flame retardant loading for nancomposite fibers was kept at 15 w% while the elastomer and nanoclay concentration varied from 0-10 wt% and 0-5 wt% respectively. All experiments for fiber spinning were conducted using the Process 11.

Table 4.1. FR PA6 fiber formulations for fiber spinning.

Sample ID	Label	PA6 (wt%)	Flame retardant (wt%)	Elastomer (wt%)	Nanoclay (wt%)	Fiber winder
1	Neat PA6 D	100	0	0	0	Dynisco
2	20FR D	80	20	0	0	Dynisco
3	15_5_1 D	79	15	5	1	Dynisco
4	15_5_5 D	75	15	5	5	Dynisco
5	Neat PA6 R	100	0	0	0	Randcastle
6	15FR R	85	15	0	0	Randcastle
7	15_5_2.5 R	77.5	15	5	2.5	Randcastle
8	15_5_5 R	75	15	5	5	Randcastle

4.1.2 Ultra-sonication and laser diffraction on FR additives

A pre-screening of the particle morphology of OP1312 FR suggests that the FR powder contains large aggregates with diameter above 30 μm (Figure 4.3.). Such large clusters composed of sub-micron scale FR particulates could negatively affect the fiber spinning process resulting in poor mechanical properties. High magnification SEM images in Figure 4.3 shows that the small FR particulates have ordered geometry and smooth surfaces.

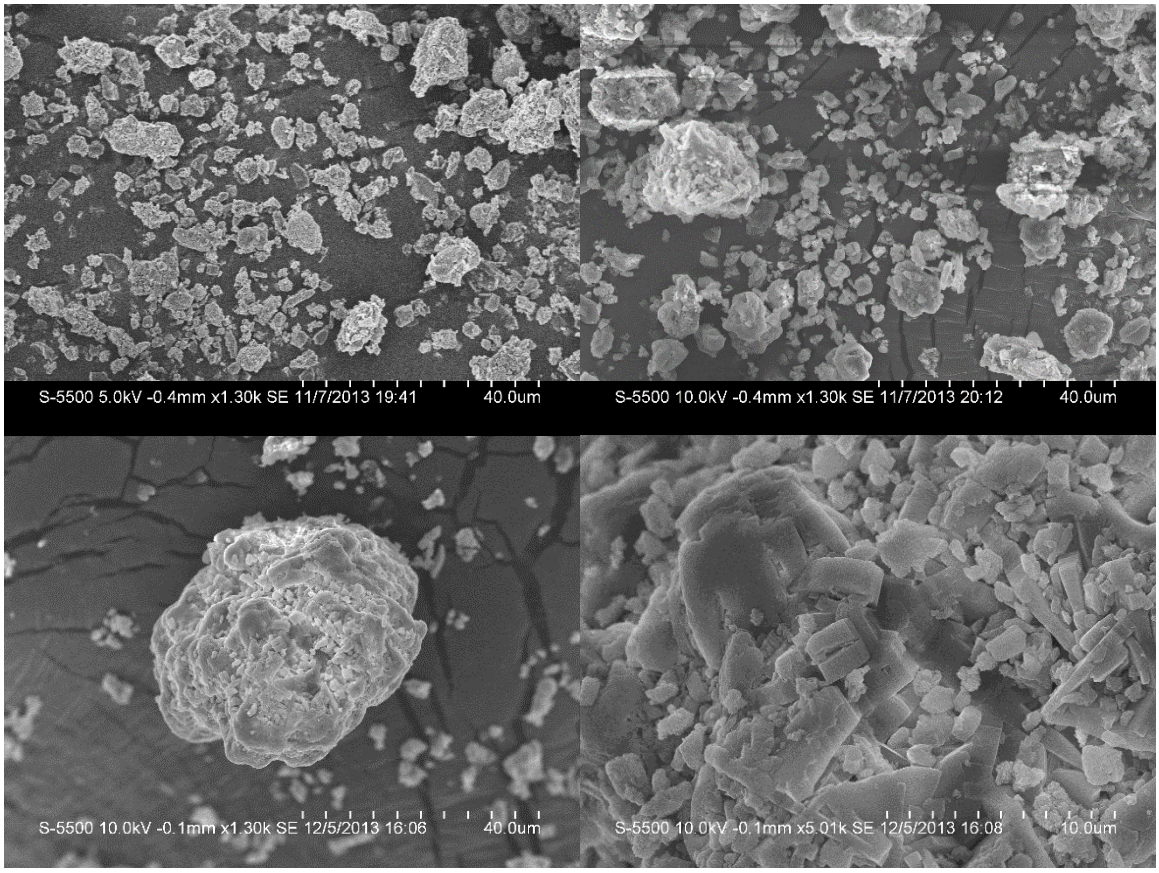

Figure 4.3. SEM images of as-received flame retardant additive.

To reduce the particle size distribution, sonication was used to agitate the FR particles prior to the fiber melt spinning process. A probe type 750 W ultrasonic processor (EW-04711-40) manufactured by Cole-Parmer was used in this study (Figure 4.4). The FR powders were first dispersed in ethanol (~20 wt%) then sonicated for 30 min. Because the intense processing creates large amount of heat, an ice bath was used to cool the solution while pausing the sonication every at 5 min intervals. After sonication, the solution was dried in an oven at 80 °C for at least 4 days to ensure that FR powder are completely dried.

Figure 4.4. Picture of ultrasonic processor and the flame retardant/ethanol solutions after 30min of sonication.

Laser diffraction was used as a tool to examine effect of sonication on the particle size distribution. A Smypatec HELOS laser diffraction system was used for the particle size characterization. FR powders sampled before and after sonication were compared by preparing two dilute solutions of as-received FR and sonicated FR in ethanol. Each sample was tested 5 times to ensure consistency.

4.1.3 Material Characterization

Melt viscosity of the nanocomposite formulations was tested using TA instrument's AR-2000EX rheometer in order to evaluate the impact of the additives on melt spinning performance. A frequency sweep temperature ramp test was performed at a frequency of 1Hz from 230 °C to 260 °C at a heating rate of 10 °C/min. Test specimens were prepared

by compression molding fibers into 1 inch diameter disk. All samples were dried at 80 °C overnight before testing.

4.1.4 Fiber Characterization

SEM and TEM analyses were performed to evaluate fiber morphology and additive dispersion within the fiber structure. A Hitachi S-5500 Scanning-Transmission Electron Microscope (STEM) and FEI Quanta 650 ESEM were used to examine the morphology of melt-spun fibers and char residue. The accelerating voltage of for both SEMs were set at 5 kV for imaging and 30 kV for EDS. Bruker ESPRIT was used for image acquisition and data analysis. Because of surface charging, the nanocomposite samples were coated with gold (Au) and palladium (Pd) before imaging.

For TEM, fibers were first embedded in Epoxy and cured before cutting into ultra-thin sections. Samples were cut along the axial direction as well as in the cross section. Ultra-thin sections were obtained by microtoming using a Leica Ultramicrotome with a diamond knife at room temperature. All the other experimental conditions are identical to what is described in Chapter 2.

Fiber samples were prepared for XRD by aligning a bundle of fibers inside a glass tube and then mounted onto the sample holder. All the other experimental conditions are identical to what is described in Chapter 2.

Optical microscopy was used to characterize fiber diameter. Nikon Elipse LV100 equipped with DS-Fi1 camera was used in this study. Each fiber sample was observed by a 50 X object lens and images were captured and analyzed by the Nikon image processing software NIS-Elements. At least 100 measurements were taken on each specimen and average and standard errors were calculated afterward.

Fiber linear density was measured in accordance with ASTM D1557 single fiber weighing method. To calculate the average and standard errors, a total of 10 specimens were cut into the same length (100 mm) and then weighed with a balance having sensitivity of 0.001 mg. All fibers were conditioned at 21 °C and 65% RH before measurement.

Dynamic Mechanical Analysis (DMA) tests were performed on single melt-spun fibers using a TA Instrument's Q800 equipped with tension clamp. Single fibers were first mounted onto a paper frame with 5 mm gap. After conditioning for 24 hours, the paper frame was transferred onto the test clamp for testing. The fibers were oscillated at 1 Hz while temperature ramps from room temperature to 240 °C.

In addition to DMA, a MTS tensile test machine equipped with 1N load cell was used for fiber samples. The drawing speed was 100 mm/min and gauge length was 100 mm. 10 specimens were tested for each formulation. All tensile test samples were conditioned at 25 °C and 50% RH for at least 48 hours before testing in accordance with ASTM D1776.

4.2 RESULTS AND DISCUSSION

4.2.1 FR Particle Size Analysis

After sonication, many of the FR aggregates are break into smaller particles shown in Figure 4.5. Quantification of the particle size by laser diffraction show a highly significant particle size reduction. Indeed, the as received particles exhibit an apparent bimodal size distribution with the main peak close to 40 μm, and a second relatively smaller peak at about 10 μm (Figure 4.6). After sonication a very distinct difference in particle size distribution can be observed. The peak around 40 um is suppressed significantly and most particles become 3 μm or smaller (Figure 4.7). In both figures, the cut off around 0.6 μm is caused by the limitations of the characterization technique. It is likely that in reality the

intensity would more gradually reach zero as the particles size continue to reduce below 0.6 μm. The shift in the bimodal pattern observed on the distributions is typical in size reduction phenomena of particulate materials [1]. These results indicate that sonication is an effective tool for particle size reduction of OP1312.

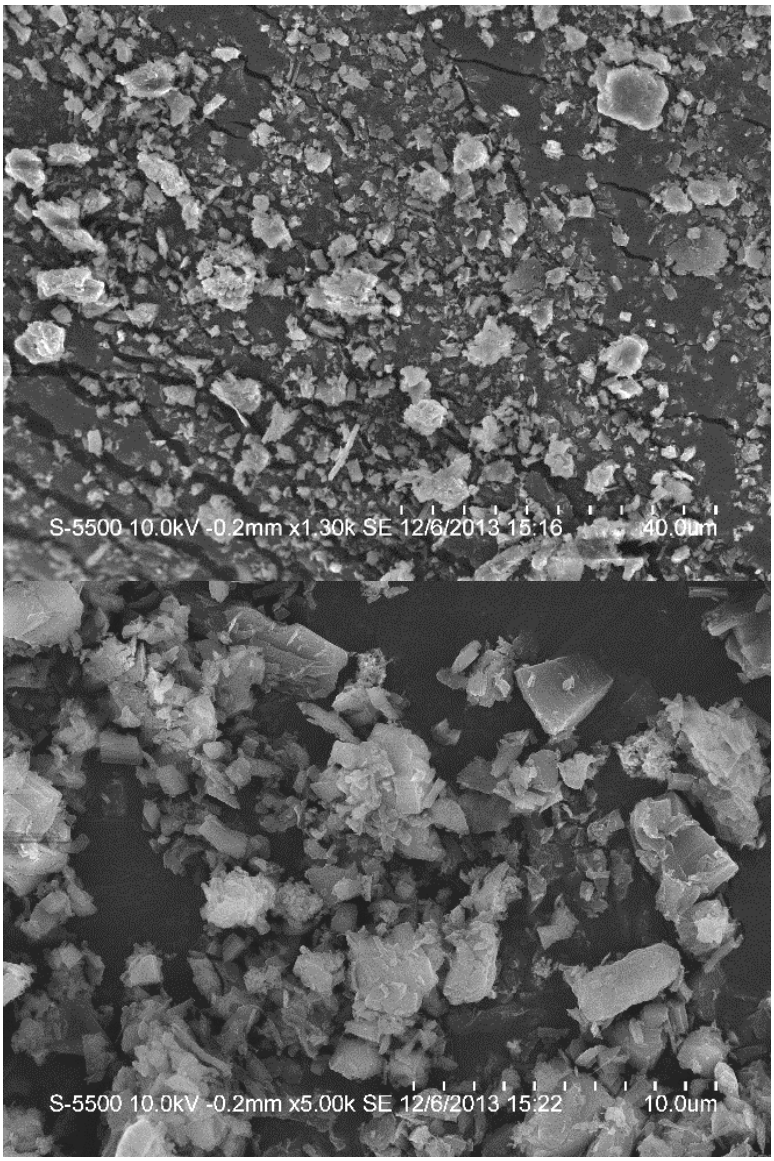

Figure 4.5. SEM image of FR additives after sonication.

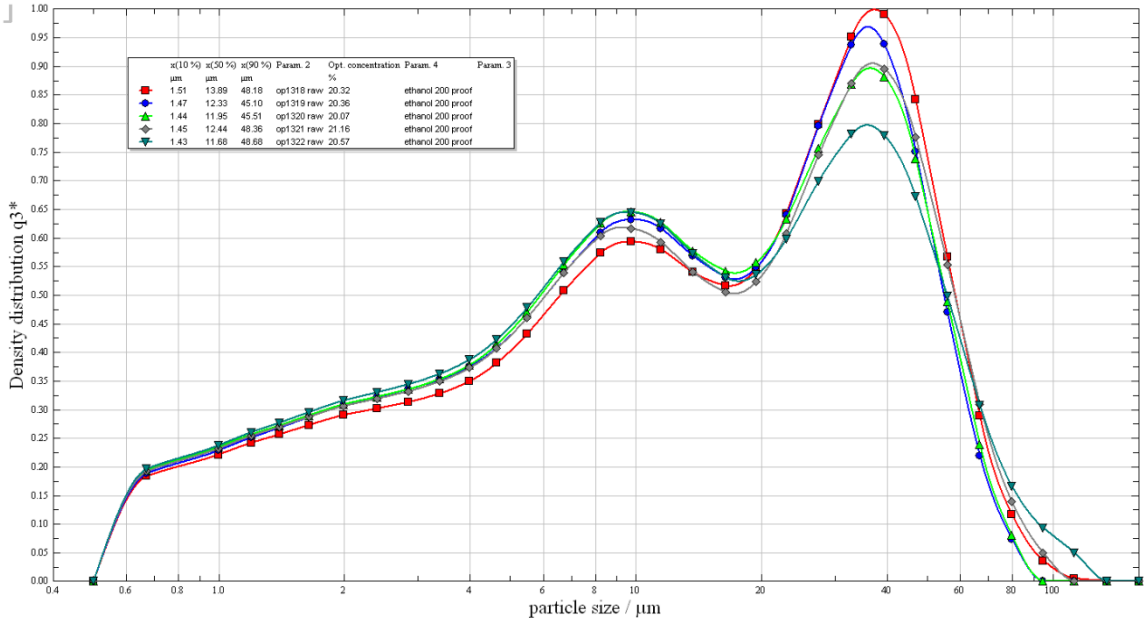

Figure 4.6. Particle size distribution of as-received FR additive.

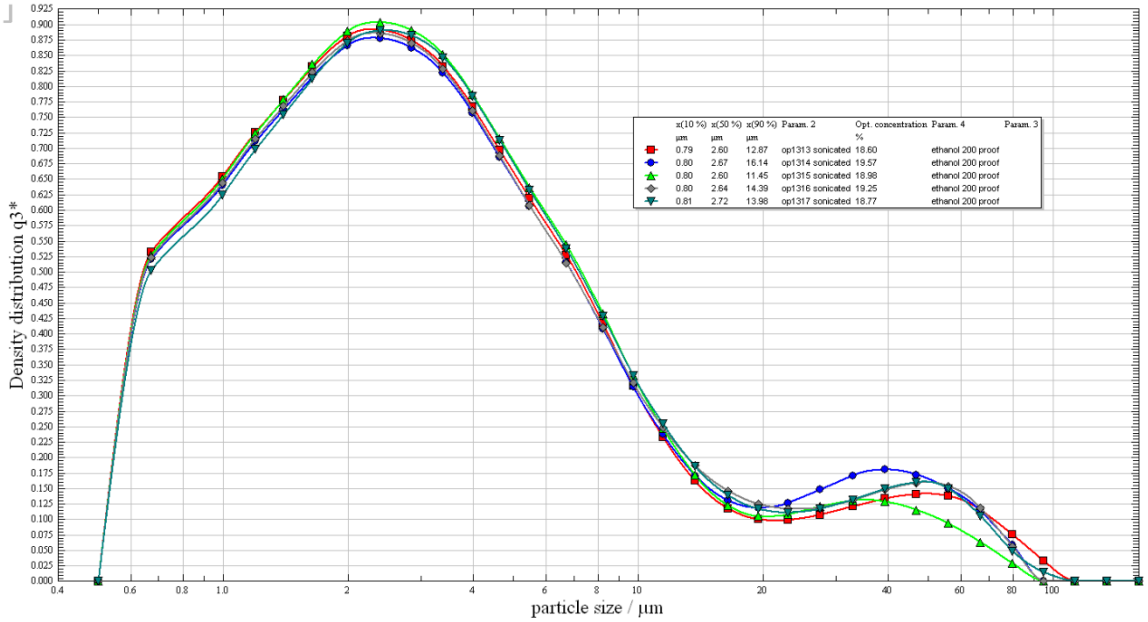

Figure 4.7. Particle size distribution of FR additive after 30min of sonication.

The XRD patterns of the as-received and sonicated FR additives are shown in Figure 4.8 indicate that the FR have at least partial crystalline structures. The distinct peak at 9.1° corresponds to the main component of aluminum diethylphosphinate (AlPi) and the small peak at 14.7° correspond to melamine polyphosphate (MPP). Peaks at 18.6° and 26.3° are convoluted peaks of both AlPi and MPP [2]. The two curves overlap with each other and no peak broadening was observed for the sonicated samples. This suggests that the sonication process has no effect on the crystal size of the FR crystalline domain, it simply separated the small FR particulates apart from the large cluster.

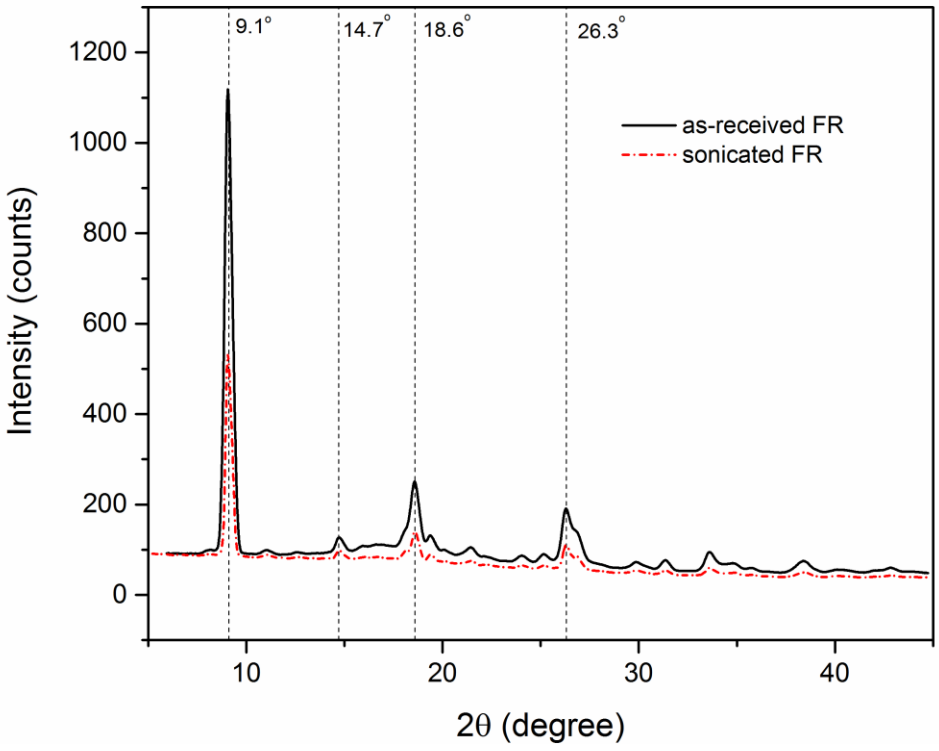

Figure 4.8. XRD patterns of FR additives before and after sonication.

4.2.2 Melt Viscosity for Fiber Spinning

Melt viscosity of the melt spun fibers (collected by low speed Dynisco fiber winder) at temperatures between 230 °C to 260 °C were tested. By using an empirical relationship called Cox-Merz rule (Equation 6.1), the complex viscosity from dynamic mechanical analysis is an effective way to estimate the steady shear viscosity for melt thermoplastics, which can be used as a reference for melt spinning [3].

$$|\eta^*(\omega)| = \eta(\dot{\gamma})|_{\dot{\gamma}=\omega} \quad (6.1.)$$

For polymeric composite materials containing one or more additives, the melt rheology can be affected by the size, shape, concentration as well as surface functionality of the additives [4]. The complex melt viscosity of molded neat PA6 and FR PA6 formulations are plotted in Figure 4.9. Neat PA6 has lowest melt viscosity compared to its composite formulations. All formulations start with slightly higher viscosity at temperatures between 230 °C to 235 °C. The viscosity becomes constant after heating above 235 °C. Samples with 20 wt% FR exhibited a significant increase in viscosity compared to the neat PA6. Sample 15_5_1 D has the highest viscosity which is possibly due to the interaction between maleic anhydride and amine groups of PA6 [5]. Because of such significant increase in viscosity, samples with higher elastomer loadings are not suitable for fiber spinning due to poor spinnability. When comparing 15_5_1 D and 15_5_5 D, the higher clay loading yielded more than a 40% decrease in melt viscosity. Two possible mechanisms to explain this result are slippage of exfoliated nanoclay within PA6 and degradation of PA6 caused by the presence of nanoclay [4]. Therefore, since the viscosity of all formulations become stable after 235 °C, it should be appropriate to use 240 °C for the fiber spinning process.

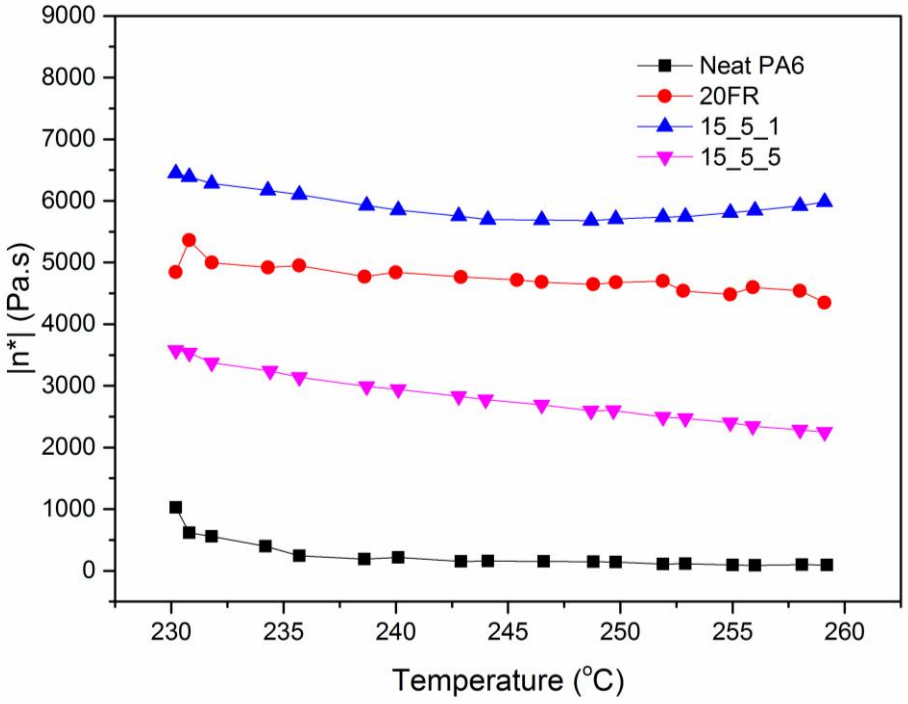

Figure 4.9. Melt Viscosity of FR PA6 formulations (fibers collected from Dynisco).

4.2.3 Fiber Morphology

Figure 4.10 shows the SEM images of neat PA6 and its FR composite fibers processed using the low speed winder from Dynisco. Neat PA6 fibers (Figure 4.10 (a)) have very smooth surface with average diameter around 100 μm whereas fibers with rougher surfaces and larger diameter were observed for the other 3 samples containing additives (Figure 4.10 (c-d)). Protruding particles of FR appeared evenly distributed throughout the observed fiber surface. EDX mapping results (Figure 4.11) confirmed that these particles contained aluminum and phosphorus elements and are indeed from the aluminum phosphinate-based flame retardants. Moreover, for formulations containing nanoclay, distinct peaks of silicon suggest the clay platelets are dispersed throughout the fiber surface (Figure 4.11).

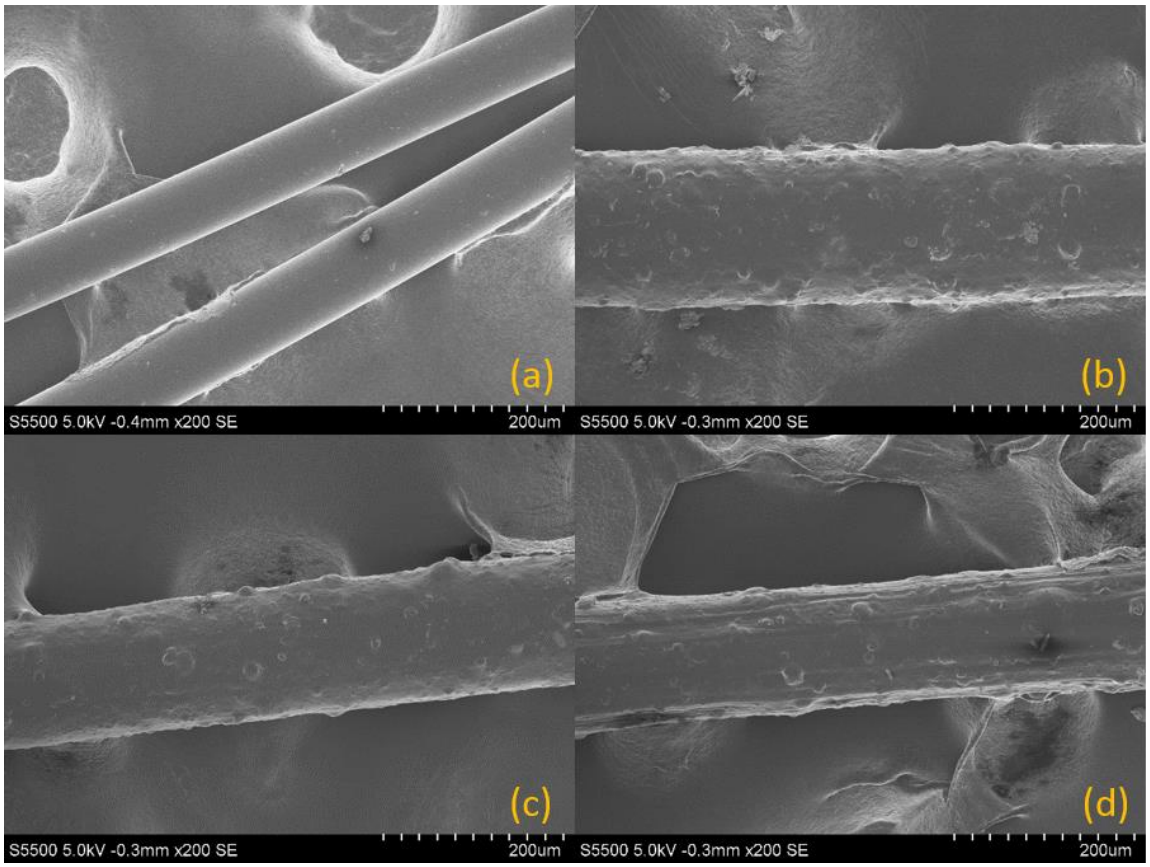

Figure 4.10. SEM images of PA6 and its nanocomposite fibers: (a) neat PA6 D; (b) 20FR D; (c) 15_5_1 D; (d) 15_5_5 D.

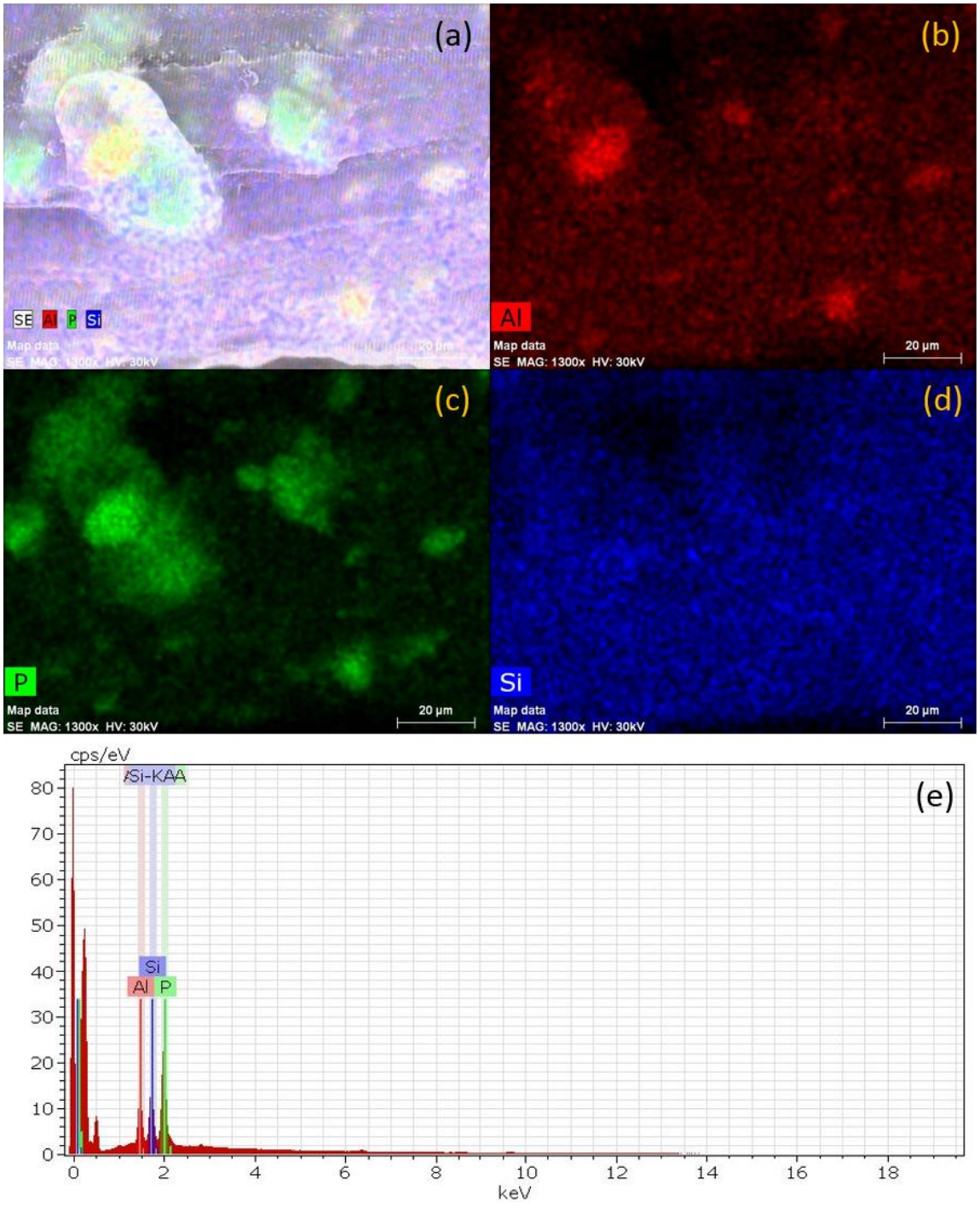

Figure 4.11. EDS mapping and spectrum of 15_5_5 D fiber.

As mentioned in the methods section, a higher RPM winder (Randcastle) was needed to ensure higher drawing of the filaments into a useable textile fiber range. The diameter and linear density of those fibers were quantified by using optical microscope and gravimetric measurement according to ASTM1557, respectively. Table 4.2 summarizes the average fiber diameter and linear density. All four formulations have very similar diameters and linear density. The relatively larger standard errors for composite fibers with additives suggest that they may be less uniform than neat PA6 fibers. This observation is confirmed in SEM images shown in Figure 4.12. Diameter unevenness and protrusions due to FR particles can clearly be seen on the filaments depicted in Figure 4.12-b, c, and d. It appears that further reduction of FR particle size may be necessary to minimize those protrusions and achieve a more even fiber surface.

Table 4.2. Fiber dimensional analysis results (Randcastle, the high RPM winder).

Sample	**Diameter (um)**	**Denier**
Neat PA6 R	34.0±0.3	10.62±0.34
15FR R	30.6±0.8	10.97±0.47
15_5_2.5 R	35.8±0.7	10.94±0.29
15_5_5 R	33.2±0.8	11.19±0.56

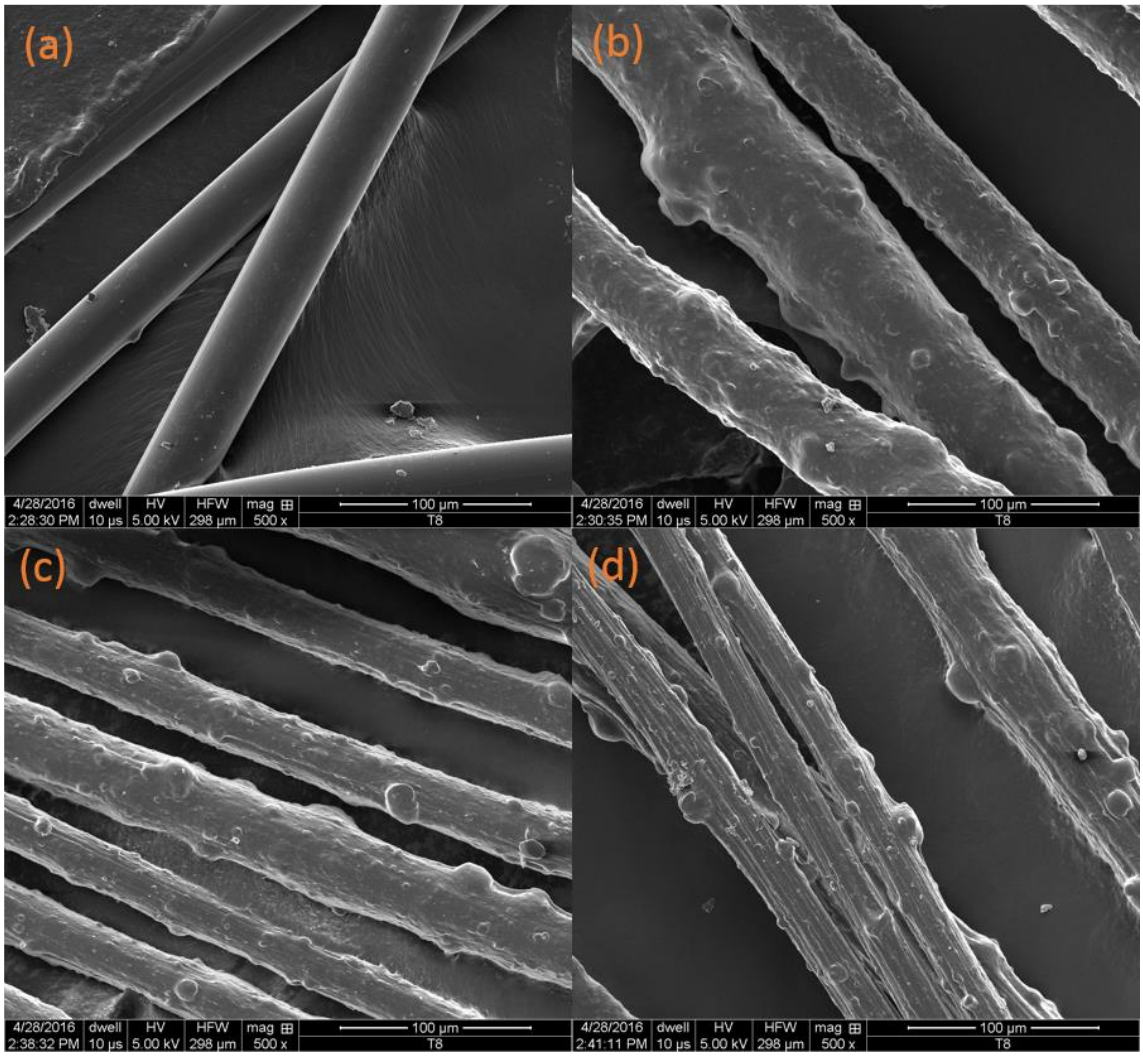

Figure 4.12. SEM images of different FR PA6 fibers: (a): neat PA6 R; (b):15FR R; (c): 15_5_2.5 R; (d):15_5_5 R.

4.2.4 XRD

The XRD pattern of melt spun neat PA6 fiber is plotted in Figure 4.13 in comparison with the injection molded PA6. Both forms of the neat PA6 exhibit γ phase peaks at 10.8° and 21.3°. This suggests that the melt spinning process in this study also favors crystallization of the γ phase possibly due to slow cooling of the fiber in air.

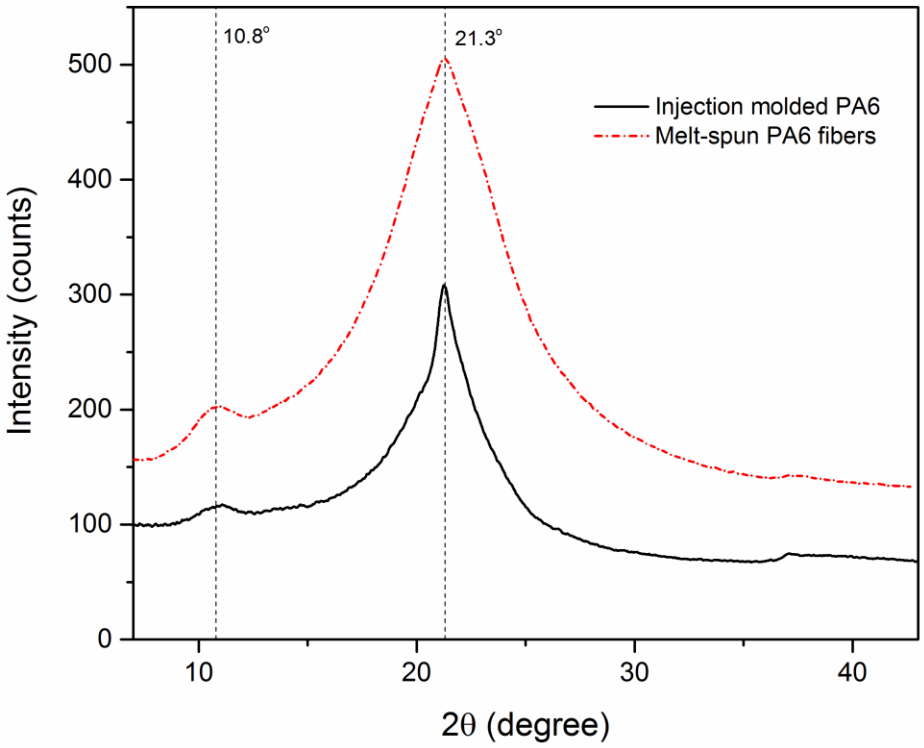

Figure 4.13. XRD patterns of injection molded PA6 specimen (solid black line) and melt spun PA6 R fibers (red dotted line).

A comparison of 2D wide-angle X-ray diffraction patterns of both injection molded and melt-spun PA6 fibers is given in Figure 4.14. It is clear that the fiber sample have a higher degree of alignment of the crystalline lamellas. Such alignment of crystal regions within PA6 is beneficial for achieving high tensile strength and modulus.

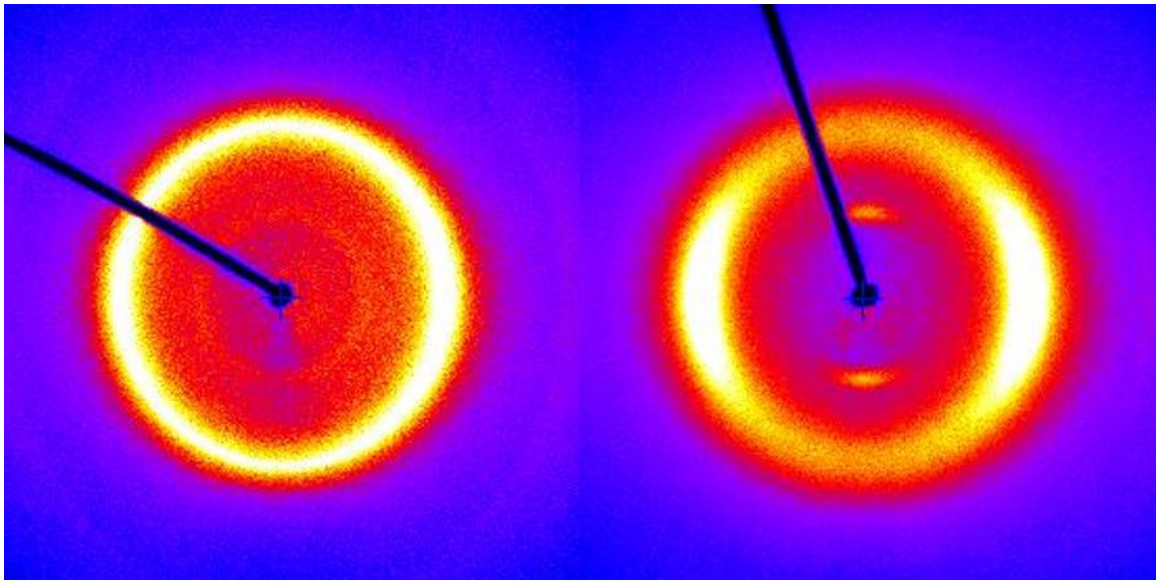

Figure 4.14. Two dimensional (2D) wide-angle X-ray diffraction patterns of injection molded PA6 specimen (left) and melt spun PA6 R fibers (right).

A similar phenomenon is observed for the FR fibers as well. Figure 4.15 shows the 2D WAXD patterns of the PA6/FR/elastomer/nanoclay formulation processed by both injection molding and melt spinning. Except for the fact that both samples have sharp rings attributed to the FR additive and broad peak due to the reflection from PA6, the fiber sample exhibits a clear preference in crystal orientation.

Figure 4.16 shows the XRD patterns of the formulation 15_5_5 in both bulk and fiber form. Both samples shares very similar diffraction pattern and none of them have the basal reflection from the nanoclay. The absence of nanoclay reflection peaks indicate high level of exfoliation of the nanoclay platelets in both injection molded and fiber samples. This observation is confirmed by the TEM images of the fiber samples which will be discussed in the next section.

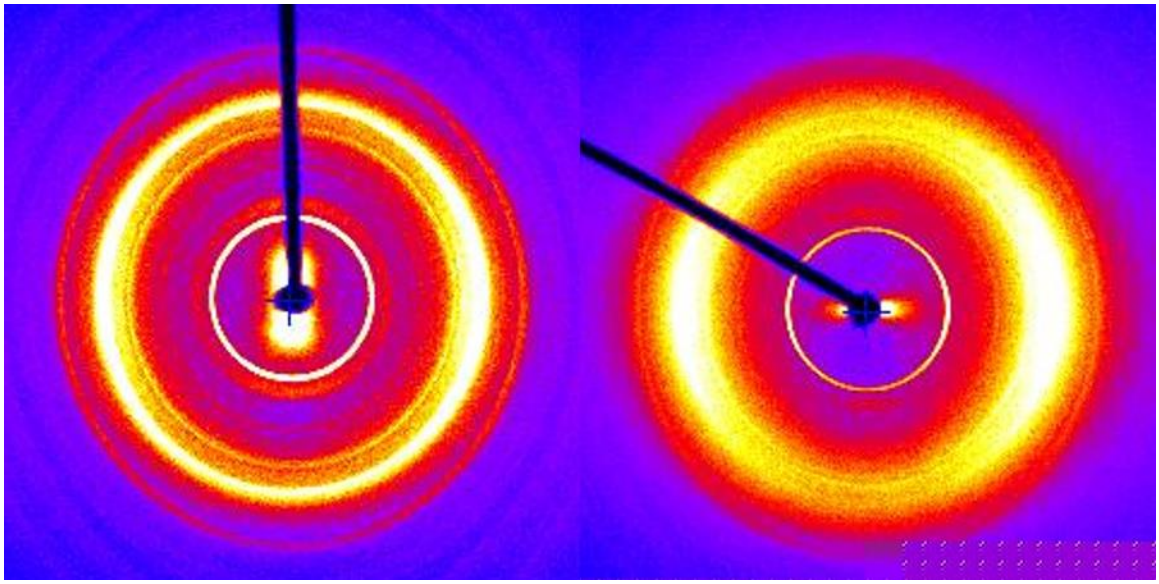

Figure 4.15. Two dimensional (2D) wide-angle X-ray diffraction patterns of FR PA6 formulation 15_5_5 containing 15 wt% of FR, 5 wt% of elastomer and 5 wt% of nanoclay: Injection molded PA6 specimen on the left and melt spun R fibers on the right.

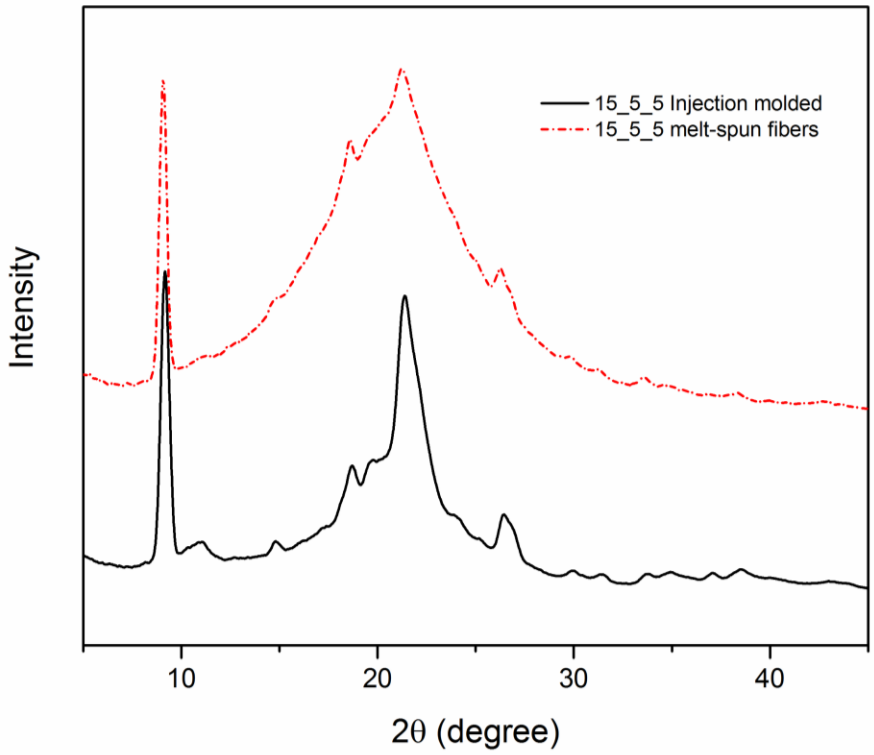

Figure 4.16. XRD patterns of 15_5_5 in both bulk and fiber form.

4.2.5 Microstructures of Melt Spun Fibers

To further evaluate the morphology and dispersion of the nano-additives, fibers spun from formulations 15_5_1 D and 15_5_5 D were cut into ultrathin section and investigated by TEM. Each sample was cut in both axial and cross section directions to obtain a comprehensive understanding about the material. Figure 4.17 and Figure 4.18 show the cross section and axial section of sample 15_5_1 D, respectively. At 1 wt% loading, nanoclay platelets are sparsely dispersed within in the polymer matrix. High magnification images suggest that with the exception of few aggregates, most nanoclay platelets are either exfoliated or intercalated. At lower magnification, even distribution of FR particles with various sizes can be observed. Similar results apply to sample 15_5_5 D with 15 wt% FR, 5 wt% elastomer and 5 wt% nanoclay (Figure 4.19 and Figure 4.20). The

only notable difference is higher density of nanoclay platelets throughout the PA6 matrix. In both cases, nanoclay observed on images taken in the fiber axial direction appear well aligned along the fiber axis (Figure 4.18 and Figure 4.20).

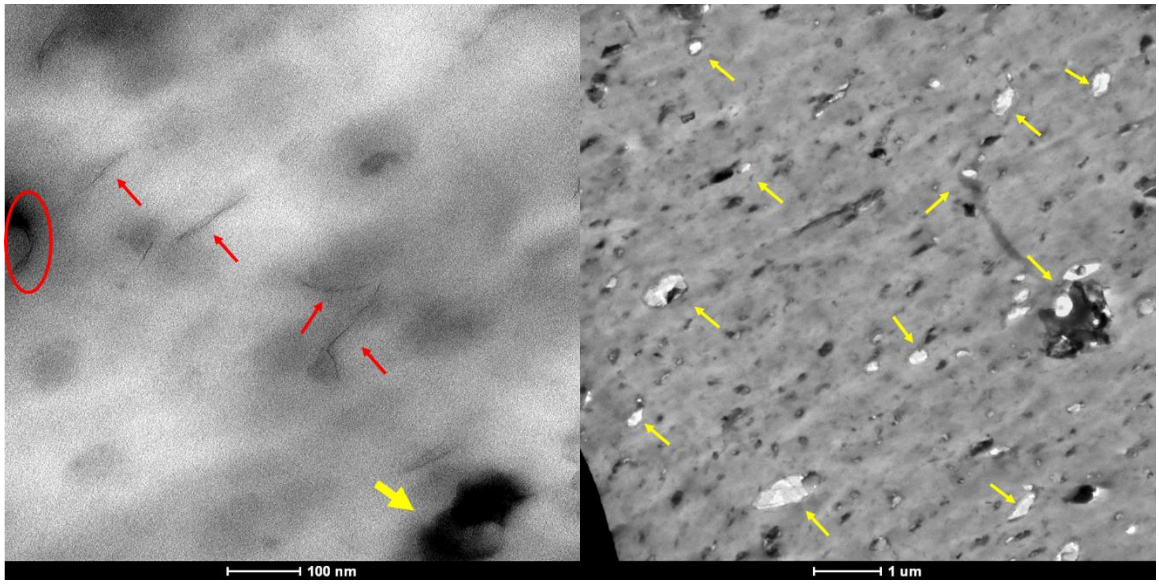

Figure 4.17. TEM of 15_5_1 D fiber cross section (red circle indicate nanoclay aggregates; red arrow indicate intercalated or exfoliated nanoclay; yellow arrow indicate flame retardant particles.)

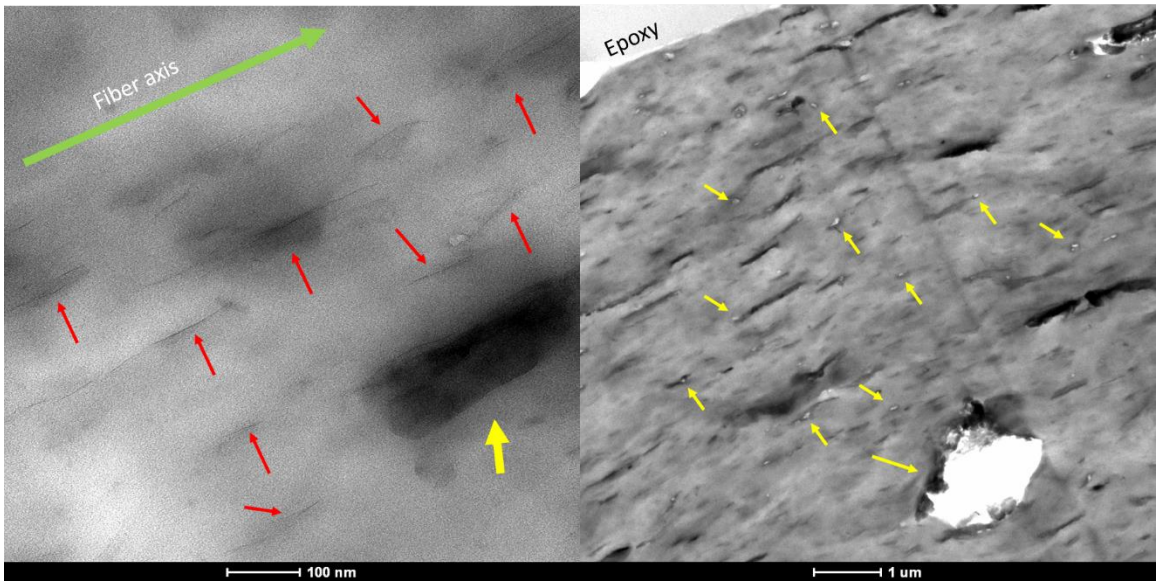

Figure 4.18. TEM of 15_5_1 D fiber in the axial direction (green arrow indicate fiber axial direction; red circle indicate nanoclay aggregates; red arrow indicate intercalated or exfoliated nanoclay; yellow arrow indicate flame retardant particles.)

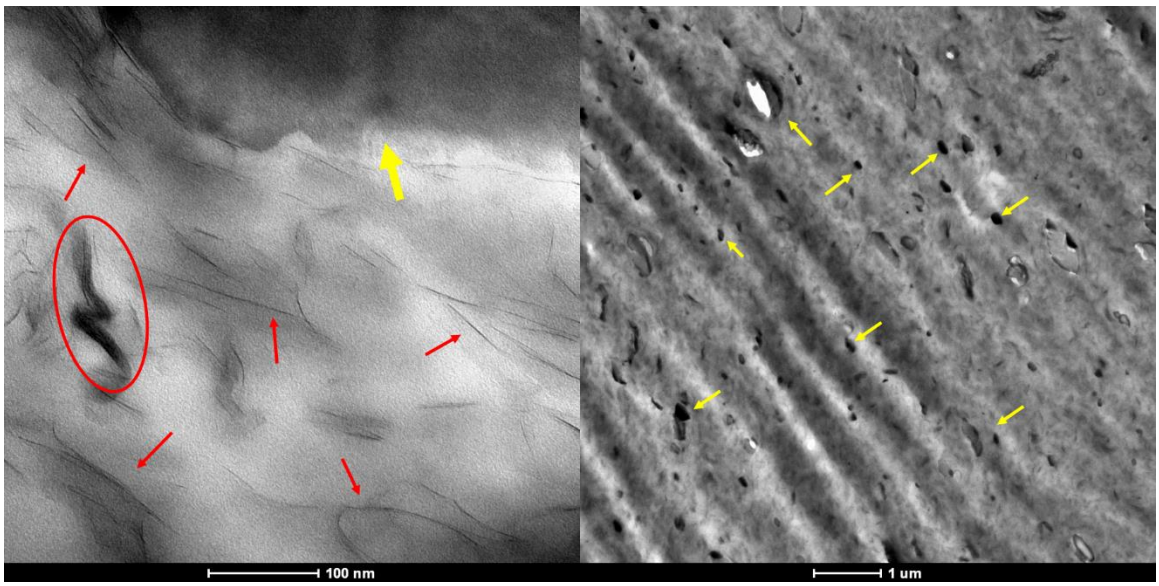

Figure 4.19. TEM of 15_5_5 D fiber cross section (red circle indicate nanoclay aggregates; red arrow indicate intercalated or exfoliated nanoclay; yellow arrow indicate flame retardant particles.)

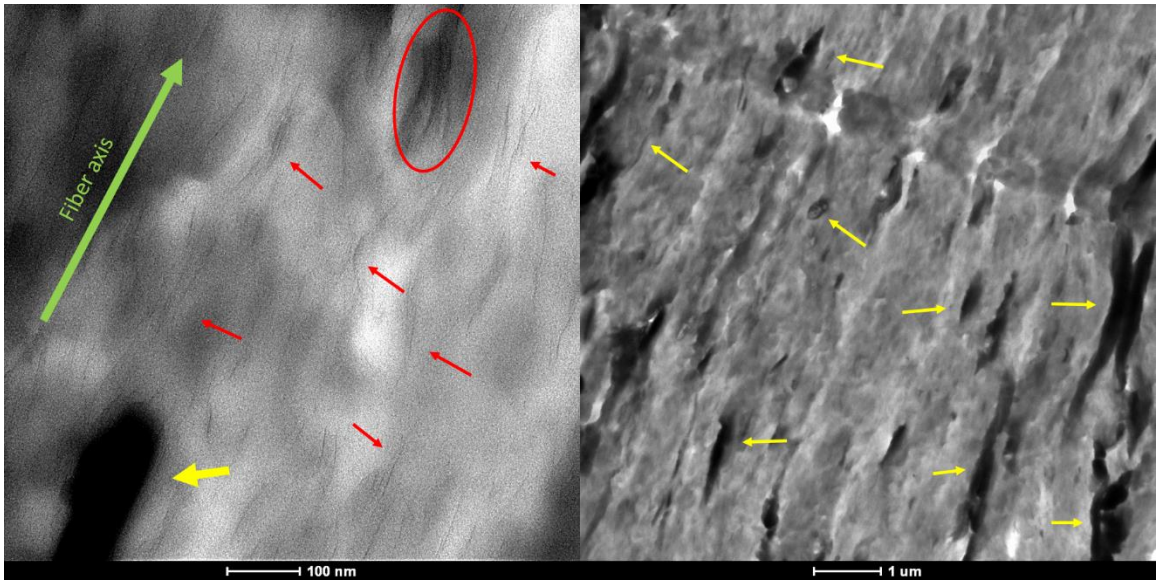

Figure 4.20. TEM of 15_5_5 D fiber in the axial direction (green arrow indicate fiber axial direction; red circle indicate nanoclay aggregates; red arrow indicate intercalated or exfoliated nanoclay; yellow arrow indicate flame retardant particles.)

As discussed in Chapter 2, TEM is a powerful tool to characterize the morphology of polymer blends both qualitatively and quantitatively. This is usually done by staining one of the phases with a heavy element to obtain enhanced contrast [6]. TEM images of stained sample 15_5_5 D are displayed in Figure 4.21. The uniformly distributed bright oval-shaped spots are elastomer particles embedded in the stained PA6. The elongated shape of the elastomer particles could be caused by the presence of nanoclay [7]. The cross section images indicate that the average length of the elastomer particles is about 100 nm. Axial section images clearly show that the elastomer particles are elongated significantly along the fiber axis. The clay platelets only exist in the nylon phase and did not penetrate into the elastomer phase [7].

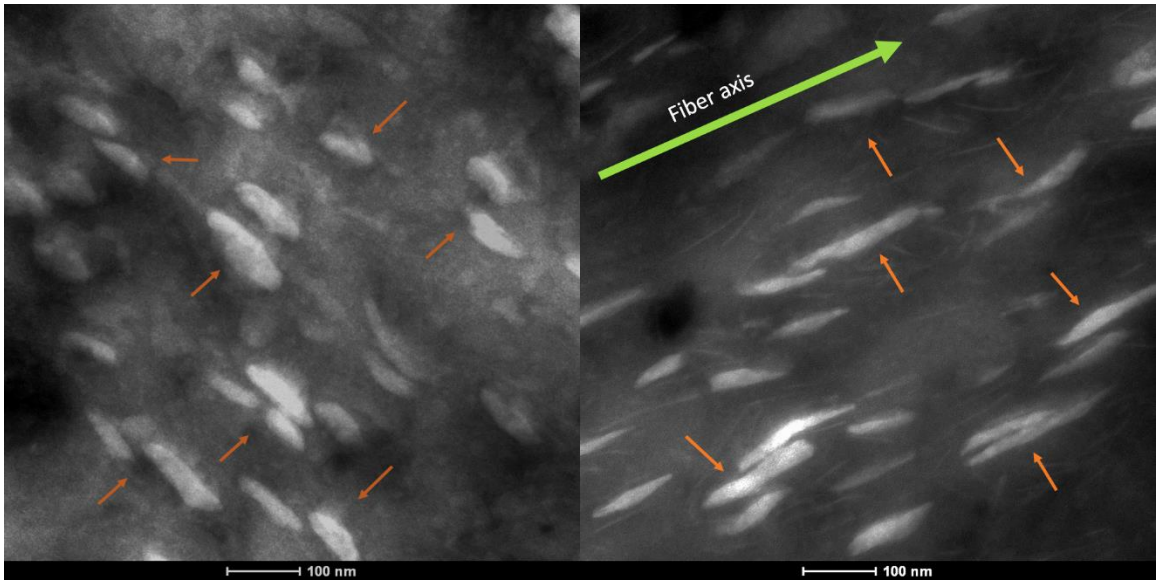

Figure 4.21. TEM of stained 15_5_5 D fiber taken in cross section direction (left) and fiber axial direction (right, green arrow indicate fiber axial direction; orange arrows indicate elastomer particles.)

4.2.6 Dynamical Mechanical Analysis (DMA)

The temperature dependence of storage and loss modulus for single FR PA6 fibers are plotted in Figure 4.22. One obvious relaxation process is observed for all samples starting at around 50 °C. It has been reported that the α relaxation or glass transition of nylon 6 occurs in two distinct steps. The first step takes place at around -50 °C and is attributed to the increased mobility of short chain segments and the section step starts at 70 °C [8, 9]. Therefore, the relaxation observed here should be regarded as the second step of glass transition which represents the micro-Brownian motions of long chain segments in the amorphous regions of the nylon 6. The Neat PA6 fiber have the highest value in both storage and loss modulus at temperatures below around 110 °C and the gap become smaller as the temperature goes up. The lower storage and loss modulus of the FR fibers could be caused by the presence of the large FR clusters shown in the SEM images. The relaxation peak temperatures obtained from the loss modulus and tan δ curves are summarized in

Table 4.3. The peak temperature of the loss modulus for neat PA6 fiber is slightly higher than the FR formulations while the 15_5_2.5 R fiber has the lowest peak temperature in loss modulus.

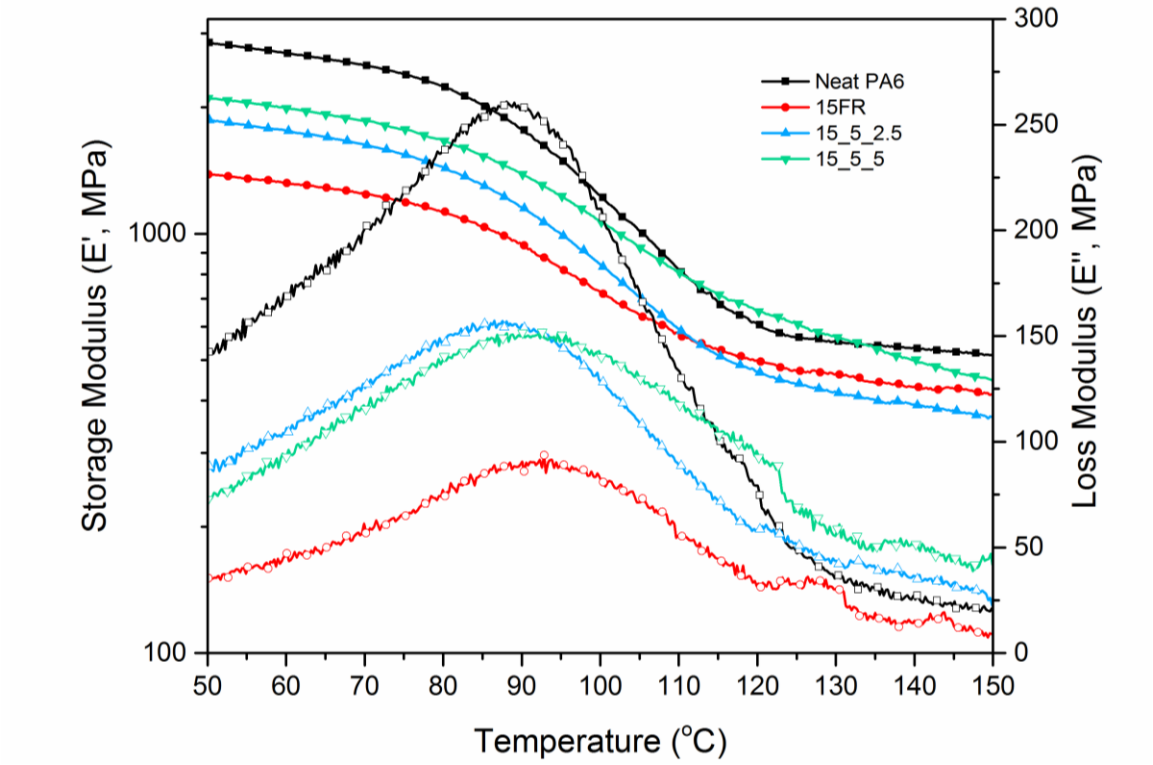

Figure 4.22. Temperature dependence of the storage and loss modulus for single FR PA6 nanocomposite fibers (Randcastle).

Table 4.3. DMA maximum relaxation temperature of the FR PA6 fibers (Randcastle).

Sample	**Loss modulus peak temperature (°C)**	**Tan δ peak temperature (°C)**
Neat PA6	93.3	102.6
15FR	92.8	102.6
15_5_2.5	86.5	105.6
15_5_5	92.6	116.9

The tan δ curve of the four fiber samples are shown in Figure 4.23. The α relaxation peak for neat PA6 fiber is 102.6 °C which is higher than values reported by other researchers [8, 9]. The increased peak temperature could be caused by higher heating rate in this experiment. Note that polymers with high crystallinity can also cause the Tg shift to higher temperature [3]. The peak tan temperature for the 15_5_5 R is 14 °C higher than the neat PA6 fiber. The peak tan δ value follows the same trend as the loss modulus. The neat PA6 fiber have highest peak tan δ which indicates that the neat fibers are less elastic than the FR fibers.

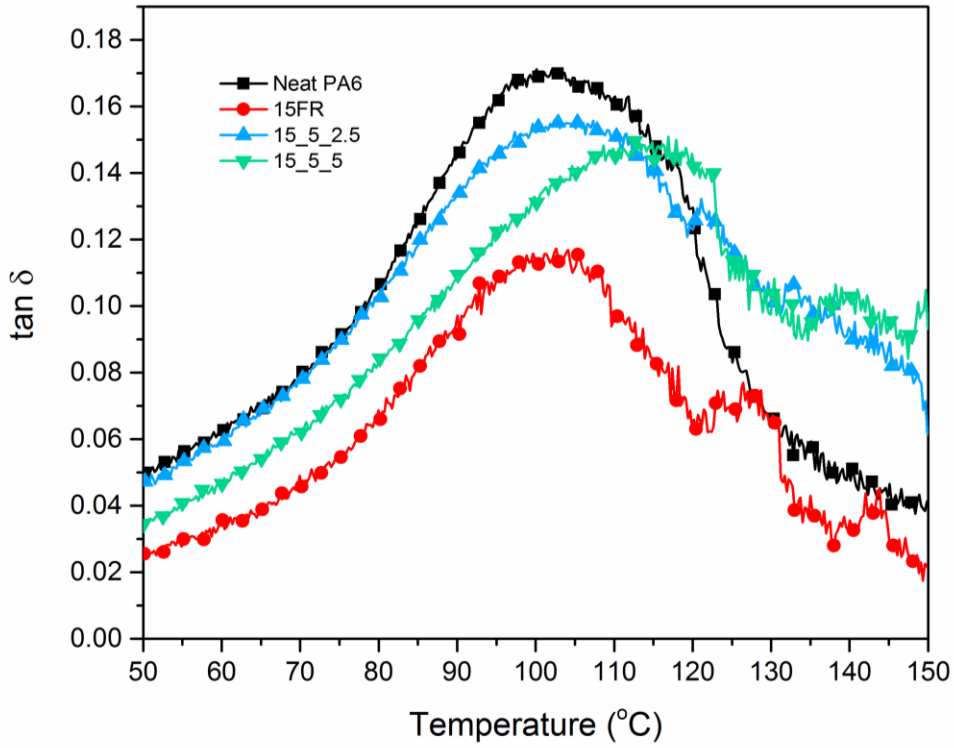

Figure 4.23. Temperature dependence of tan δ of FR PA6 fibers.

4.2.7 Single Fiber Tensile Properties

Tensile properties of single FR PA6 fibers collected at 1000 rpm using the Randcastle winder were tested on a MTS machine according to ASTM D3822. Typical stress-strain curves are plotted in Figure 4.24. Fiber tenacity and elongation at break are summarized in Table 4.4. Because the fibers have been drawn significantly after extrusion, there is no necking stage for all the fiber formulations. The disappearance of the necking stage typically observed in the injection molded samples suggests that the crystalline regions are well aligned inside the fiber. Among all the formulations, neat PA6 fibers have the highest tensile strength and elongation at break. The major impact on the tensile properties comes from the flame retardant particles, 15 wt% of FR have 50% lower elongation break than the neat PA6. One of the formulations containing elastomer and nanoclay (15_5_2.5 R) exhibits a significant increase in both tensile strength and elongation at break compared to the 15FR fiber. However higher nanoclay loading resulted in further significant degradation in both tensile strength and ductility. These results are consistent across all specimens tested for each formulation.

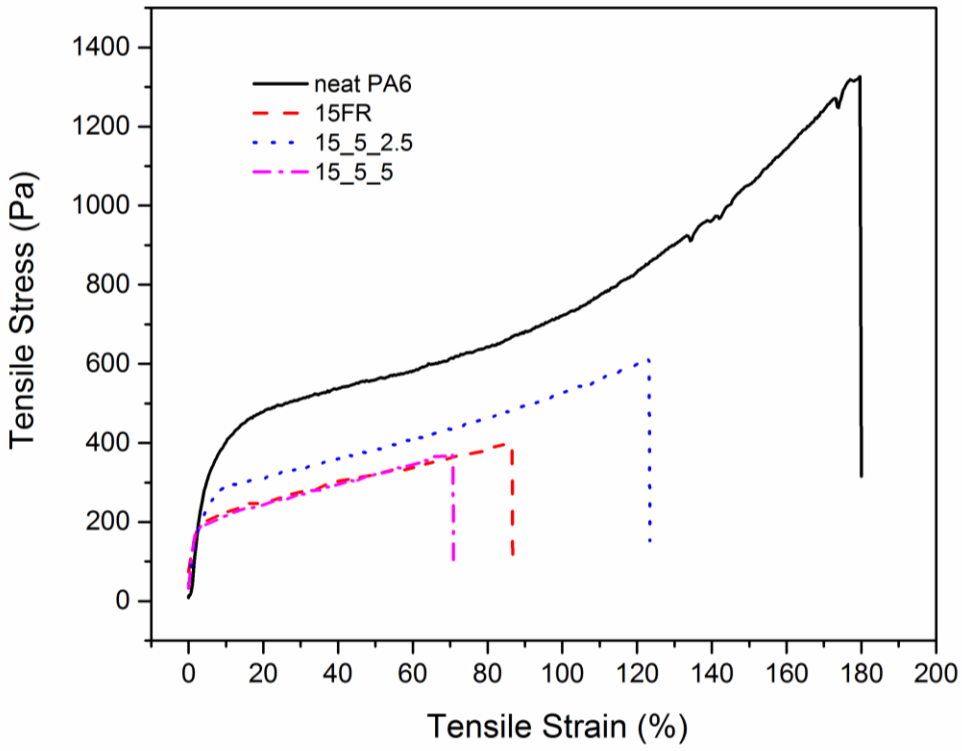

Figure 4.24. Typical stress strain curve of single FR PA6 fibers (Randcastle).

Table 4.4. Tensile properties of FR PA6 fibers (Randcastle).

Sample	Tenacity (g/denier)	Elongation at break (%)
neat	1.52±0.08	167.35±6.85
15FR	0.47±0.06	88.45±15.00
15_5_2.5	0.68±0.02	127.33±4.58
15_5_5	0.40±0.02	69.58±5.23

4.2.8 Fiber Flammability

4.2.8.1 Preliminary Coarse Fibers

Flammability of FR fiber formulations were evaluated by small scale MCC tests. Heat release rate (HRR) vs. Temperature curves are plotted in Figure 4.25 for the initial set of fiber samples processed using low RPM winder. The corresponding MCC parametric results are summarized in Table 4.5. Neat nylon 6 fibers have a peak heat release rate (PHRR) around 870 W/g. The PHRR is reduced by more than 30% for all other three FR fiber samples. The onset degradation temperature is lower than the neat control as expected based on the discussion in Chapter 2. The heat release capacity (HRC) of melt spun fibers are shown in Figure 4.26. Neat PA6 fibers have a HRC of 620.6 J/g-K. After adding 20 wt% of FR, the HRC dropped by 31% to 426.8 J/g-K. At 15 wt% FR loading, both formulations with 3 different additives including FR, elastomer and nanoclay show even lower HRC than the formulation with just FR.

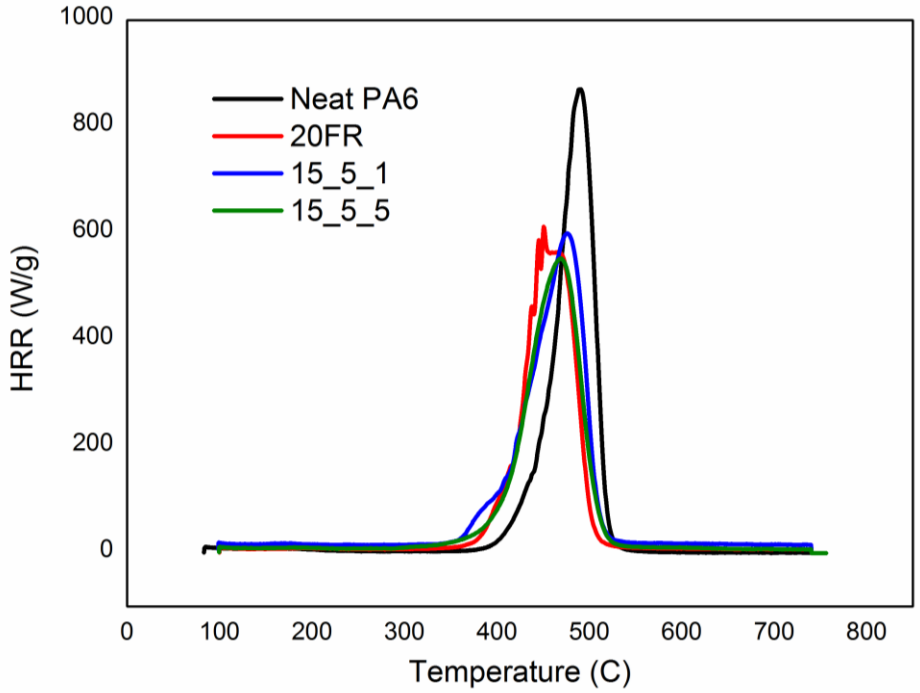

Figure 4.25. MCC curves of FR PA6 fibers (Dynisco).

Table 4.5. FR PA6 fiber formulations (Dynisco).

Sample	**Heat Release Capacity (J/g-K)**	**Peak Heat Release Rate (W/g)**	**Total Heat Release (kJ/g)**	**Peak Temperature (°C)**
Neat PA6	620.6±4.8	870.8±6.7	30.5±0.1	488.2±0.5
20FR	426.8±6.6	596.7±9.0	27.1±0.1	451.6±1.5
15_5_1	411.2±4.3	578.3±6.1	28.4±0.1	475.5±0.6
15_5_5	395.4±2.1	549.9±4.5	27.7±0.1	470.3±0.6

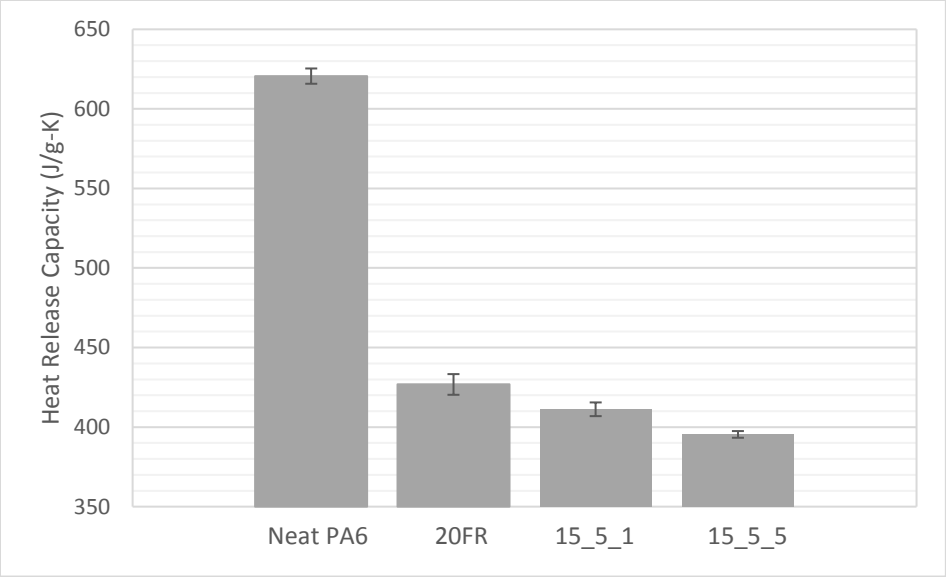

Figure 4.26. Heat Release Capacity of FR PA6 fibers (Dynisco).

The principle degradation products of neat nylon 6 is volatile cyclic caprolactam [10, 11]; therefore, minimal residues are left after heating the sample to 750 °C (Figure 4.27 left). In contrast, all samples containing FRs have significantly higher char yield. In addition, what's rather interesting is that the posttest char of sample 15_5_5 D retained its fiber morphology (Figure 4.27 right), which could be related to the non-drip nature of the FR system. Figure 4.28 shows the char morphology of sample 15_5_5 D. High magnification images shows that the char is formed throughout the fiber body. Air bubbles forming inside the fiber consolidate the char layer composed of intumescent and nanoclay platelets. This observation indicates that the nanocomposite fibers have overcome the dripping problem of neat PA6.

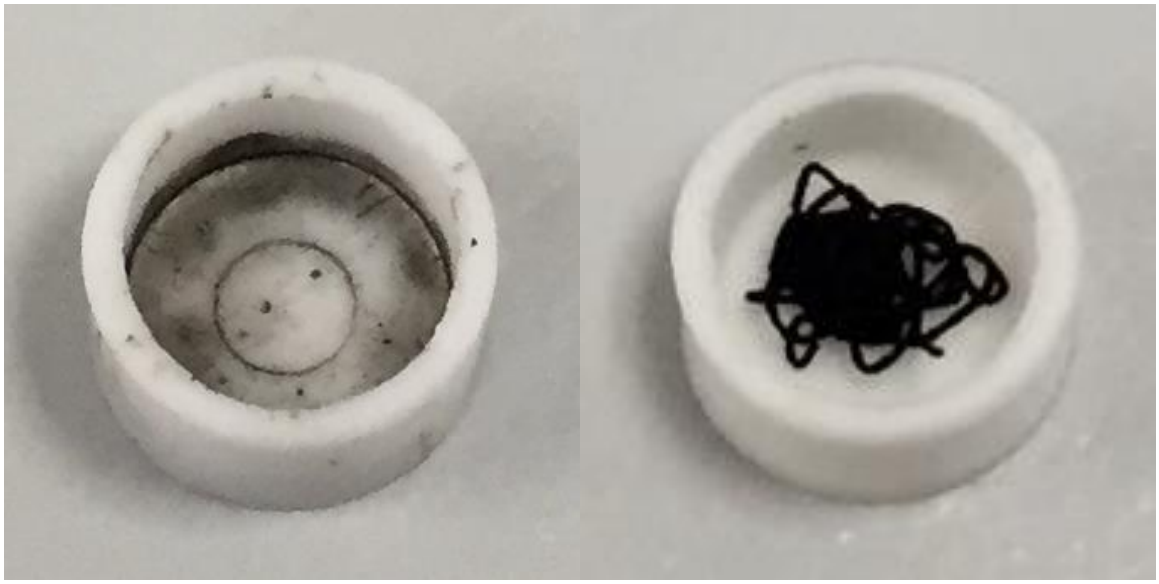

Figure 4.27. Post MCC test specimen of FR PA6 nanocomposites (left: neat PA6 D; right: 15_5_5 D).

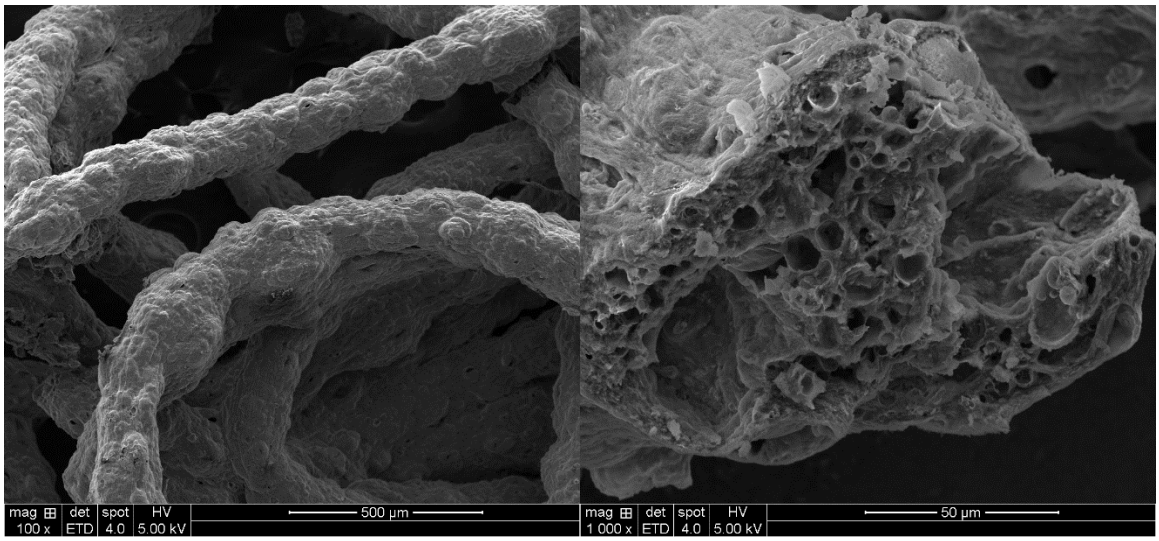

Figure 4.28. Char morphology of 15_5_5 D fiber.

4.2.8.2 High Draft Fibers (30 um)

The typical heat release rate versus temperature curves of the second set of fiber samples (fine diameter) are shown in Figure 4.29. Table 4.6 summarized the MCC

parameters of the formulations. The results obtained on the fine fibers show an analogous trends to those discussed above. Neat nylon 6 has a PHRR of 973.6 W/g at 488.2 °C. After adding 15 wt% of FR, the PHRR dropped by more than 35% to 624.1 W/g. However, the onset degradation temperature is 20 °C lower than the neat control. This lower onset degradation temperature is caused by the decomposition of the FR additive in order to produce a protective char layer at the surface [12]. For the last two formulations containing FR, elastomer and nanoclay, a further decrease in PHRR is observed. Formulation with 15wt% FR, 5wt% elastomer and 5wt% nanoclay have achieved PHRR 45% lower than the neat nylon 6. The heat release capacity follows the same trend as the PHRR. The HRC of 15_5_5 R fibers is 45% lower than neat nylon fibers. The effectively suppressed peak heat release rate and heat release capacity indicate that the nanocomposite fibers represent promising solutions for non-drip FR PA6 fibers.

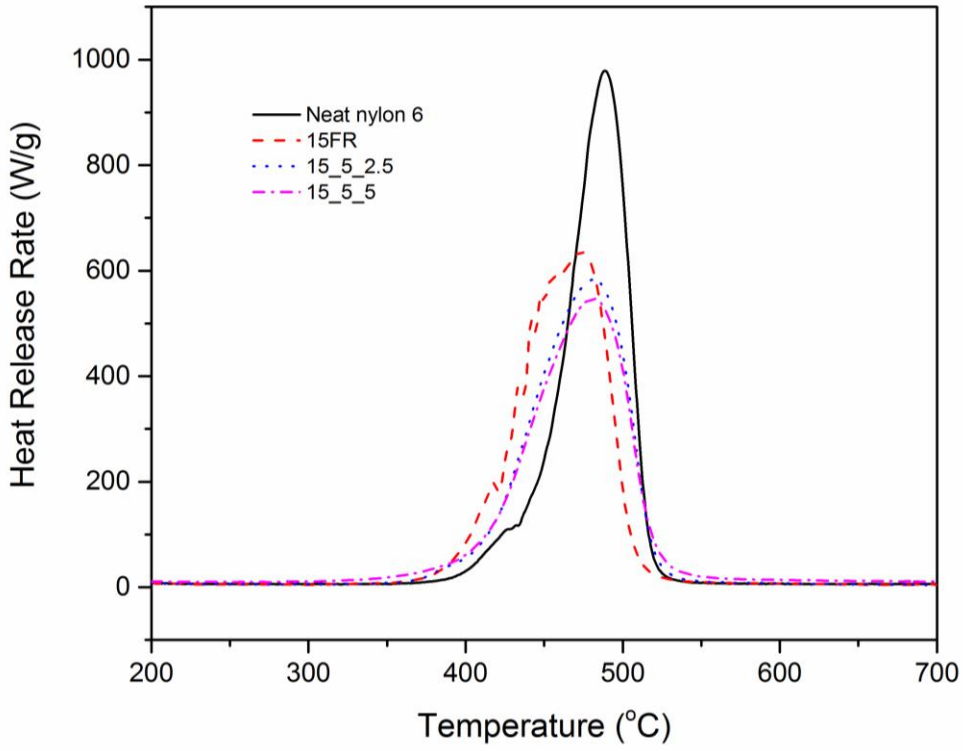

Figure 4.29. Typical heat release rate versus temperature curve of PA6/FR/elastomer/nanoclay fibers (Randcastle).

Table 4.6. Summary of heat release properties of PA6/FR/elastomer/nanoclay fibers (Randcastle).

Sample	Heat Release Capacity (J/g-K)	Peak Heat Release Rate (W/g)	Total Heat Release (kJ/g)	Peak Temperature (°C)
Neat PA6	701.8±10.6	973.6±15.4	33.5±0.2	488.2±0.7
15FR	453.0±4.1	624.1±6.6	30.4±0.2	467.1±2.9
15_5_2.5	415.4±5.3	574.7±7.9	29.6±0.2	478.0±1.0
15_5_5	384.2±3.2	531.7±4.6	28.3±0.2	478.5±1.3

4.3 CONCLUSION

In this chapter, FR PA6 nanocomposite fibers at two diameter ranges are successfully produced by melt-spinning. Ultra-sonication is an effective method to reduce the particle size of the FR additives. There is no significant difference in melt viscosity at

temperatures above 235 °C, therefore, 240 °C was used for the extrusion process. The presence of large FR aggregates result in rough fiber surfaces for both fiber diameters. XRD and TEM results suggest that the nanoclay platelets are well dispersed throughout the specimen. γ phase of the nylon 6 is predominant in both injection molding and fiber spinning FR PA6 samples. Moreover, preferentially alignment of nanoclay and elastomers are observed along the fiber axis. The second step of the α relaxation in PA6 is observed from in single fiber DMA results. No significant differences in relaxation temperature for FR PA6 fibers is observed. The addition of elastomers successfully recovered the lost elongation break caused by the addition of FR additives: nanocomposite fibers with 15 wt% FR, 5 wt% elastomer and 2.5 wt% nanoclay have elongation at break of 127% which is 44% higher than the sample with just FR. MCC characterization shows that a 45% reduction in heat release capacity was achieved in the nanocomposite fibers with 15 wt% FR, 5 wt% elastomer and 5 wt% nanoclay. From char morphology characterization the 15_5_5 D fibers retains its fiber shape after heating to 750 °C, which is an indication of its non-dripping nature. In conclusion, melt extrusion and fiber spinning is a promising technique for producing low cost non-dripping FR PA6 fibers.

4.4 REFERENCES

[1] M. Krifa, A Mixed Weibull Model for Size Reduction of Particulate and Fibrous Materials, Powder Technology 194(3) (2009) 233-238.
[2] F. Samyn, S. Bourbigot, Thermal decomposition of flame retarded formulations PA6/aluminum phosphinate/melamine polyphosphate/organomodified clay: interactions between the constituents?, Polymer Degradation and Stability 97(11) (2012) 2217-2230.
[3] J.D. Menczel, R.B. Prime, Thermal analysis of polymers, fundamentals and applications, John Wiley & Sons (2009).
[4] J.W. Cho, D.R. Paul, Nylon 6 nanocomposites by melt compounding, Polymer 42(3) (2001) 1083-1094.
[5] D. Wu, X. Wang, R. Jin, Toughening of poly(2,6-dimethyl-1,4-phenylene oxide)/nylon 6 alloys with functionalized elastomers via reactive compatibilization: morphology, mechanical properties, and rheology, European Polymer Journal 40(6) (2004) 1223-1232.
[6] J.J. Huang, H. Keskkula, D.R. Paul, Rubber toughening of an amorphous polyamide by functionalized SEBS copolymers: morphology and Izod impact behavior, Polymer 45(12) (2004) 4203-4215.
[7] Y.C. Ahn, D.R. Paul, Rubber toughening of nylon 6 nanocomposites, Polymer 47(8) (2006) 2830-2838.
[8] S.M. Burkinshaw, Polyamide Fibres, Physico-chemical Aspects of Textile Coloration, John Wiley & Sons, Ltd. (2016) pp. 427-490.
[9] M.A. Bellinger, C.W.A. Ng, W.J. Macknight, Effects of water on the mechanical relaxation in polyamide 4, Acta Polymerica 46(5) (1995) 361-366.
[10] H. Wu, J. Koo, M. Krifa, Rubber Toughening of Flame Retardant Polyamide 6 Nanocomposite Systems, SAMPE Conference Proceedings, Dallas, TX, (2015).
[11] H. Ohtani, T. Nagaya, Y. Sugimura, S. Tsuge, Studies on thermal degradation of aliphatic polyamides by pyrolysis-glass capillary chromatography, Journal of Analytical and Applied Pyrolysis 4(2) (1982) 117-131.
[12] B.J. Holland, J.N. Hay, Thermal degradation of nylon polymers, Polymer International 49(9) (2000) 943-948.

Chapter 5: Conclusion and Future Work

5.1 CONCLUSION

Although there are high performance FR fibers such as PBI® and Nomax®, their high cost limits their application to only niche markets. Nylon as an engineering thermoplastic is widely used in textile products because of its good mechanical properties and relatively low cost. This research explores the possibility of producing functional PA6 fibers for the purpose of creating inherently flame retardant textiles and study the processing-structure-performance relationship of the composite materials.

In this dissertation, cost effective alternative of producing non-drip inherently flame retardant PA6 fibers with balanced performances were developed by using twin screw extrusion and melt fiber spinning. Three different components including a phosphorus intumescent FR additive, a SEBS elastomer, and organo-modified nanoclay were explored for the FR formulation of PA6.

Injection molding technique was used as a tool for screening the performance of each FR PA6 formulation before the fiber spinning process. Preliminary results of injection molded FR PA6 nanocomposites suggest that although a good FR performance can be achieved, mechanical properties, especially ductility, are significantly compromised. To solve this problem, a thermoplastic block copolymer SEBS elastomer was introduced into the formulation matrix. SEBS is known for its high elasticity and, when treated with maleic anhydride, good compatibility with PA6 can be achieved. The well-known synergistic effect between nanoclay and FR was also explored in the formulation. XRD and DSC results for PA6/FR/elastomer and PA6/FR/elastomer/nancoclay formulations show that while only gamma crystals of the PA6 exist at the surface of the injection molded samples, the core contains both gamma and a small amount of alpha crystal. Good dispersion of elastomer and nanoclay was observed by TEM and XRD. The finely dispersed elastomer

hinders the chain movement of the PA6 resulting in lower crystallinity. Low concentration of nanoclay improves the crysatillinity through the nucleation effect. With the addition of the elastomers, significant improvement in ductility from the original FR system was achieved. The highest elongations of injection molded PA6/FR/elastomer and PA6/FR/elastomer/nanoclay are 116% and 76%, respectively. Both sets of formulations show low heat release capacities based on MCC. However, high elastomer concentration tends to degrade UL94 and LOI results.

Thermal stabilities of six injection-molded formulations were studied by TGA tests at multiple heating rates. From the TGA results, the activation energies of selected formulations were calculated using two isoconversion methods: the Flynn-Wall-Ozawa method and Lyon's method. The two methods yielded similar results: FR slightly reduces the Ea of the neat PA6 polymer due to earlier onset decomposition of the FR additive. Lower concentration of elastomer tended to increase the activation energy which is supported by MCC flammability results. Although nanoclay did not have a major impact on activation energy, it helped produce more protective char residue acting as thermal barrier.

Results on melt-spun fibers with two different diameters (i.e. ~200 μm and ~30 μm) are also presented. Ultra-sonication of the FR additives prior the fiber spinning has proven to be effective in reducing the FR particle size distribution. An alignment in well-dispersed nanoclay was found in nanocomposites fibers. The second step of the alpha relaxation in PA6 was observed from DMA loss modulus and tan δ results, no significant difference is found in FR formulations. Single fiber tensile test show that neat PA6 has the highest tenacity and elongation at break. PA6/FR/elastomer/nanoclay formulation allowed to improve both the tenacity and elongation at break by 44% from the original PA6/FR system. Finally, MCC flammability results showed low flammability and non-drip

behavior for the nanocomposite FR fibers. Synergistic effect between FR and nanoclay was observed. Among all formulations, fibers with 15 wt% FR, 5 wt% elastomer, and 5 wt% nanoclay remain in fiber form after combustion, which indicates that non-dripping property was successfully achieved.

In summary, our experiments have yielded non-drip inherently FR nylon fibers through the infusion of nanoclay (montmorillonite or MMT) and non-halogenated intumescent particles (FR) via co-rotating twin-screw extrusion. Rubber toughening allowed to effectively, albeit partially, recover the ductility lost after the addition of FR nanoclay particles. It is expected that further improvement in mechanical properties can be achieved with a better control of particle size distribution in the scale-up process.

One major implication of the results above is that with the new non-drip FR PA6 fiber, it would be possible to achieve blends with higher nylon content than customary without compromising the FR performance of the fabric. Indeed, experience shows that a typical neat nylon content in a FR fiber mix cannot exceed 10-12%, if one is to retain FR performance of the fabric. Our new FR PA6 nanocomposite will allow significantly increased amount of nylon in the blend, thus resulting in sizeable cost savings and in significant gains in applicability without compromising the FR protection.

5.2 FUTURE WORK:

To further explore the melt spun FR PA6 fibers, additional work can be focused on FR particle size optimization, manufacturing, and characterization of full scale FR fabric and new FR additives for PA6.

From the data presented, it is clear that the FR particle size distribution is not optimal for the fiber spinning process. In order to further improve the mechanical performance of the FR PA6 nanocomposite fibers, efforts could be made to fully separate

the FR particles from its cluster and minimize the presence of large FR aggregates. For example, a filtration process can be added following the ultra-sonication to screen out the large FR aggregates.

In many textile applications, the performance fibers will be blended with other commodity textile fibers to achieve a balance in performance, comfort and cost. One example is blending FR PA6 fibers with cotton for making low cost work clothes and uniforms. It would be useful to study the overall properties of the fiber blends with different blending ratios and structures. Finally, scale up of the manufacturing process shall be studied for large-scale commercial production of the FR PA6 fibers. To get preliminary results of the fabrics, the FR PA6 fibers and its blends can be processed into nonwovens by a simple needle punching process. Mechanical and flame retardant properties should be tested on the nonwoven fabric. Eventually, woven fabric made of FR PA6 fibers should be tested to evaluate the properties of the final product.

As the technology in FR chemistry advances, new types of FR additives may be developed in the future. The new FR additive may have nano-level dispersion and better compatibility with the polymer thus it could have less impact or even enhance the mechanical properties of the polymer matrix. The bio-based FRs developed in recent years such as lignin could be a promising and more environmental friendly option.

Bibliography

A. Blum, B.N. Ames, Flame-retardant additives as possible cancer hazards, Science 195(4273) (1977) 17-23.

A. Dasari, Z.-Z. Yu, Y.-W. Mai, Effect of blending sequence on microstructure of ternary nanocomposites, Polymer 46(16) (2005) 5986-5991.

A. Laachachi, M. Cochez, M. Ferriol, J.M. Lopez-Cuesta, E. Leroy, Influence of TiO_2 and Fe_2O_3 fillers on the thermal properties of poly(methyl methacrylate) (PMMA), Materials Letters 59(1) (2005) 36-39.

A. Usuki, A. Koiwai, Y. Kojima, M. Kawasumi, A. Okada, T. Kurauchi, O. Kamigaito, Interaction of nylon 6-clay surface and mechanical properties of nylon 6-clay hybrid, Journal of Applied Polymer Science 55(1) (1995) 119-23.

A.B. Morgan, C.A. Wilkie, Practical issues and future trends in polymer nanocomposite flammability research, John Wiley & Sons, New York, NY, USA, (2007).

A.B. Morgan, Flame retarded polymer layered silicate nanocomposites: a review of commercial and open literature systems, Polymers for Advanced Technologies 17(4) (2006) 206-217.

A.J. Oshinski, H. Keskkula, D.R. Paul, Rubber toughening of polyamides with functionalized block copolymers: 1. Nylon-6, Polymer 33(2) (1992) 268-283.

A.J. Oshinski, H. Keskkula, D.R. Paul, The role of matrix molecular weight in rubber toughened nylon 6 blends: 1. Morphology, Polymer 37(22) (1996) 4891-4907.

A.M. Calcraft, K. Maries, Burning of plastics. Part II A mathematical model of thermal response, Plast. Polym 42 (1974) 247.

A. Margolina, S. Wu, Percolation model for brittle-tough transition in nylon/rubber blends, Polymer 29(12) (1988) 2170-2173.

A.R. Horrocks, Flame retardant challenges for textiles and fibres: New chemistry versus innovatory solutions, Polymer Degradation and Stability 96(3) (2011) 377-392.

A.R. Horrocks, B.K. Kandola, P.J. Davies, S. Zhang, S.A. Padbury, Developments in flame retardant textiles – a review, Polymer Degradation and Stability 88(1) (2005) 3-12.

B.H. Cipiriano, T. Kashiwagi, S.R. Raghavan, Y. Yang, E.A. Grulke, K. Yamamoto, J.R. Shields, J.F. Douglas, Effects of aspect ratio of MWNT on the flammability properties of polymer nanocomposites, Polymer 48(20) (2007) 6086-6096.

B.J. Holland, J.N. Hay, Thermal degradation of nylon polymers, Polymer International 49(9) (2000) 943-948.

B.N. Jang, C.A. Wilkie, The effect of clay on the thermal degradation of polyamide 6 in polyamide 6/clay nanocomposites, Polymer 46(10) (2005) 3264-3274.

B.N. Jang, M. Costache, C.A. Wilkie, The relationship between thermal degradation behavior of polymer and the fire retardancy of polymer/clay nanocomposites, Polymer 46(24) (2005) 10678-10687.

Clariant GmbH, Division Pigments & Additives, Exolit® OP1312 Technical Datasheet, (2004).

Cloisite® 30B Typical Physical Properties Bulletin, Southern Clay Products, (2012) p. 2.

C. Siat, M. Le Bras, S. Bourbigot, Combustion behaviour of ethylene vinyl acetate copolymer-based intumescent formulations using oxygen consumption calorimetry, Fire and Materials 22(3) (1998) 119-128.

C.A. Wilkie, A.B. Morgan, Editors, Fire Retardancy of Polymeric Materials, Second Edition, CRC Press (2010).

C.D. Doyle, Estimating isothermal life from thermogravimetric data, Journal of Applied Polymer Science 6(24) (1962) 639-642.

C.J. Hilado, Flammability handbook for plastics, CRC Press (1998).

C.Q. Yang, Q. He, Applications of micro-scale combustion calorimetry to the studies of cotton and nylon fabrics treated with organophosphorus flame retardants, Journal of Analytical and Applied Pyrolysis 91(1) (2011) 125-133.

C.Q. Yang, H. Yang, The Flame Retardant Nomex/Cotton and Nylon/Cotton Blend Fabrics for Protective Clothing, in: S. Vassiliadis (Ed.), Advances in Modern Woven Fabrics Technology, InTech (2011).

D. Wu, X. Wang, R. Jin, Toughening of poly(2,6-dimethyl-1,4-phenylene oxide)/nylon 6 alloys with functionalized elastomers via reactive compatibilization: morphology, mechanical properties, and rheology, European Polymer Journal 40(6) (2004) 1223-1232.

D.C.O. Marney, L.J. Russell, D.Y. Wu, T. Nguyen, D. Cramm, N. Rigopoulos, N. Wright, M. Greaves, The suitability of halloysite nanotubes as a fire retardant for nylon 6, Polymer Degradation and Stability 93(10) (2008) 1971-1978.

D.M. Laura, H. Keskkula, J.W. Barlow, D.R. Paul, Effect of rubber particle size and rubber type on the mechanical properties of glass fiber reinforced, rubber-toughened nylon 6, Polymer 44(11) (2003) 3347-3361.

D.R. Paul, L.M. Robeson, Polymer nanotechnology: Nanocomposites, Polymer 49(15) (2008) 3187-3204.

E. Pearce, Flame-retardant polymeric materials, Springer Science & Business Media (2012).

E. Piorkowska, G.C. Rutledge, Handbook of polymer crystallization, John Wiley & Sons (2013).

E.D. Weil, S. Levchik, Current Practice and Recent Commercial Developments in Flame Retardancy of Polyamides, Journal of Fire Sciences 22(3) (2004) 251-264.

E.D. Weil, S.V. Levchik, Flame Retardants in Commercial Use or Development for Textiles, Journal of Fire Sciences 26(3) (2008) 243-281.

F. Chavarria, R.K. Shah, D.L. Hunter, D.R. Paul, Effect of melt processing conditions on the morphology and properties of nylon 6 nanocomposites, Polymer Engineering & Science 47(11) (2007) 1847-1864.

F. Dabrowski, M. Le Bras, R. Delobel, J.W. Gilman, T. Kashiwagi, Using clay in PA-based intumescent formulations. Fire performance and kinetic parameters, Macromolecular Symposia 194(1) (2003) 201-206.

F. Fiala, J. Králíček, The influence of a cation on thermal degradation of anionic polymerizates of ε-caprolactam, Collection of Czechoslovak Chemical Communications 40(4) (1975) 1155-1162.

F. Laoutid, L. Bonnaud, M. Alexandre, J.M. Lopez-Cuesta, P. Dubois, New prospects in flame retardant polymer materials: From fundamentals to nanocomposites, Materials Science and Engineering: R: Reports 63(3) (2009) 100-125.

F. Samyn, S. Bourbigot, Thermal decomposition of flame retarded formulations PA6/aluminum phosphinate/melamine polyphosphate/organomodified clay: interactions between the constituents?, Polymer Degradation and Stability 97(11) (2012) 2217-2230.

F. Samyn, S. Bourbigot, C. Jama, S. Bellayer, S. Nazare, R. Hull, A. Fina, A. Castrovinci, G. Camino, Characterisation of the dispersion in polymer flame retarded nanocomposites, European Polymer Journal 44(6) (2008) 1631-1641.

G. Gururajan, S.P. Sullivan, T.P. Beebe, D.B. Chase, J.F. Rabolt, Continuous electrospinning of polymer nanofibers of Nylon-6 using an atomic force microscope tip, Nanoscale 3(8) (2011) 3300-3308.

Honeywell Resins and Chemicals, Product Specification: Aegis®H95ZI, https://www.honeywell-nylon6.com/?document=honeywell-aegis-h95zi-datasheet&download=1, (January 2010).

H. Lu, C.A. Wilkie, Study on intumescent flame retarded polystyrene composites with improved flame retardancy, Polymer degradation and stability 95(12) (2010) 2388-2395.

H. Ohtani, T. Nagaya, Y. Sugimura, S. Tsuge, Studies on thermal degradation of aliphatic polyamides by pyrolysis-glass capillary chromatography, Journal of Analytical and Applied Pyrolysis 4(2) (1982) 117-131.

H. Wu, M. Krifa, J.H. Koo, Flame retardant polyamide 6/nanoclay/intumescent nanocomposite fibers through electrospinning, Textile Research Journal 84(10) (2014) 1106-1118.

H. Wu, J. Koo, M. Krifa, Rubber Toughening of Flame Retardant Polyamide 6 Nanocomposite Systems, SAMPE Conference Proceedings, Dallas, TX, (2015).

H. Wu, X. Yin, M. Krifa, M. Londa, J. Koo, Fabrication and Characterization of Flame Retardant Polyamide 6 Nanocomposites via Electrospinning, SAMPE TECH 2011, Fort Worth, TX, (2011).

H.F. Mark, J.I. Kroschwitz, Encyclopedia of polymer science and engineering, Wiley (1986).

H.H.G. Jellinek, The combustion of organic polymers, C. F. Cullis and M. M. Hirschler, Eds., Oxford university press, London, 1981, Journal of Polymer Science: Polymer Letters Edition 20(11) (1982) 606-606.

H.J. Ploehn, C. Liu, Quantitative Analysis of Montmorillonite Platelet Size by Atomic Force Microscopy, Industrial & Engineering Chemistry Research 45(21) (2006) 7025-7034.

H.Q. Peng, Q. Zhou, D.-Y. Wang, L. Chen, Y.-Z. Wang, A novel charring agent containing caged bicyclic phosphate and its application in intumescent flame retardant polypropylene systems, Journal of Industrial and Engineering Chemistry 14(5) (2008) 589-595.

IUPAC. Compendium of Chemical Terminology, 2nd ed. (the "Gold Book"). Compiled by A. D. McNaught and A. Wilkinson. Blackwell Scientific Publications, Oxford (1997). XML on-line corrected version: http://goldbook.iupac.org (2006-) created by M. Nic, J. Jirat, B. Kosata; updates compiled by A. Jenkins. ISBN 0-9678550-9-8. doi:10.1351/goldbook.).

I. Kelnar, J. Kotek, L. Kaprálková, B.S. Munteanu, Polyamide nanocomposites with improved toughness, Journal of Applied Polymer Science 96(2) (2005) 288-293.

I.K. Melvin, M.I. Kohan, Nylon Plastics Handbook, Hanser/Gardner Publications (1995).

J. Asrar, Polymer-bound non-halogen fire resistant compositions, US Patent US 5750603 A , (1998).

J.C. Lee, J.H. Koo, O.A. Ezekoye, K. Erickson, Heating rate and nanoparticle loading effects on thermoplastic polyurethane elastomer nanocomposite kinetics, AIAA Paper 4096 (2009).

J.D. Lichtenhan, J.W. Gilman, Preceramic additives as fire retardants for plastics, US Patent US 6362279 B2, (2002).

J.D. Lichtenhan, N.Q. Vu, J.A. Carter, J.W. Gilman, F.J. Feher, Silsesquioxane-siloxane copolymers from polyhedral silsesquioxanes, Macromolecules 26(8) (1993) 2141-2142.

J.D. Menczel, R.B. Prime, Thermal analysis of polymers, fundamentals and applications, John Wiley & Sons (2009).

J.G. Quintiere, Fundamentals of Fire Phenomena, John Wiley & Sons Ltd. (2006).

J.J. Huang, H. Keskkula, D.R. Paul, Rubber toughening of an amorphous polyamide by functionalized SEBS copolymers: morphology and Izod impact behavior, Polymer 45(12) (2004) 4203-4215.

J.K. Pandey, K. Raghunatha Reddy, A. Pratheep Kumar, R.P. Singh, An overview on the degradability of polymer nanocomposites, Polymer Degradation and Stability 88(2) (2005) 234-250.

J.W. Cho, D.R. Paul, Nylon 6 nanocomposites by melt compounding, Polymer 42(3) (2001) 1083-1094.

J.W. Gilman, T. Kashiwagi, J.D. Lichtenhan, Nanocomposites: a revolutionary new flame retardant approach, Sampe Journal 33 (1997) 40-46.

J.W. Gilman, Flammability and thermal stability studies of polymer layered-silicate (clay) nanocomposites, Applied Clay Science 15(1-2) (1999) 31-49.

J.W. Gilman, C.L. Jackson, A.B. Morgan, R. Harris, E. Manias, E.P. Giannelis, M. Wuthenow, D. Hilton, S.H. Phillips, Flammability Properties of Polymer−Layered-Silicate Nanocomposites. Polypropylene and Polystyrene Nanocomposites†, Chemistry of Materials 12(7) (2000) 1866-1873.

KRATON® FG1901 G Polymer Techinical Datasheet, http://docs.kraton.com/tl_warehouse/pdf_data_docs/WG_17864_WGC843.tmp.pdf, (2015).

M. Coquelle, S. Duquesne, M. Casetta, J. Sun, S. Zhang, S. Bourbigot, Investigation of the decomposition pathway of polyamide 6/ammonium sulfamate fibers, Polymer Degradation and Stability 106 (2014) 150-157.

M. Doğan, E. Bayramlı, The flame retardant effect of aluminum phosphinate in combination with zinc borate, borophosphate, and nanoclay in polyamide-6, Fire and Materials 38(1) (2014) 92-99.

M. Krifa, A Mixed Weibull Model for Size Reduction of Particulate and Fibrous Materials, Powder Technology 194(3) (2009) 233-238.

M. Le Bras, S. Bourbigot, E. Félix, F. Pouille, C. Siat, M. Traisnel, Characterization of a polyamide-6-based intumescent additive for thermoplastic formulations, Polymer 41(14) (2000) 5283-5296.

M. Lewin, Reflections on migration of clay and structural changes in nanocomposites, Polymers for Advanced Technologies 17(9-10) (2006) 758-763.

M. Norouzi, Y. Zare, P. Kiany, Nanoparticles as effective flame retardants for natural and synthetic textile polymers: application, mechanism, and optimization, Polymer Reviews 55(3) (2015) 531-560.

M. Paci, S. Filippi, P. Magagnini, Nanostructure development in nylon 6-Cloisite® 30B composites. Effects of the preparation conditions, European Polymer Journal 46(5) (2010) 838-853.

M. Zanetti, T. Kashiwagi, L. Falqui, G. Camino, Cone Calorimeter Combustion and Gasification Studies of Polymer Layered Silicate Nanocomposites, Chemistry of Materials 14(2) (2002) 881-887.

M.A. Bellinger, C.W.A. Ng, W.J. Macknight, Effects of water on the mechanical relaxation in polyamide 4, Acta Polymerica 46(5) (1995) 361-366.

M.J. Starink, The determination of activation energy from linear heating rate experiments: a comparison of the accuracy of isoconversion methods, Thermochimica Acta 404(1–2) (2003) 163-176.

M.N. Grigg, Thermo-oxidative degradation of polyamide 6, (2006). PhD dissertation, Queensland University of Technology.

N.F.P.A. (NFPA), Fires in the U.S., www.nfpa.org, (2015).

O.A. Pickett Jr, J.W. Stoddard, Phosphorus-containing copolyamides and fibers thereof, US Patent US 4092302 A , (1977).

O.K. Muratoglu, A.S. Argon, R.E. Cohen, M. Weinberg, Toughening mechanism of rubber-modified polyamides, Polymer 36(5) (1995) 921-930.

Product datasheet OP1312, Clariant, (2011).

R. Misra, B.X. Fu, A. Plagge, S.E. Morgan, POSS-nylon 6 nanocomposites: Influence of POSS structure on surface and bulk properties, Journal of Polymer Science Part B: Polymer Physics 47(11) (2009) 1088-1102.

R. Song, Z. Wang, X. Meng, B. Zhang, T. Tang, Influences of catalysis and dispersion of organically modified montmorillonite on flame retardancy of polypropylene nanocomposites, Journal of Applied Polymer Science 106(5) (2007) 3488-3494.

R.D. Davis, J.W. Gilman, D.L. VanderHart, Processing degradation of polyamide 6/montmorillonite clay nanocomposites and clay organic modifier, Polymer Degradation and Stability 79(1) (2003) 111-121.

R.E. Lyon, An integral method of nonisothermal kinetic analysis, Thermochimica Acta 297(1–2) (1997) 117-124.

R.E. Lyon, M.L. Janssens, Polymer flammability, National Technical Information Service (NTIS), Springfield, Virginia 22161, Washington, DC 20591, (2005).

R.E. Lyon, R.N. Walters, S.I. Stoliarov, Thermal analysis of flammability, Journal of Thermal Analysis and Calorimetry 89(2) (2007) 441-448.

R.E. Lyon, R.N. Walters, S.I. Stoliarov, Screening flame retardants for plastics using microscale combustion calorimetry, Polymer Engineering & Science 47(10) (2007) 1501-1510.

R.E. Lyon, R.N. Walters, A microscale combustion calorimeter, National Technical Information Service (NTIS), Springfield, Virginia 22161, (2002).

R.J.M. Borggreve, R.J. Gaymans, J. Schuijer, J.F.I. Housz, Brittle-tough transition in nylon-rubber blends: effect of rubber concentration and particle size, Polymer 28(9) (1987) 1489-1496.

R.S. Lehrle, I.W. Parsons, M. Rollinson, Thermal degradation mechanisms of nylon 6 deduced from kinetic studies by pyrolysis-g.c, Polymer Degradation and Stability 67(1) (2000) 21-33.

Spherulite. <https://commons.wikimedia.org/wiki/File:Spherulite2.PNG>, (2016).

S. Bourbigot, E. Devaux, X. Flambard, Flammability of polyamide-6/clay hybrid nanocomposite textiles, Polymer Degradation and Stability 75(2) (2002) 397-402.

S. Bourbigot, S. Duquesne, Fire retardant polymers: recent developments and opportunities, Journal of Materials Chemistry 17(22) (2007) 2283-2300.

S. Bourbigot, S. Duquesne, C. Jama, Polymer Nanocomposites: How to Reach Low Flammability?, Macromolecular Symposia 233(1) (2006) 180-190.

S. Bourbigot, S. Duquesne, G. Fontaine, S. Bellayer, T. Turf, F. Samyn, Characterization and reaction to fire of polymer nanocomposites with and without conventional flame retardants, Molecular crystals and liquid crystals 486(1) (2008) 325-1367.

S. Bourbigot, T. Turf, S. Bellayer, S. Duquesne, Polyhedral oligomeric silsesquioxane as flame retardant for thermoplastic polyurethane, Polymer Degradation and Stability 94(8) (2009) 1230-1237.

S. Duquesne, J. Lefebvre, S. Bourbigot, R. Delobel, P. Recourt, Thermal Stability and Fire Behavior of Intumescent Systems in Presence of Layered Inorganic Fillers and Silica, Fire and Polymers IV, American Chemical Society (2005) pp. 89-102.

S. Wu, A generalized criterion for rubber toughening: The critical matrix ligament thickness, Journal of Applied Polymer Science 35(2) (1988) 549-561.

S.C. Lao, C. Wu, T.J. Moon, J.H. Koo, A. Morgan, L. Pilato, G. Wissler, Flame-retardant polyamide 11 and 12 nanocomposites: thermal and flammability properties, J. Compos. Mater. 43(17) (2009) 1803-1818.

S. C. Lao, J. H. Koo, T. J. Moon, M. Londa, C. C. Ibeh, G. . Wissler, a.L. Pilato, Flame-retardant Polyamide 11 Nanocomposites: Further Thermal and Flammability Studies, J. of Fire Sciences 29(6) (2011) 479-498.

S.C. Lao, W. Yong, K. Nguyen, T.J. Moon, J.H. Koo, L. Pilato, G. Wissler, Flame-retardant polyamide 11 and 12 nanocomposites: processing, morphology, and mechanical properties, J. Compos. Mater. 44(25) (2010) 2933-2951.

S.C. Tjong, S.P. Bao, Impact fracture toughness of polyamide-6/montmorillonite nanocomposites toughened with a maleated styrene/ethylene butylene/styrene

elastomer, Journal of Polymer Science Part B: Polymer Physics 43(5) (2005) 585-595.

S.K. Lim, E.-P. Hong, Y.-H. Song, H. Choi, I.-J. Chin, Thermodynamic interaction and mechanical characteristics of Nylon 6 and polyhedral oligomeric silsesquioxane nanohybrids, Journal of Materials Science 47(1) (2012) 308-314.

S.M. Burkinshaw, Polyamide Fibres, Physico-chemical Aspects of Textile Coloration, John Wiley & Sons, Ltd. (2016) pp. 427-490.

S.V. Levchik, E.D. Weil, Combustion and fire retardancy of aliphatic nylons, Polymer International 49(10) (2000) 1033-1073.

S.V. Levchik, E.D. Weil, M. Lewin, Thermal decomposition of aliphatic nylons, Polymer International 48(7) (1999) 532-557.

T. Kashiwagi, F. Du, K.I. Winey, K.M. Groth, J.R. Shields, S.P. Bellayer, H. Kim, J.F. Douglas, Flammability properties of polymer nanocomposites with single-walled carbon nanotubes: effects of nanotube dispersion and concentration, Polymer 46(2) (2005) 471-481.

T. Kashiwagi, R.H. Harris, X. Zhang, R.M. Briber, B.H. Cipriano, S.R. Raghavan, W.H. Awad, J.R. Shields, Flame retardant mechanism of polyamide 6-clay nanocomposites, Polymer 45(3) (2004) 881-891.

T.D. Fornes, D.R. Paul, Crystallization behavior of nylon 6 nanocomposites, Polymer 44(14) (2003) 3945-3961.

T.F.Y. GmbH, The Fiber Year 2015, The Fiber Year GmbH, (2015).

T.M. Wu, E.-C. Chen, C.-S. Liao, Polymorphic behavior of nylon 6/saponite and nylon 6/montmorillonite nanocomposites, Polymer Engineering & Science 42(6) (2002) 1141-1150.

T.S. Lin, J.M. Cogen, R.E. Lyon, Correlations between microscale combustion calorimetry and conventional flammability tests for flame retardant wire and cable compounds, Proceedings of the 56th IWCS, (2007).

U. Braun, B. Schartel, M.A. Fichera, C. Jäger, Flame retardancy mechanisms of aluminium phosphinate in combination with melamine polyphosphate and zinc borate in glass-fibre reinforced polyamide 6,6, Polymer Degradation and Stability 92(8) (2007) 1528-1545.

U. Braun, H. Bahr, B. Schartel, Fire retardancy effect of aluminium phosphinate and melamine polyphosphate in glass fibre reinforced polyamide 6, e-Polymers (2010).

W. Wu, Flame retardant finishing for cotton using a hydroxy-functional organophosphorus oligomer, Dept. of Textiles, Merchandizing and Interiors, The University of Georgia, Athens, GA, (2004) p. 213.

W.C. Smith, High Performance and High Temperature Resistant Fibers-Emphasis on Protective Clothing, Industrial Textile Associates, (1999) p. 17.

X. Yin, H. Wu, M. Krifa, M. Londa, J. Koo, Flame retardant polyamide 6-MWNT nanocomposites: Characterization and processing via electrospinning, SAMPE TECH 2011, Fort Worth, TX, (2011).

Y. Chen, Z. Fang, C. Yang, Y. Wang, Z. Guo, Y. Zhang, Effect of clay dispersion on the synergism between clay and intumescent flame retardants in polystyrene, Journal of Applied Polymer Science 115(2) (2010) 777-783.

Y. Hu, S. Wang, Z. Ling, Y. Zhuang, Z. Chen, W. Fan, Preparation and Combustion Properties of Flame Retardant Nylon 6/Montmorillonite Nanocomposite, Macromolecular Materials and Engineering 288(3) (2003) 272-276.

Y.C. Ahn, D.R. Paul, Rubber toughening of nylon 6 nanocomposites, Polymer 47(8) (2006) 2830-2838.